République Algérienne Démocratique et Populaire
Ministère de l'Enseignement Supérieur et de la Recherche Scientifique

Université de Batna 2 – Mostefa Ben Boulaïd
Faculté de Technologie
Département de Génie Mécanique

Thèse

Présentée pour l'Obtention du Diplôme de
Doctorat en Sciences

Spécialité: Mécanique

Option: Construction Mécanique

Par
MOHAMMEDI Brahim

Contribution à la prédiction des défauts de bord dans une plaque élastique moyennant la propagation d'ondes de cisaillement (S-H waves)

Soutenue Publiquement le: 13/07/2019

Devant le jury composé de :

ZIDANI Kamel	Professeur	Université Batna 2	Président
BELGACEM BOUZIDA Aissa	Professeur	Université Batna 1	Rapporteur
NAHIL A Sobh	MCA	University of Illinois - USA	Co-Rapporteur
BARKAT Belkacem	Professeur	Université Batna 2	Examinateur
SEGHIR Kamel	Professeur	Université Batna 2	Examinateur
DERFOUF Chemseddine	Professeur	Université de Biskra	Examinateur
BELBACHA El-Djemai	Professeur	Université Batna 1	Invité

République Algérienne Démocratique et Populaire
Ministère de l'Enseignement Supérieur et de la Recherche Scientifique

Université de Batna 2 – Mostefa Ben Boulaïd
Faculté de Technologie
Département de Génie Mécanique

Thèse

Présentée pour l'Obtention du Diplôme de
Doctorat en Sciences

Spécialité: Mécanique

Option: Construction Mécanique

Par
MOHAMMEDI Brahim

Contribution to the prediction of edge defects in an elastic plate using SH waves

Soutenue Publiquement le: 13/07/2019

Devant le jury composé de :

ZIDANI Kamel	Professeur	Université Batna 2	Président
BELGACEM BOUZIDA Aissa	Professeur	Université Batna 1	Rapporteur
NAHIL A Sobh	MCA	University of Illinois - USA	Co-Rapporteur
BARKAT Belkacem	Professeur	Université Batna 2	Examinateur
SEGHIR Kamel	Professeur	Université Batna 2	Examinateur
DERFOUF Chemseddine	Professeur	Université de Biskra	Examinateur
BELBACHA El-Djemai	Professeur	Université Batna 1	Invité

To all my family

ملخص

تم فحص التفاعل بين موجات القص الافقية SH الموجهة مع نهاية حرة منحوتة لصفيحة نصف لانهائية بالطريقتين التحليلية والرقمية. وقد تم إعتماد فرض مادة الصفيحة مرنة ومتباينة المناحي. كما تمت نمذجة الصفيحة ذات التشوه على الحافة كتركيبة لمنطقتين : منطقة شبه لانهائية مع اجهادات منعدمة على السطوح ومنطقة قطاعية محددة ، المنطقتين تحدهما حدود مشتركة. تمت برهنة الحل التحليلي لحالة النهاية الحرة العمودية والذي تم استخدامه للتحقق من نجاعة البرنامج المنجز . في هذه الدراسة تم استخدام نمطين مختلفين واردين SH_0 و SH_1 كل على حده بهدف تحليل الأنماط المنعكسة والمرتبطة بالنهاية الحرة . تم إيجاد حل رقمي في حالة مجموعة واسعة من الترددات والزوايا المشطوفة. كما تم تمثيل خصوصا طاقة المرونة المنقولة بواسطة الانماط المنعكسة و ذلك باختيار زوايا مشطوفة و وترددات واردة. تم التأكد من صحة ودقة النتائج باعتماد مبدأ مصونية الطاقة و تقبل نسبة خطأ على الدقة لا تتجاوز 0 .001 %. المنهج التحليلي المقترح في هذه الأطروحة يساهم في فهم التفاعل بين الموجات SH الموجهة و عيوب المواد ويبين ان هذه الطريقة يمكن ان تشكل قاعدة إرشادية للمراقبة الغيرمدمرة للصفائح.

كلمات مفتاحية: نهاية منحوتة, تشوه الحافة, صفيحة مرنة, موجاتSH ,دالة الموجة

Abstract

The interaction of guided Shear Horizontal (SH) waves with the beveled free end of a semi-infinite plate is analytically and numerically investigated. The material of the plate is assumed to be elastic, homogenous, and isotropic. The plate with edge defect is modeled as a combination of a semi-infinite region with traction free surfaces and a bounded wedged region, separated by a common boundary. The analytical solution of the vertical free end case for the two regions is derived and used in verifying the numerical implementation. In this study, two single incident modes SH_0 and SH_1 were used individually in order to analyze the corresponding reflected modes from the free end. The numerical solution is determined for a wide range of frequencies and bevel angles. Specifically, the elastic energy carried by the reflected modes is reported for selected beveled angles and incident frequencies. The validity and accuracy of the results are checked by satisfaction of the energy conservation principle with a tight error tolerance less than 0.001 percent. The analytical approach proposed in this thesis contribute to the understanding of the interaction of guided SH waves with defects and shows that this method can be an efficient guidelines for non-destructive testing of plates.

Keywords: Bevel end; Edge defect; Elastic plate; SH waves; Wave function

Résumé

L'interaction des ondes de cisaillement horizontales (SH) guidées avec l'extrémité libre biseautée d'une plaque semi-infini est analytiquement et numériquement examinée. Le matériau de la plaque est supposé élastique, homogène et isotrope. La plaque présentant un défaut de bord est modélisée comme une combinaison d'une région semi-infinie avec des contraintes nulles en surfaces et d'une région sectorielle bornée, délimitées par une frontière commune. La solution analytique du cas d'extrémité libre verticale pour les deux régions est démontrée et utilisée pour vérifier l'implémentation numérique. Dans cette étude, deux modes incidents distincts SH_0 et SH_1 ont été utilisés individuellement afin d'analyser les modes réfléchis correspondants de l'extrémité libre. La solution numérique est déterminée pour une large gamme de fréquences et d'angles de biseau. Spécifiquement, l'énergie élastique transportée par les modes réfléchis est représentée pour une sélection d'angles biseautés et fréquences incidentes. La validité et la précision des résultats sont vérifiées par la satisfaction du principe de conservation de l'énergie avec une tolérance d'erreur étroite inférieure à 0,001%. L'approche analytique proposée dans cette thèse contribue à la compréhension de l'interaction des ondes SH guidées avec les défauts et montre que cette méthode peut constituer une ligne de conduite efficace pour le contrôle non destructif des plaques.

Mots clés: Extrémité biseautée; Défaut de bord; Plaque élastique; Ondes SH; Fonction d'onde.

Acknowledgement

This work would not have been possible without the financial support of the Algerian ministry of higher education and scientific research. It was carried out at the Beckman Institute for Advanced Science and Technology at the University of Illinois Urbana-Champaign, USA.

I would like to express my sincere gratitude to Professor Belgacem-Bouzida Aissa, my research supervisor, who offered continuous encouragement and guidance throughout this work. I would like to extend my deepest gratitude to Doctor Nahil Sobh, my research co-supervisor, for his patient, guidance and useful critiques of this research work. His office door was always open whenever I ran into a trouble or had a question about my research. In addition, he cared about my life and made me feel like I'm home during my stay in USA.

I would especially like to thank Professor Kamel Zidani, who accepted to be the chairman of my committee and devoted his precious time to review my thesis. I would also like to thank professor Chemseddine Derfouf, professor Kamel Seghir, professor Belkacem Barkat and professor El-Djemai Belbacha to be in the committee members. I also want to thank them for leaving my defense being enjoyable moments, and for their brilliant comments and suggestions.

I am very grateful for having been given the opportunity to work with Micro and Nanotechnology Laboratory (MNTL) research group at the University of Illinois at Urbana-Champaign. Thank you for your companionship and support. I would like to specifically thank Mr Diab Abueidda and Mr Dan Lanier for maintaining a great spirit of cooperation and assistance on Matlab code. I must mention my friend Slim Kibech who helped me getting started and who was of a great support to me.

I am grateful to my friends and colleagues of the Faculty of Technology and specifically the department of mechanical engineering for their help and encouragements. My thanks to Mr Lamir Saidi and Mr Mahieddine Naoun for their valuable discussion and revision of the thesis. I would also like to extend my thanks to Saleh Derradji, Saleh Madani, Ghazali Mebarki, Hamoudi Mazouz, Toufik Outtas, Brioua Mourad, Djamel Batache, Wahid Kaddouri, Mohamed Masmoudi.

Finally, I must express my very deep gratitude to my family for providing me with unfailing support and continuous encouragement throughout my years of study and through the process of researching and writing this thesis. This accomplishment would not have been possible without them.

Acronyms

EMAT	Electromagnetic-Acoustic Transducer
GWT	Guided Wave Testing
NDT	Non destructive testing
SAFE	Semi-Analytical Finite Element
SHM	Structural Health Monitoring
SH	Shear horizontal
A_0	Anti-symmetric zeroth SH mode
A_1	Anti-symmetric first SH mode
A_2	Anti-symmetric second SH mode
J_n	Bessel function of the first kind
S_0	Symmetric zeroth SH mode
S_1	Symmetric first SH mode
S_2	Symmetric second SH mode
Y_n	Bessel function of the second kind

Nomenclature

A_m	Amplitude of the reflected mode,
B_n	Amplitude of the sector region,
c_s	Shear velocity,
c_p	dilatational wave speed,
C_q	Amplitude of the incident mode,
d	Thickness,
E	Young's modulus,
E_m, E_q	Energy flux,
f	Frequency,
G	Shear modulus,
i	Imaginary index,
$J_{n\pi/\alpha}$	Bessel function,
k_m, k_q	Wave numbers,
m	Number of modes,
$\underset{\sim}{n}$	Outward normal to surface,
R	Maximum polar radius,
r	Polar radius,
R_{mq}	Energy flux ratio,
t	Time,
$\underset{\sim}{t}$	Stress vector,
U	Displacement field,

$\underset{\sim}{u}$	Displacement vector,
W_{ij}	infinitesimal rotation tensor,
w_i	vector rotation
α	Bevel angle,
Γ	Boundary surface,
δ_{ij}	Kronecker delta,
ε	Relative energy error,
ε_{ij}	Strain tensor,
ε_{ijk}	permutation symbol,
θ	Polar angle,
K	Non-dimensional wave number,
λ	Lame's constant,
λ	wavelength,
μ	Shear modulus,
ν	Poisson's ratio,
ρ	Mass density,
σ_{ij}	Stress tensor,
Ω	Non-dimensional frequency,
ω	Circular frequency,

Table of contents

List of figures

List of tables

Chapter 1

General Introduction

Chapter 1
General Introduction

1.1. Motivation

Mechanical structures are widely used and indispensable in modern industry (pressure vessels, pipelines, storage tanks, ship hulls, aircraft wings, etc.). These structures are easily affected by the presence of damage mechanisms, such as corrosion or cracks which change the material properties and geometric integrity, consequently enfeebling their performance and decreasing their service life (Figure 1.1).

Figure 1.1: Mechanical structures

Testing these structures is a significant issue for safety reasons and environmental impact control. Small defects are admissible as long as they are limited in size and if no overload occurs. Structural damage can continue to increase for a long time, but the ultimate failure is generally quick and unexpected. The consequences can be disastrous (structure collapse, aircraft crash, storage tank burst) (Figure 1.2). Such disasters can be predicted and avoiding such events is a good motivation for Structural Health Monitoring (SHM). This technique is rapidly emerging as a critical tool for continuous nondestructive inspection. It is used to evaluate material properties, components, or entire process units.

Figure 1.2: Incident of Aloha Airlines, Flight 243

In a typical SHM process, sensors are permanently installed to enable periodic assessment of the structure damage state. It provides information for making decisions about equipment life assessment [Boukabache et al, 2014].

A Structural Health Monitoring system is a kind of imitation of the human nervous system with integrated sensors and diagnostic capabilities (Figure 1.3). The analogy between the operation of the human nervous system and structure SHM is represented as follow, (Table 1.1):

Table 1.1. Analogy between operation of the human nervous system and structure SHM

Human Nervous system	Structural Health Monitoring system
More **nerves** around critical **organs**	More **sensors** around critical **parts**
Pain indication	**Damage** indication
The brain checks the intensity of the pain and judges when to go to the doctor.	The SHM system checks the structure and evaluate the reexamination actions for maintenance.

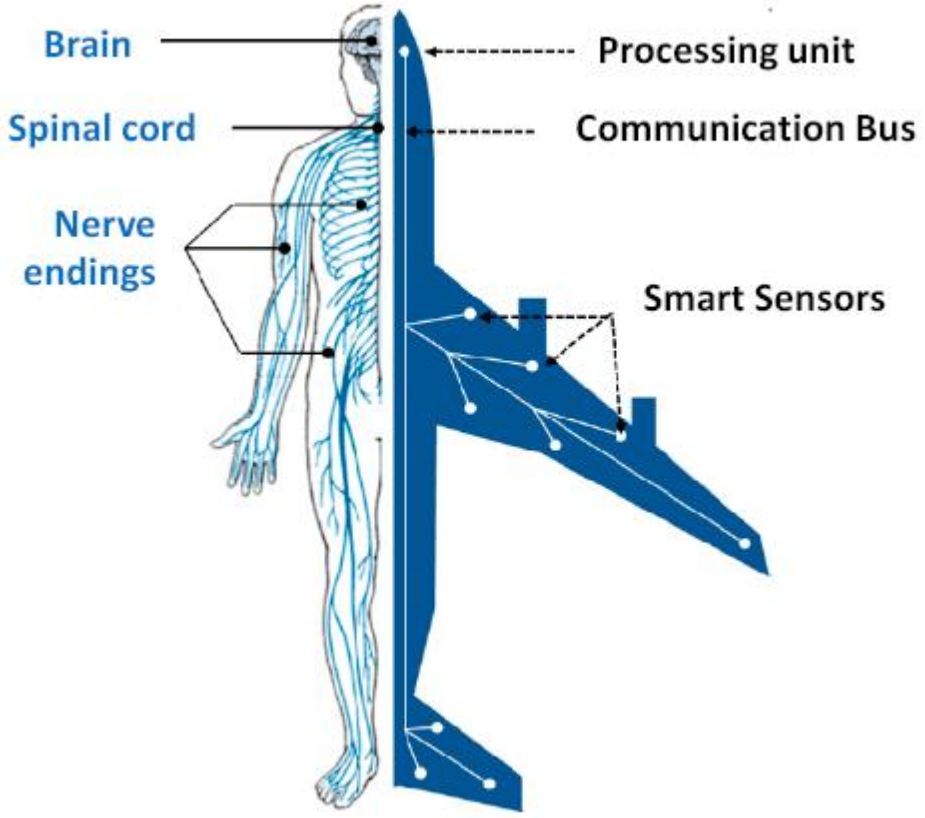

Figure 1.3: Analogy between the operation of the human nervous system and of SHM of a structure [Boukabache et al, 2014].

To improve the performance of structures monitoring, and reduce the operational cost at the same time, many researchers explored recently some new kind of structural health monitoring systems.

One of these SHM techniques is the employment of guided waves which proved to be useful in locating various types of defects in both plates and tubes. Guided waves refer to mechanical (or elastic) waves that propagate in a bounded medium parallel to the plane of its boundary. (Figure 1.4).

Figure 1.4: Pipeline inspection using guided wave testing (GWT)

The wave is called "guided" when it travels along the medium guided by its geometric boundaries. For this reason, the geometry has a strong influence on the behavior of the wave [Redwood, 1960]; [Rose, 1999]. Guided waves have advantages in their capacity to propagate from a single location over long distances in plates and tubes (Figure 1.5). They can offer good estimates of location, severity, and damage type, thus admitting higher efficiency, low in cost and fast detection of defects in large area of the structures [Staszewski et al, 2004]; [Croxford et al, 2007]; [Annamaria, 2016].

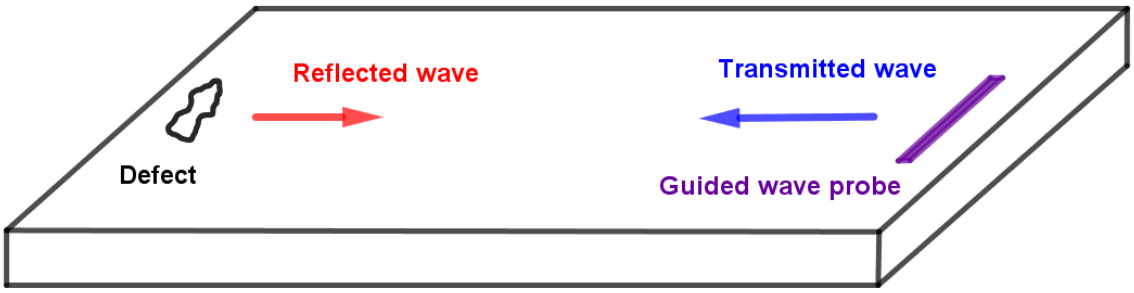

Figure 1.5: Guided wave through a plate with defect

The benefit of guided waves can also include:

- High percentage coverage throughout the thickness of the structure
- Ability of inspection of hidden and inaccessible regions of the structure
- Inspection of underwater structures, coatings, insulation and concrete.
- Avoidance of removal/reinstatement of insulation or coatings.

Guided waves can potentially be used for plate inspection such as airplane fuselage and wings often made of aluminum sheets. These sheets are assembled from holes by fasteners, which are sources of stress concentration and crack formation. The interaction of guided elastic waves with discontinuities in the structures has been the subject of scientific research of many scholars. Discontinuities in structures can be either geometrical or due to material property changes.

The complexity of such physical phenomenon fascinated many scientists over several years and has not been explained for all possible cases encountered in real situations [Demma, 2003]. Generally, the solution to such problems presents a very redoubtable challenge. A correct understanding of the physical and mathematical principles of the discontinuity effect in the structure is essential for effective utilization of these guided waves.

An important class of guided waves is the horizontal shear waves known as SH waves. The particle motion of SH waves is polarized parallel to the plate surface and perpendicular to the direction of wave propagation. These waves remain confined inside the walls of the structure and hence can travel over vast distances without energy loss (Figure 1.6).

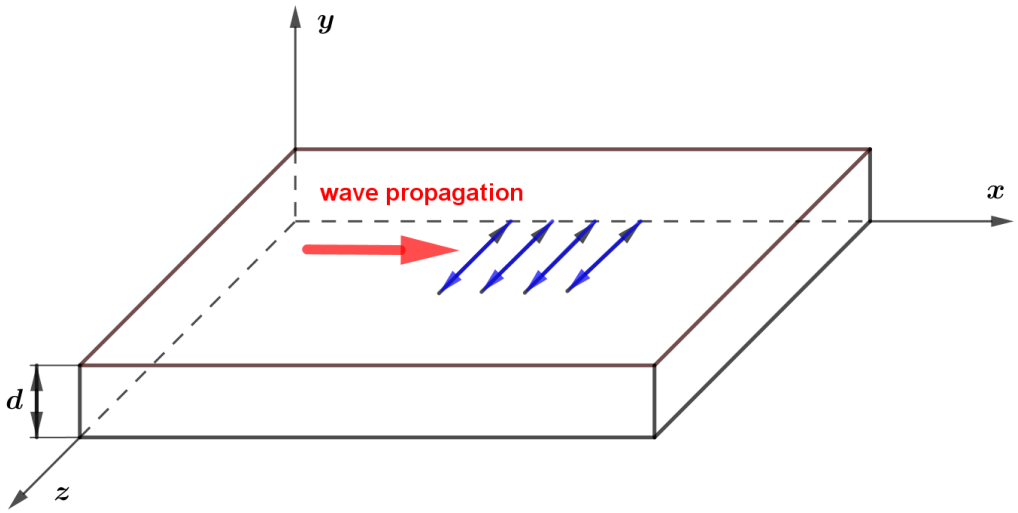

Figure 1.6: SH wave in a plate

On the other hand, the properties of the fundamental wave mode (SH_0) make them very convenient for the inspection of the structure with good capability to detect defects. For those reasons, SH guided waves have the potential to be used for Non-Destructive Testing (NDT) and have recently attracted considerable interest in the structural health monitoring community [Adams, 2007] ; [Kamal and Giurgiutiu, 2014] ; [Castaings, 2014].

For the purpose of NDT studies, it is essential to model the SH wave propagation and interaction with defects analytically. This allows prediction of the repercussions of these defects on wave propagation. The knowledge of SH wave interaction with specific geometrical features can also help in the selection of incident modes and frequencies that improve inspection to various discontinuities. In the simplest case, one-single incident wave mode is used, after that it can be converted to other reflected modes in order to satisfy boundary conditions. The determination of reflection and transmission coefficients from discontinuities of different kinds has been studied by many scholars. Several approaches were proposed. The first is the development of numerical methods and tools to simulate the phenomena. The second is the development of appropriate experimental methods and techniques allowing verification and validation results of numerical simulations.

For numerical methods, different approaches were investigated as methods based on wave expansion (mode-matching) methods [Chen et al, 2015] ; [Ditri, 1996]; [Nakamura et al, 2012]; [Ahmad and Gabbert, 2012]; [Chancellier et al, 2002], finite element methods [Rajagopal and Lowe, 2007]; [Ratassep et al, 2008] ;[Koshiba et al, 1987]; [Lowe and Diligent, 2002]; [Demma et al, 2003]; [Gunawan and Hirose, 2004], or a combination of finite element formulations with waves function expansion technique [Annamaria, 2016]. Unfortunately, the study of the effects of multiple angles representing the direction of discontinuities was not widely analyzed. For these raisons, a better understanding of the interaction of guided SH waves with a beveled free end in a plate is needed.

The aim of this thesis is to develop an analytical and numerical model for SH guided wave propagation in an isotropic plate with a beveled free end. Applying these proposed procedures, the interaction between the guided waves and edge defects is well analyzed. [Mohammedi et al, 2019] The background literature on the different issues is presented in the following section.

1.2. Previous work

Although experimental observations of dynamic edge phenomenon in elastic waveguides took place over 70 years ago, the reflection of guided waves from the free end of an elastic layer remains an active area of research. Lawrie et al. [Lawrie and Kaplunov, 2012] provided a detailed review of the field that covered the period from 1958 to 2008. Within this context, a follow-up report was made by Deckers et al. [Deckers et al, 2014] in which they discussed and summarized research on wave-based methods.

Researchers have made tremendous advancements utilizing mode and frequency selections to solve many problems; for example, in the testing of pipes, rails, plates, ship hulls, and aircraft integrity [Giurgiutiu, 2007]; [Pujol, 2003]; [Rose, 2014]. In recent years, the inspection of irregularities and defects such as cracks have been carried out using horizontally polarized shear (SH) waves

generated and detected by electromagnetic-acoustic transducers [Rose, 2000]; [Gao and Lopez, 2010]; [Hirao and Ogi, 1999].

The study of scattering problems varies from classical approaches such as mode matching and variational techniques to numerical techniques such as finite element and boundary element approaches, or a combination of numerical formulations with a wave function expansion technique. Among these, Abduljabbar et al. [Abduljabbar et al, 1983] studied the diffraction of SH waves in a plate with arbitrary defects by employing a finite element formulation and wave function expansion technique. Furthermore, Chen et al. [Chen et al, 2015] studied the SH guided waves propagated in a tapered plate using eigenmode matching theory and finite element methods. Ditri [Ditri, 1996] dealt with the scattering of guided elastic SH waves from material and geometric waveguide discontinuities. Nakamura et al. [Nakamura et al, 2012] studied the mode conversion behavior of an SH guided wave in a tapered plate. They investigated the different mode conversion phenomenon for abrupt and gradual thickness changes.

Many investigations have been made to study the beveled end of plates using Lamb waves. A semi-analytical finite element method has been used to simulate Lamb wave reflections at plate edges [Ahmad and Gabbert, 2012]. The Lamb wave conversion due to the beveled free end of plates has been studied theoretically as well as numerically, using the finite element method [Chancellier et al, 2002]; [Mofakhami and Boller, 2008]. Chancellier et al. used a collocation method on the beveled free end to determine the Lamb wave amplitudes and edge resonance [Chancellier et al, 2005].

Several experimental works have been published on the reflection of Lamb waves by the free and beveled edge of a plate [Castaings et al, 2002]; [Morvan et al, 2003]; [Chancellier et al, 2004]; [Santhanam and Demirli, 2013]. In these papers, the mode conversions were examined in detail over an extensive frequency range, and the energy conversion coefficients were obtained both numerically (finite element method) and experimentally.

1.3. Scope and objectives

The aim of this thesis is to contribute to the understanding of SH wave propagation in an elastic plate with edge defects. The method of separation of variables (also known as the wave function expansion) is used to investigate the interactions of SH waves with the beveled free end of an elastic plate. The plate is divided into two non-overlapping regions with a common interface. Each region admits a separable solution of the corresponding wave equation. The total solution is assembled by enforcing continuity conditions at the interface. The solution preserves the total incident energy to within a small tolerance. The convergence of the solution is met when the difference between the total incident energy and reflected energy is less than 0.001% which is a very tight criterion compared to existing convergence criteria reported in many works available in the literature [Abduljabbar et al, 1983]; [Ditri, 1996]; [Morvan et al, 2003]; [Chancellier et al, 2005]. The solution provided here is compared with the known solution for a plate with a vertical end [Giurgiutiu, 2007]; [Rose, 2014].

Finally, very good agreement between the proposed numerical approach and analytical solution is observed. This indicates the effectiveness of the proposed approach. A wide range of beveled angles and incident frequencies is studied and reported here [Mohammedi et al, 2019].

1.4. Thesis outline

This thesis is divided into five chapters. The present chapter is intended to provide a general introduction to the subject, research backgrounds and useful information.

The second chapter presents a literature review of the theoretical fundamentals of wave propagation, which gives all the research background and useful information about this thesis. Guided waves in elastic plates are then introduced with particular attention on SH waves which are used in this study.

Chapter 3 describes the analysis of SH waves propagating in a beveled free end plate. A region matching technique is applied to derive a series solution. Appropriate wave functions are employed to describe the displacement field. The unknown coefficients are determined by the enforcement of the continuity of displacements and stresses at the fictitious common boundary. The particular case of a plate with vertical edge is used in order to test the numerical results obtained in chapter 4

Chapter 4 deals with the numerical results of the reflecting SH waves in terms of the ratio between the energy of the m^{th} reflected mode and the energy of the q^{th} incident mode. Beveled angles ranging from 20° to 90° with 0.1° increment and normalized frequencies ranging from 0 to 5.5 are considered. The validity and accuracy of the results are checked by satisfaction of the energy conservation principle. The energy ratios are plotted as function of the beveled angles and normalized frequencies. After all, a comparative study between different approaches mentioned in the literature is done and shows the novelty of this work

In the last chapter, conclusion is provided on the findings of this thesis and additional topics that will be the subject of future work are proposed.

Chapter 2

Background and literature review

Chapter2

Background and literature review

2.1. Introduction

In this chapter, the basic theoretical concepts for waves propagating in elastic solids on the basis of the continuum theory are described. Continuum mechanics is a classical subject that has been discussed in great generality in numerous treatises. The theory of continuous media is built upon the basic concepts of stress, motion, and deformation, upon the laws of conservation of mass, linear momentum and on the constitutive relations. The governing equations used in this thesis are for homogeneous, isotropic, linearly elastic solids. These equations are valid if it may be assumed that the strains are small and that the stress components are proportional to the strains.

The theory of wave propagation in solids is well developed and dates back to the early 1800s with the discovery of dynamical equations and waves in solids by Cauchy [Cauchy, 1822], Poisson [Poisson, 1829] and Lamé [Lamé, 1852]. During that time, these studies were merely an extension of the theory of elasticity. Poisson was the first to recognize that elastic disturbance was in general composed of two types of fundamental waves (dilatational and equivoluminal ones).

The linear theory of elasticity is based upon a linear approximation (geometrical and physical). Although it does not give an exact description of dynamics, it does provide a handy solution that is applicable as long as the assumptions are valid. This linear theory is the subject of many classic texts. A famous work entitled Mathematical Theory of Elasticity by A. E. H. Love [Love, 1906] was published in 1892 and has been reprinted many times until 1944. Numerous objects, such as an elastic 3D medium, a half space, waveguides, etc. were being studied. A wide range of waves was described, and particular

mathematical methods for analysis were derived. In recent years several books have appeared specifically dealing with wave propagation in linearly elastic solids. We mention the books presented by Kolsky [Kolsky, 1963], Achenbach [Achenbach, 1973], Whitham [Whitham, 1974], Graff [Graff, 1991], and Miklowitz [Miklowitz, 1980]. These books have summaries of the relevant elastodynamic theory. This theory is essential to the development of the method of wave propagation in plates developed in later sections.

2.2. Fundamental equations of elastodynamics

The theory to be introduced in this section attempts to deal with problems from a more fundamental basis (The dynamic theory of elasticity, called elastodynamics). The significant aspects of the theory needed for a basic understanding are presented to pursue the study in the upcoming chapters.

2.2.1. Tensor notation

Elastodynamics deals with physical quantities which are independent of any particular coordinate system that may be used to describe them. At the same time, these physical quantities are very often specified most conveniently by referring to an appropriate system of coordinates. Mathematically, such quantities are represented by Tensor. Tensor notation permits a compact expression to be written for the equations of mathematical physics that also indicates the form natural laws should take. Both indicial notation and vector notation are used in this thesis. In a Cartesian coordinate system with coordinates denoted by x_i, the vector $\underset{\sim}{u}(\underset{\sim}{x},t)$ is presented by

$$\underset{\sim}{u} = u_1\underset{\sim}{e}_1 + u_2\underset{\sim}{e}_2 + u_3\underset{\sim}{e}_3 \tag{2.1}$$

Where, $\underset{\sim}{e}_i$ $(i=1,2,3)$ are a set of orthonormal base vectors. Since summations of the type (2.1) occur frequently, it is convenient to introduce the *summation convention*, whereby a repeated index means summation over all values of that index. Thus, the three-term expression (2.1) can be simply written as

$$\underset{\sim}{u} = u_i \underset{\sim}{e}_i \tag{2.2}$$

The repeated index is called a *dummy index* because it can be replaced by any othersymbol that has not already been used in that expression. Thus, the expression in equation (2.2) can also be written as

$$\underset{\sim}{u} = u_i \underset{\sim}{e}_i = u_j \underset{\sim}{e}_j = u_m \underset{\sim}{e}_m \tag{2.3}$$

Similarly we may have a set of nine quantities such as a_{ij} $(i, j = 1,2,3)$. Use will be made of *Kronecker delta* defined as

$$\delta_{ij} = \begin{cases} 1 & \text{for } i = j, \\ 0 & \text{for } i \neq j, \end{cases} \tag{2.4}$$

Permutationsymbol is defined as follows:

$$\varepsilon_{ijk} = \begin{cases} 1, & \text{if } i, j, k \text{ are an even permutation of } 1,2,3, \\ -1, & \text{if } i, j, k \text{ are an odd permutation of } 1,2,3, \\ 0, & \text{otherwise.} \end{cases} \tag{2.5}$$

The following notation is used for the field variables:

- Position vector $\underset{\sim}{x}$ (coordinates x_i)
- Displacement vector $\underset{\sim}{u}$ (components u_i)
- Strain tensor $\underset{\sim}{E}$ (components ε_{ij})
- Stress tensor $\underset{\sim}{\sigma}$ (components σ_{ij})

It may generally be assumed that the functions $u_i(x_i, t)$ are differentiable. A shorthand notation for the nine partial derivatives is

$$\frac{\partial u_i}{\partial x_j} = u_{i,j} \tag{2.6}$$

where the comma denotes partial differentiation with respect to the Cartesian coordinates x_j.

It can be shown that the $u_{i,j}$ are the components of a second order tensor. A time derivative is often indicated by a dot over the quantity, i.e., $\frac{\partial u_i}{\partial t} = \dot{u}_i$

2.2.2. Displacement

Displacement characterizes vibrations, is a distance of a particle from its position of equilibrium. The field defining the displacement at position $\underset{\sim}{x}$ at time t is denoted by the displacement vector $\underset{\sim}{u}(\underset{\sim}{x},t)$

$$\underset{\sim}{u}(\underset{\sim}{x},t) = u_1(\underset{\sim}{x},t)\underset{\sim}{e}_1 + u_2(\underset{\sim}{x},t)\underset{\sim}{e}_2 + u_3(\underset{\sim}{x},t)\underset{\sim}{e}_3 = u_i(\underset{\sim}{x},t)\underset{\sim}{e}_i \tag{2.7}$$

2.2.3. Strain

As a direct implication of the notion of a continuum, the deformation of the medium can be expressed in terms of the gradients of the displacement vector.

$$u_i(\underset{\sim}{x}+\delta\underset{\sim}{x}) \approx u_i(\underset{\sim}{x}) + \frac{\partial u_i(\underset{\sim}{x})}{\partial x_j}\delta x_j = u_i(\underset{\sim}{x}) + \delta u_i \tag{2.8}$$

Therefore, in the first order assumption

$$\begin{aligned}\delta u_i &= \frac{\partial u_i(\underset{\sim}{x})}{\partial x_j}\delta x_j = \frac{1}{2}\left(\frac{\partial u_i}{\partial x_j} + \frac{\partial u_j}{\partial x_i}\right)\delta x_j + \frac{1}{2}\left(\frac{\partial u_i}{\partial x_j} - \frac{\partial u_j}{\partial x_i}\right)\delta x_j \\ &= \frac{1}{2}\left(u_{i,j} + u_{j,i}\right)\delta x_j + \frac{1}{2}\left(u_{i,j} - u_{j,i}\right)\delta x_j = (\varepsilon_{ij} + \omega_{ij})\delta x_j\end{aligned} \tag{2.9}$$

Where the symmetric part of (2.9)

$$\varepsilon_{ij} = \frac{1}{2}\left(u_{i,j} + u_{j,i}\right) \tag{2.10}$$

is the linear strain tensor and the skew symmetric part

$$\omega_{ij} = \frac{1}{2}\left(u_{i,j} - u_{j,i}\right) \tag{2.11}$$

is the linear rotation tensors, which contain the spatial derivatives of the displacement field.

2.2.4. Forces and stress

In general forces on a body may be classified into two categories:

1. *Body forces*: Forces acting on all elements of volume of a continuum. Examples are gravity and inertia forces. These forces are represented by the symbol p_i (force per unit volume)

2. *Surface forces:* Forces acting on the surface of a body, resulting from physical contact with another body.

Applied external loads induce internal forces and stresses inside a body. In three-dimensions, the stress is defined by

$$\sigma_{ij} = \begin{bmatrix} \sigma_{11} & \sigma_{12} & \sigma_{13} \\ \sigma_{21} & \sigma_{22} & \sigma_{23} \\ \sigma_{31} & \sigma_{32} & \sigma_{33} \end{bmatrix}, \tag{2.12}$$

which is a second order tensor, and the first subscript indicates the surface applied and the second the direction (Figure 2.1).

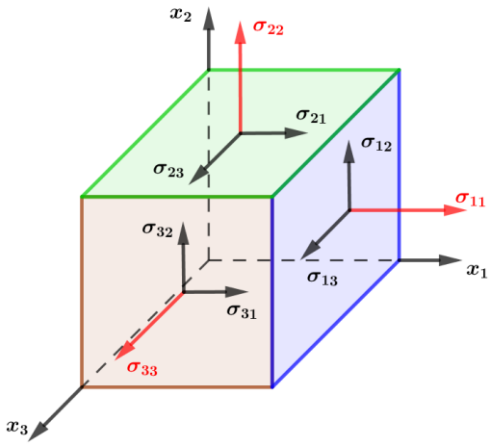

Figure 2.1: Cartesian stress components.

Thus if a surface element has a unit outward normal $\underset{\sim}{n}$ the surface traction $\underset{\sim}{t}$ (stress vector) is introduced, defining a force per unit area. The surface tractions generally depend on the orientation of $\underset{\sim}{n}$ as well as the location $\underset{\sim}{x}$.

$$t_i^n = \sigma_{ij} n_j \tag{2.13}$$

Equation (2.13) is the Cauchy stress formula.

2.2.5. Equations of motion

According to the principle of balance of linear momentum, the instantaneous rate of change of the linear momentum of the body is equal to the resultant external force acting on the body at a particular instant of time. In the linear theory, this leads to the equations.

$$\sigma_{ij,j} + p_i = \rho \ddot{u}_i \tag{2.14}$$

where ρ is the mass density per unit volume.

Equations (2.14) are known as *Cauchy equations of motion*. For the linearized theory, the balance of moment of momentum yields the result $\sigma_{ij} = \sigma_{ji}$, i.e., the stress tensor is *symmetric*.

2.2.6. Stress-strain relation

Assuming that the material is linearly elastic and that only small deformations are present in the domain, the linear relation between the components of the stress tensor and the components of the strain tensor is

$$\sigma_{ij} = C_{ijkm} \varepsilon_{km} \tag{2.15}$$

which is known as the *generalized Hooke's law*.

In (2.15) C_{ijkm} is a fourth-order tensor containing 81 elastic constants or matrix components that define the elastic properties of the material in the anisotropic medium. However, due to the symmetry of both the stress and strain tensors, there are at most 36 distinct elastic constants. Through strain energy

considerations, it follows that $C_{ijkm} = C_{kmij}$, so that even in the case of anisotropy the number of constants can be reduced to 21. The assumption of isotropy reduces the number of independent elastic constants to just 2. In summary for an isotropic, continuous medium, the elastic constant tensor can be reduced to the following:

$$c_{ijkm} = \lambda\delta_{ij}\delta_{km} + \mu(\delta_{ik}\delta_{jm} + \delta_{im}\delta_{jk}) \tag{2.16}$$

Equation (2.16) contains two elastic constants λ and μ, which are known as Lamé's elastic constants, which are related to the Young's modulus E and the Poisson ratio ν as

$$\lambda = \frac{\nu E}{(1+\nu)(1-2\nu)}, \quad \mu = \frac{E}{2(1+\nu)} \tag{2.17}$$

Since the material is homogeneous, λ and μ are independent of x. The Lamé constant μ is also identified as the *shear modulus*, which is often denoted G. The stress-strain relationship (2.15) simplifies to

$$\sigma_{ij} = \lambda\delta_{ij}\varepsilon_{kk} + 2\mu\varepsilon_{ij} \tag{2.18}$$

which is known as the *Hook's law* for isotropic elastic behavior.

2.2.7. Navier equations

The system of equations governing the motion of a homogeneous, isotropic, linearly elastic solid consists of Cauchy equations of motion, Hooke's law and the strain-displacement relations [Rose, 2014]; [Achenbach, 1973]. The strain-displacement relations (2.10) may be substituted into Hooke's law (2.18) and the result in turn substituted into the stress equation of motion (2.14) to produce the governing equations

$$\mu u_{i,jj} + (\lambda + \mu)u_{j,ji} + p_i = \rho\ddot{u}_i \tag{2.19}$$

Motion equations (2.19) containing only particle displacements (displacement vector u_i) are displacement-type partial differential equations known as *Navier* equations and represent three equations in Cartesian notation

$$\begin{aligned}
&\mu\left(\frac{\partial^2 u_x}{\partial x^2}+\frac{\partial^2 u_x}{\partial y^2}+\frac{\partial^2 u_x}{\partial z^2}\right)+(\lambda+\mu)\frac{\partial}{\partial x}\left(\frac{\partial u_x}{\partial x}+\frac{\partial u_y}{\partial y}+\frac{\partial u_z}{\partial z}\right)+p_x=\rho\frac{\partial^2 u_x}{\partial t^2}\\
&\mu\left(\frac{\partial^2 u_y}{\partial x^2}+\frac{\partial^2 u_y}{\partial y^2}+\frac{\partial^2 u_y}{\partial z^2}\right)+(\lambda+\mu)\frac{\partial}{\partial y}\left(\frac{\partial u_x}{\partial x}+\frac{\partial u_y}{\partial y}+\frac{\partial u_z}{\partial z}\right)+p_y=\rho\frac{\partial^2 u_y}{\partial t^2}\\
&\mu\left(\frac{\partial^2 u_z}{\partial x^2}+\frac{\partial^2 u_z}{\partial y^2}+\frac{\partial^2 u_z}{\partial z^2}\right)+(\lambda+\mu)\frac{\partial}{\partial z}\left(\frac{\partial u_x}{\partial x}+\frac{\partial u_y}{\partial y}+\frac{\partial u_z}{\partial z}\right)+p_z=\rho\frac{\partial^2 u_z}{\partial t^2}
\end{aligned} \tag{2.20}$$

In vector notation equation of motion (2.19) becomes

$$\mu\nabla^2\underset{\sim}{u}+(\lambda+\mu)\nabla\nabla\cdot\underset{\sim}{u}+\underset{\sim}{p}=\rho\ddot{\underset{\sim}{u}} \tag{2.21}$$

2.3. Elastic waves in unbounded media

Elastic waves are mechanical waves propagating in an elastic medium as an effect of forces associated with volume deformation (compression and extension) and shape deformation (shear) of medium elements [Pujol, 2003]. The solution of the equation of motion for an elastic medium results in the existence of elastic waves in its interior. The wave phenomenon is a way of transporting energy without transport of matter. The propagation of energy is, then, an essential aspect of wave propagation.

2.3.1. Dilatational and rotational wave equations

Elastic homogeneous medium is considered so that the elastic moduli are constant throughout the body. In this context, the body forces are to be neglected. Navier's equations in the absence of body forces are

$$\mu u_{i,jj}+(\lambda+\mu)u_{j,ji}=\rho\ddot{u}_i \tag{2.22}$$

Taking the divergence of equation (2.22) yield the scalar equation

$$\mu u_{i,jji}+(\lambda+\mu)u_{j,jii}=\rho\ddot{u}_{i,i}$$

which after substitution and reordering of terms involving repeated indices yields

$$\mu u_{k,iik} + (\lambda + \mu) u_{k,kii} = \rho \ddot{u}_{k,k} \text{ or } (\lambda + 2\mu)\Delta_{,ii} = \rho \ddot{\Delta}$$

with the cubic dilatation $\Delta = u_{k,k}$, this equation is rewritten as

$$\Delta_{,ii} = \frac{1}{c_p^2} \rho \ddot{\Delta} \quad \text{or} \quad \frac{\partial^2 \Delta}{\partial x_i \partial x_i} = \frac{1}{c_p^2} \frac{\partial^2 \Delta}{\partial t^2} \tag{2.23}$$

where

$$c_p = \sqrt{\frac{\lambda + 2\mu}{\rho}} \tag{2.24}$$

is the speed of propagation of such dilatational waves, known as the *dilatational wave speed*. From (2.23), the cubic dilatation Δ satisfies the wave equation, known as the *dilatational wave equation.* The Dilatational waves are frequently called *longitudinal waves*, or *irrotational waves*, or in seismology, *P-waves* (where *P* stands for pressure).

Navier equations (2.22) admit another wave-type solution. Taking the rotational of equation (2.22) yields the three equations

$$\mu \varepsilon_{ijk} u_{k,llj} + (\lambda + \mu) \varepsilon_{ijk} u_{l,lkj} = \rho \varepsilon_{ijk} \ddot{u}_{k,j} \tag{2.25}$$

Here ε_{ijk} is the permutation symbol defined in (2.5). The term $u_{l,lkj}$ is symmetric in the indices j and k, whereas the permutation symbol ε_{ijk} is antisymmetric. Hence, the second term appearing in equation (2.25) vanishes. Making use of this result, equation (2.25) reduces to

$$w_{i,jj} = \frac{1}{c_s^2} \ddot{w}_i \quad \text{or} \quad \frac{\partial^2 w_i}{\partial x_j \partial x_j} = \frac{1}{c_s^2} \frac{\partial^2 w_i}{\partial t^2} \tag{2.26}$$

where

$$c_s = \sqrt{\frac{\mu}{\rho}} \tag{2.27}$$

is the *shear speed*. Equation (2.26) is the three-dimensional wave equation known as transverse waves, or shear waves, or S-waves. The quantity w_i is the vector rotation of the displacement field

$$w_i = \frac{1}{2}\varepsilon_{ijk}u_{k,j} = \frac{1}{2}\varepsilon_{ijk}W_{kj} \quad , \quad W_{ij} = \frac{1}{2}(u_{i,j} - u_{j,i}) \tag{2.28}$$

Here W_{ij} is the skew-symmetric part of the displacement gradient $u_{k,j}$ known as the infinitesimal *rotation tensor*.

2.3.2. Helmholtz representation

The results presented in the previous section can also be found in an alternative way known as Helmholtz decomposition. The vector field u_i can be expressed as the sum of the gradient of a scalar field v_i and the curl of a vector field (divergence-free) w_i

$$u_i = v_i + w_i = \phi_{,i} + \varepsilon_{ijk}H_{k,j} \quad \text{or} \quad \underset{\sim}{u} = \nabla\phi + \nabla\times\underset{\sim}{H} \tag{2.28}$$

and

$$H_{k,k} = 0 \quad \text{or} \quad \nabla\cdot\underset{\sim}{H} = 0 \tag{2.29}$$

Direct calculation show that $u_{i,i} = 0$ and $\varepsilon_{ijk}v_{k,j} = 0$. In other words, u_i has been decomposed into the sum of an *irrotational* vector v_i and a *solenoidal* vector w_i.

The case where u_i is solenoidal ($v_i = 0$) and $u_i = w_i$, Navier's equations (2.25) reduce to

$$u_{i,jj} = \frac{\rho}{\mu}\ddot{u}_i \tag{2.30}$$

which is the wave equation governing shear waves or equivoluminal waves. The case where the displacement is irrotational ($w_i = 0$) and $u_i = v_i$, can be found by rewriting (2.25) in the equivalent form

$$u_{i,jj} = \frac{\rho}{\lambda + 2\mu} \ddot{u}_i \tag{2.31}$$

which is the dilatational wave equation. Consequently, an arbitrary displacement can be regarded as the sum of equivoluminal and dilatational waves. Equations (2.30) and (2.31) are independent of each other, which mean that the longitudinal and shear waves propagate without interaction in unbounded media.

2.4. Guided waves

In comparison, a bulk wave travels in an infinite media, for which boundaries do not influence wave propagation. Hence they travel in the bulk of the material. Guided waves are waves that propagate within the boundaries of a structure. The boundaries not only influence the propagation but they guide the wave along the structure. Bulk and guided waves are governed by the same set of partial differential equations. The difference in mathematical solution is that guided waves must satisfy some additional boundary conditions [Giurgiutiu, 2007]. The difficulty in the application of guided waves arises from the complexity of the solution. Guided waves are characterized by an infinite number of modes associated with a given partial differential equation solution. The basic principles of guided waves are very well known, and several textbooks discuss the topics [Giurgiutiu, 2007]; [Graff, 1991]; [Brekhovskikh, 1980].

In this thesis, the guided waves propagation in plates will be considered.

2.4.1. Guided waves in plates

The elastic wave propagation theory in plates has been built-up over one hundred years. The propagation of waves in isotropic plates with free boundary conditions was first studied by Lamb [Lamb, 1917] after whom the guided waves in free plates are named. His study analyzed symmetric and anti-symmetric modes separately. In 1945 Rayleigh and Lindsay investigated the wave propagation in isotropic plates with free boundary conditions [Rayleigh and Lindsay, 1945]. In their works, the Rayleigh-Lamb equations were developed, which identified the relationship between wave frequency and wave number

under certain conditions. A comprehensive analysis and contribution to the understanding of guided waves in plates were given by Victorov [Victorov, 1970], Achenbach [Achenbach, 1973], Graff [Graff, 1991], Rose [Rose, 2014] and Royer and Dieulesaint [Royer and Dieulesaint, 2000]. Some examples of guided wave problems that have been solved and whose solution has inherited the name of the investigator are Rayleigh waves, Lamb waves, Love waves, and Shear horizontal waves. A brief description is listed as follows:

2.4.1.1 Rayleigh waves

Rayleigh waves, as the most straightforward wave, propagate on the free surface of a semi-infinite solid [Ostachowicz et al, 2011]. In these waves, the particle motion is composed of elliptical movements in the $x\,y$ vertical plane and of motion parallel to the direction of propagation x (as shown in Figure 2.2). The motion amplitude decreases rapidly with depth y starting from the wave crest. The Rayleigh waves are very sensitive to surface defects with very little penetration in the depth of the solid [Hirao and Ogi, 1999]. For this reason, they can be used to inspect the surface properties for a structure.

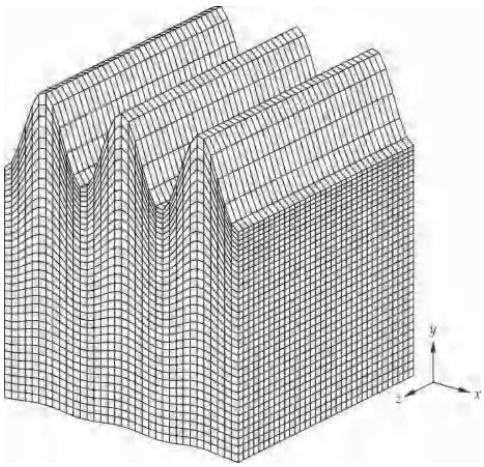

Figure 2.2: Rayleigh wave [Ostachowicz et al, 2011].

2.4.1.2 Lamb waves

Lamb waves are waves that are guided between two parallel free surfaces, such as the upper and lower surfaces of a plate (Figure 2.3). These waves can

only be generated in thin-walled structures so that the motion amplitude remains the same on both top and bottom surfaces only. Therefore Lamb waves are of two basic varieties, symmetric Lamb-waves modes and antisymmetric Lamb-wave modes [Hirao and Ogi, 1999]; [Ostachowicz et al, 2011]. Unlike the Rayleigh waves, the Lamb waves are highly dispersive, and their speed is related to their frequency and plate thickness.

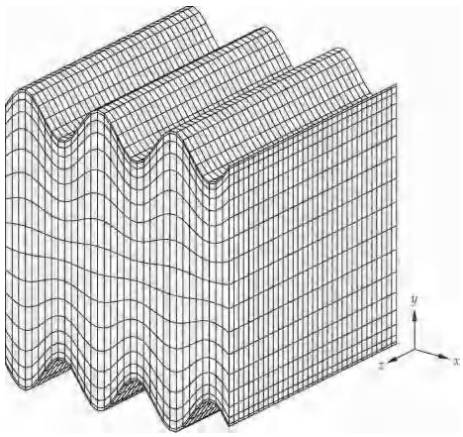

Figure 2.3: Lamb wave [Ostachowicz et al, 2011].

2.4.1.3 Love waves

Love waves are another kind of surface waves applied for surface inspection. These waves were firstly found by Love in 1911 and verified by many researchers. Their particle motion is horizontal (in the $x\,z$ plane) and perpendicular to the direction of propagation x. As in the case of Rayleigh waves, their wave amplitude decreases rapidly with depth (Figure 2.4).

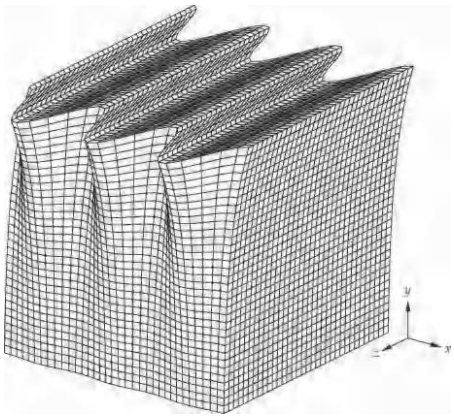

Figure 2.4: Love wave [Ostachowicz et al, 2011].

2.4.1.4 Shear horizontal waves

Shear horizontal (SH) waves are characterized by particle motion maintained in the $x\,z$ horizontal plane, as their name explained. The direction of the particle motion is perpendicular to the direction of wave propagation x (Figure 2.5). The SH waves can be symmetric and antisymmetric. Except for the very fundamental mode, the SH wave modes are all dispersive. The advantage of applied SH waves on structural health monitoring is summarized by Petcher et al. [Petcher et al, 2013].

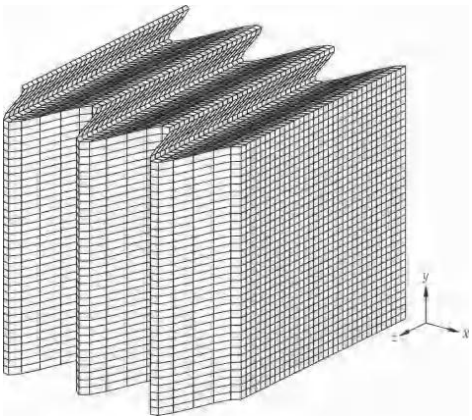

Figure 2.5: Horizontal shear wave [Ostachowicz et al, 2011].

2.4.2. Shear horizontal wave in plate

Shear horizontal waves have a particle motion contained in a plane parallel to the surface of the plate ($x\,z$). The axes definition is shown in Figure 2.6. The x axis is placed along the direction of wave propagation, whereas the z axis is perpendicular to it. [Giurgiutiu, 2007]

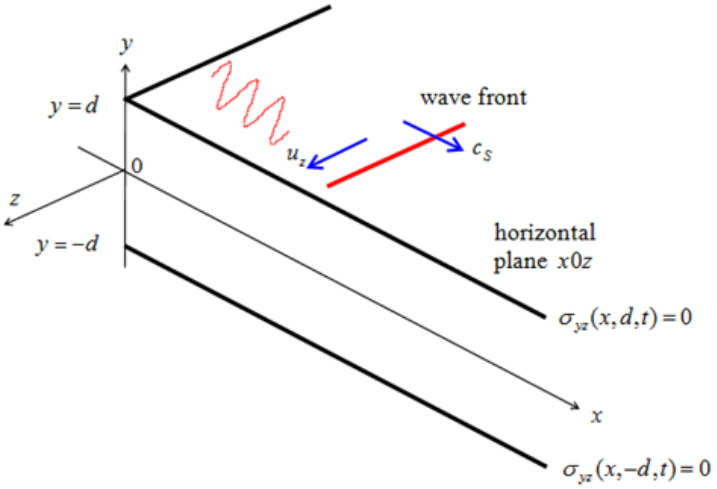

Figure 2.6: Particle motion and coordinate definition for SH plate waves [Giurgiutiu, 2007].

2.4.2.1 General equation

The SH mode can be considered as the superposition of waves reflecting from the upper and lower surfaces of the plate, polarized horizontally (in the z axis direction). The problem is assumed to be z-invariant, i.e., $\frac{\partial(\,)}{\partial z}=0$. Particle motion has only a U_z component and if U_z is independent of z, then equation (2.26) reduces to:

$$\nabla^2 U_z = \frac{1}{c_s^2}\ddot{U}_z \quad \text{or} \quad \frac{\partial^2 U_z}{\partial x^2}+\frac{\partial^2 U_z}{\partial y^2}=\frac{1}{c_s^2}\frac{\partial^2 U_z}{\partial t^2} \tag{2.32}$$

where $U_z = w_3$

It is assumed that the particle motion has the form

$$U_z(x,y,t) = f(y)e^{i(kx-\omega t)} \tag{2.33}$$

This form of the solution is chosen because it represents a wave motion propagating in the x direction (due to the exponential term $e^{i(kx-\omega t)}$) and has a fixed distribution in the y direction (standing waves across the thickness d). Notice that U_z is independent of z, so that the problem is assumed z-invariant.

Substitution of equation (2.33) into equation (2.32) and division of both sides by $e^{i(kx-\omega t)}$ yields

$$\frac{\partial^2 f(y)}{\partial x^2}+\left(\frac{\omega^2}{c_s^2}-k^2\right)f(y)=0 \tag{2.34}$$

The solution of equation (2.34) has the general form

$$f(y)=A\sin(\eta y)+B\cos(\eta y) \tag{2.35}$$

Where η is defined as

$$\eta^2=\frac{\omega^2}{c_s^2}-k^2 \tag{2.36}$$

and A, B are arbitrary constants. The general form of the displacement field is therefore

$$U_z(x,y,t)=\left[A\sin(\eta y)+B\cos(\eta y)\right]e^{i(kx-\omega t)} \tag{2.37}$$

The boundary conditions state that the upper and lower plate surfaces are traction free

$$\sigma_{yz}(x,\pm d,t)=\mu\frac{\partial U_z}{\partial y}(x,\pm d,t)=0 \tag{2.38}$$

Without going into details [Giurgiutiu, 2007], Boundary conditions (2.38) lead to the dispersion equations characterized by the system of linear homogeneous equations with the determinant

$$\sin(\eta d)\cos(\eta d)=0 \tag{2.39}$$

Equation (2.39) is the characteristic equation of SH wave modes and is zero when either:

$$\sin(\eta d)=0 \tag{2.40}$$

which corresponds to symmetric modes (S-modes) of the SH waves, or:

$$\cos(\eta d) = 0 \tag{2.41}$$

which corresponds to antisymmetric modes (A-modes) of the SH waves. By virtue of the simplicity of the solution, explicit solutions of equations (2.40) and (2.41) are

$$\begin{aligned} \eta^S d &= n\pi, \quad n = 0, 1, 2, ... \\ \eta^A d &= \frac{n\pi}{2}, \quad n = 1, 3, 5, ... \end{aligned} \tag{2.42}$$

The values $\eta^S d$ and $\eta^A d$ given by equations (2.42) are the Eigenvalues for symmetric and antisymmetric motions. The solutions to equations (2.40) and (2.41) can be written as

$$\eta d = \frac{n\pi}{2} \tag{2.43}$$

where $n \in \{0, 2, 4, ...\}$ for symmetric SH modes and $n \in \{1, 3, 5, ...\}$ for antisymmetric SH modes. After substitutions, the general solution (2.33) becomes

$$U_z^S(x, y, t) = B\cos\frac{n\pi}{2d} y e^{i(kx-\omega t)} \tag{2.44}$$

for symmetric SH waves (S-modes), and

$$U_z^A(x, y, t) = A\sin\frac{n\pi}{2d} y e^{i(kx-\omega t)} \tag{2.45}$$

For antisymmetric SH waves (A-modes).

A sketch of the symmetric SH modes (S_0, S_1, S_2) and antisymmetric SH modes (A_0, A_1, A_2) are illustrated in Figure 2.7.

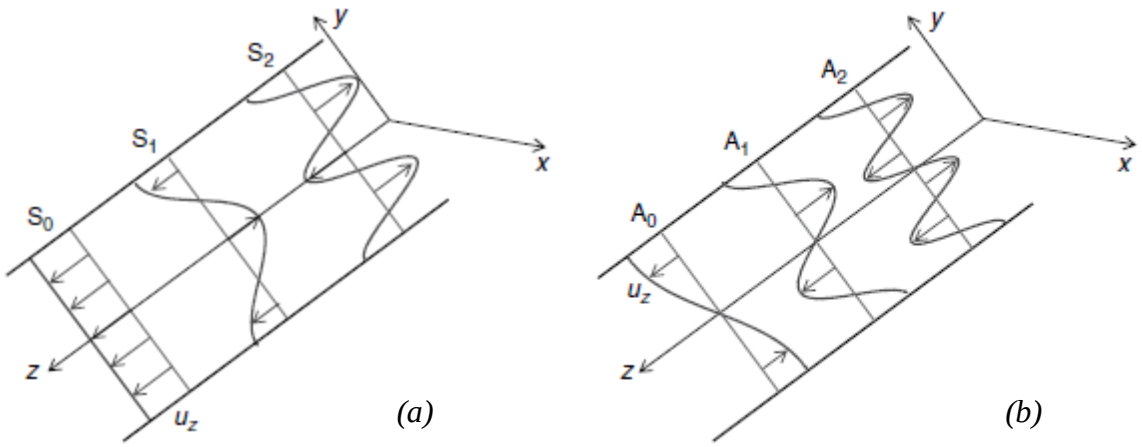

Figure 2.7: SH waves, (a) symmetric modes, (b) Anti-symmetric modes. [Giurgiutiu, 2007].

2.4.2.2 Dispersion of SH waves

By using the definition of the wave number

$$k = \frac{\omega}{c_p} \tag{2.46}$$

where c_p is the mode phase velocity

The dispersion equation (2.36) can be written as

$$\frac{\omega^2}{c_s^2} - \frac{\omega^2}{c_p^2} = \left(\frac{n\pi}{2d}\right)^2 \tag{2.47}$$

Equation (2.47) can be solved for the phase velocity c_p in terms of the frequency thickness product $2fd$ (where $\omega = 2\pi f$)

$$c_p = 2c_s \left\{ \frac{2fd}{\sqrt{4(2fd)^2 - n^2 c_s^2}} \right\} \tag{2.48}$$

It should be noted that when $n = 0$, corresponding to the first symmetric mode SH_0, the phase velocity c_p is equal to c_s, so the SH_0 wave mode is not dispersive and propagates at the shear wave speed c_s. For all other SH modes ($n > 0$) the phase velocity is varying with the frequency-thickness product. This phenomenon is called *dispersion,* and results in the distortion of the shape of the wave packet

containing multiple frequencies that propagates for long distances. The first five SH modes of the phase velocity dispersion curves over a frequency thickness range of 0-14 MHz-mm, are plotted in Figure 2.8. The solid and dashed curves represent the symmetric and antisymmetric modes respectively.

The cutoff frequencies of the SH modes which correspond to infinite phase velocities can be found by setting the denominator in equation (2.48) equal to zero. The *n*th cutoff frequency is given by

$$\left(2fd\right)_n = \frac{nc_s}{2} \tag{2.49}$$

It should be noted that , even integer n represents *symmetric* modes and odd integer n represents antisymmetric modes.

Figure 2.8 also indicates the asymptotic behavior of the phase velocity. All the SH modes converge to c_s as the frequency thickness product becomes large. In this example $c_s = 3.1\,mm/\mu s$ for aluminum plate.

The phase velocity represents the velocity at which a mode at a given frequency is traveling in a medium. If this mode is dispersive, then the group velocity is associated with the propagation velocity of a group of waves of similar frequency.

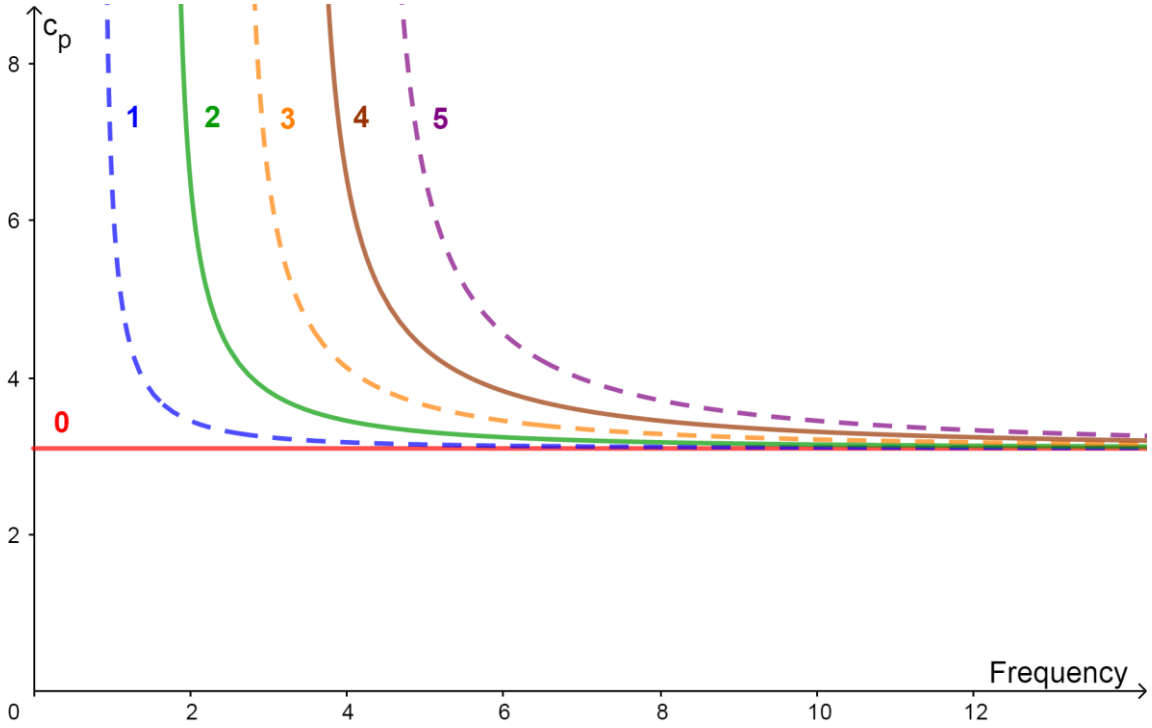

Figure 2.8: Phase velocity dispersion curves for SH modes.

The group velocity corresponds to the velocity at which the energy of a multi frequency wave packet is traveling.

Solving the dispersion equation for the quantity $\frac{d\omega}{dk} = c_g$ (by definition, the group velocity), it can be shown [Rose, 1999], that the group SH wave velocities can be expressed as :

$$c_g = c_s \sqrt{1 - \frac{\left(\frac{n}{2}\right)^2}{\left(\frac{2fd}{c_s}\right)^2}} \qquad (2.50)$$

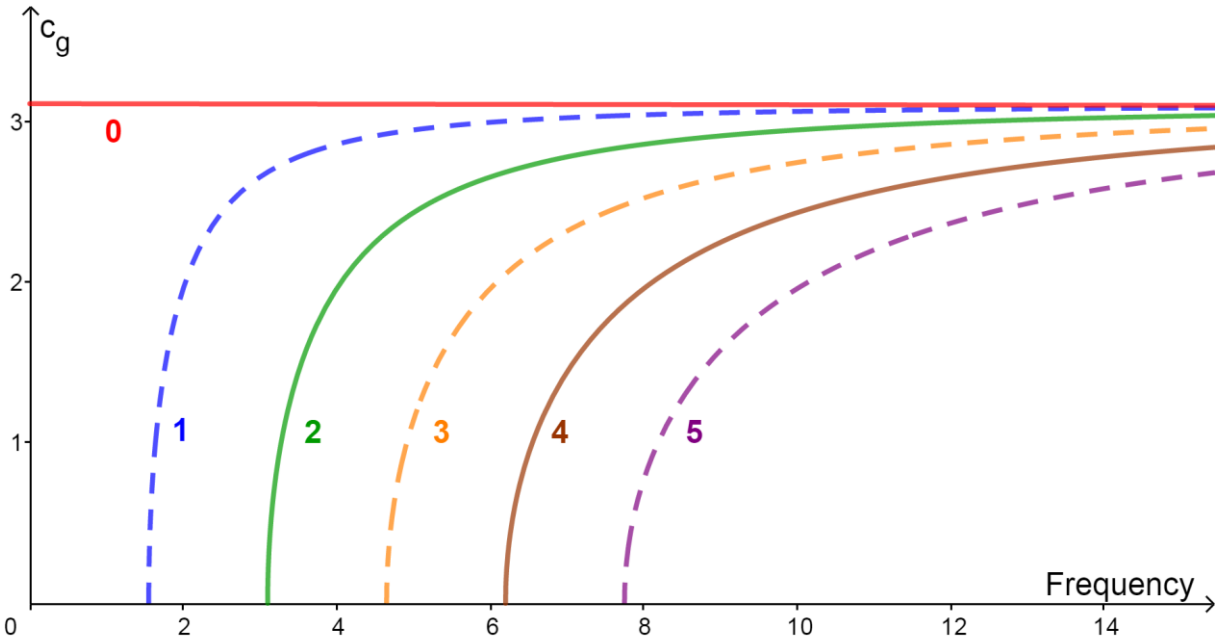

Figure 2.9: Group velocity dispersion curves for SH modes.

Notice that at cutoff frequencies given by equation (2.49), the group velocity of any mode is zero. As fd approaches infinity for any mode, the group velocity approaches the shear wave c_s. Plots of SH mode group velocity curves are illustrated in Figure 2.9.

2.5. Wave equation in cylindrical and polar coordinates

While Cartesian coordinates are attractive because of their simplicity, there are many problems in mechanics fruitfully analyzed when they are modeled as having particular geometry and various symmetries, such as cylindrical symmetry. When looking for waves with some chosen geometry, it is advantageous to get at the solutions to the wave equation directly in these coordinates.

2.5.1. Transforming the wave equation

The coordinate independent wave equation

$$\nabla^2 u = \frac{1}{c^2}\frac{\partial^2 u}{\partial t^2} \tag{2.51}$$

can take on different forms, depending upon the coordinate system in use. In Cartesian coordinates, the Laplacian ∇^2 is expressed as

$$\nabla^2 = \frac{\partial^2}{\partial x^2} + \frac{\partial^2}{\partial y^2} + \frac{\partial^2}{\partial z^2} \tag{2.52}$$

To express (2.52) in cylindrical coordinates (r, θ, z), a point with Cartesian coordinates (x, y, z) as shown in Figure 2.10 is given by

$$\begin{aligned} r &= \sqrt{x^2 + y^2} \\ \theta &= \tan^{-1}\left(\frac{x}{y}\right) \end{aligned} \tag{2.53}$$

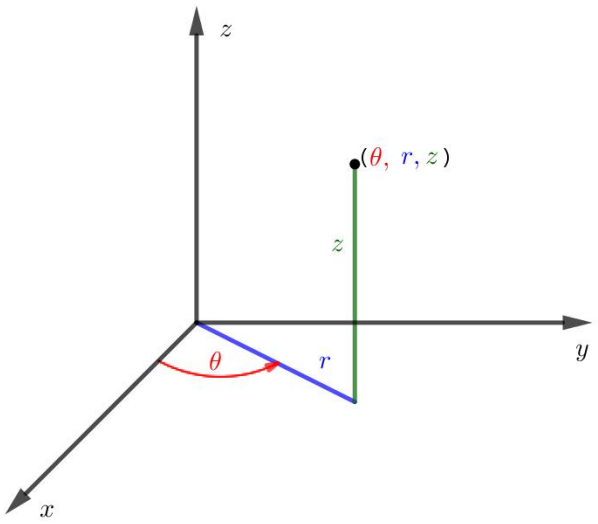

Figure 2.10: Illustration of cylindrical coordinates.

After manipulations given in several mathematical books, the Laplacian in cylindrical coordinates is given by

$$\nabla^2 = \frac{\partial^2}{\partial r^2} + \frac{1}{r}\frac{\partial}{\partial r} + \frac{1}{r^2}\frac{\partial^2}{\partial \theta^2} + \frac{\partial^2}{\partial z^2} \tag{2.54}$$

Thus, in cylindrical coordinates the wave equation becomes

$$\frac{1}{r}\frac{\partial}{\partial r}\left(r\frac{\partial u}{\partial r}\right)+\frac{1}{r^2}\frac{\partial^2 u}{\partial \theta^2}+\frac{\partial^2 u}{\partial z^2}=\frac{1}{c^2}\frac{\partial^2 u}{\partial t^2} \tag{2.55}$$

2.5.2. Separation of variables in cylindrical coordinates

The method of separation of variables can be used to obtain the solution of equation (2.55). Assuming that

$$u(r,\theta,z,t)=R(r)\,\Phi(\theta)\,Z(z)\,T(t) \tag{2.56}$$

and substituting this trial solution into the wave equation, and then dividing the resulting equation by u to find

$$\frac{1}{r}\frac{(rR')'}{R}+\frac{1}{r^2}\frac{\Phi''}{\Phi}+\frac{Z''}{Z}=\frac{1}{c^2}\frac{T''}{T} \tag{2.57}$$

The separation of variables is seen from this equation: the right hand side is a function of t only while the left hand side is a function of (r,θ,z). Thus both sides must equal a constant $(-k^2)$. The resulting equation for T can be solved

$$T''=-c^2k^2T \tag{2.58}$$

through

$$T=Ae^{ickt} \tag{2.59}$$

where the complex form for the solution is used and, as usual, the real part of the solution will be taken into account.

Equation (2.57) is reduced to the form

$$\frac{1}{r}\frac{(rR')'}{R}+\frac{1}{r^2}\frac{\Phi''}{\Phi}=-k^2-\frac{Z''}{Z} \tag{2.60}$$

which equates a function of r and θ with a function of z. The left and right hand sides must therefore equal to a constant $(-a^2)$

$$\frac{Z''}{Z}=a^2-k^2 \tag{2.61}$$

The solution to (2.61) is of the form

$$Z = Be^{i\sqrt{a^2-k^2}z} \tag{2.62}$$

The remaining equation is then

$$r\frac{(rR')'}{R} + a^2r^2 = -\frac{\Phi''}{\Phi} \tag{2.63}$$

Both sides of this equation must equal a constant (b^2)

$$\Phi'' + b^2\Phi = 0 \tag{2.64}$$

With the harmonic solution of 2π period that forces b to be an integer n

$$\Phi(\theta) = c\sin(\mathrm{n}\,\theta) + d\cos(\mathrm{n}\,\theta) \tag{2.65}$$

Finally (2.63) must be solved for R

$$R'' + \frac{1}{r}R' + \left(a^2 - \frac{n^2}{r^2}\right)R = 0 \tag{2.66}$$

This equation is known as *Bessel's equation*. Its two linearly independent solutions are known as *Bessel functions* $J_n(r)$ and $Y_n(r)$ of the first and second kind, respectively (Figure 2.11 and Figure 2.12). The subscript n is known as the order of the Bessel function. As Bessel functions of the second kind exhibit a singularity in the origin $r = 0$, this branch of solutions is discarded.

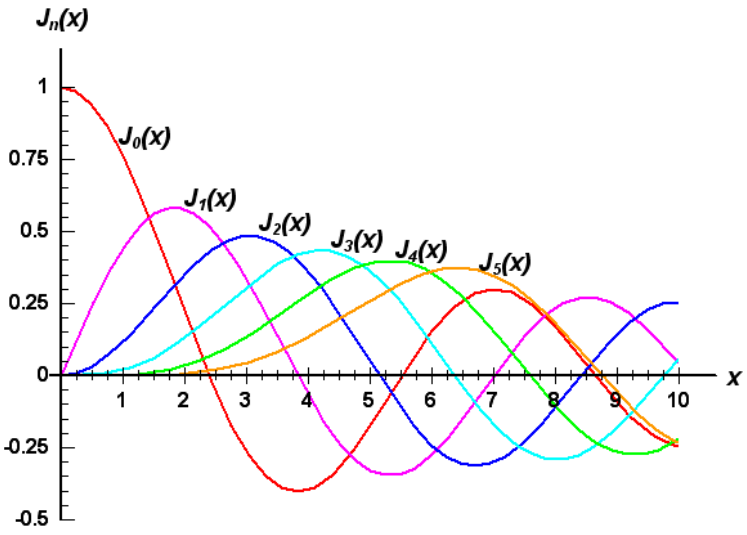

Figure 2.11: Bessel functions of the first kind

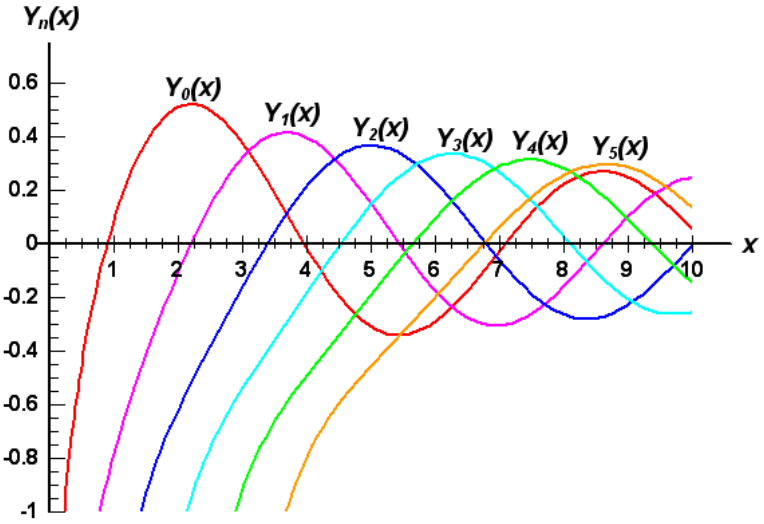

Figure 2.12: Bessel functions of the second kind

2.6. Summary

This chapter presented a review of the fundamental concepts of elastic wave propagation in elastic media. The general equations of 3-D wave propagation in unbounded solid media were developed. Two types of wave in unbounded media were identified and discussed: Pressure wave and shear wave. Both Navier and Helmholtz methods were used to determine the dilatational and rotational wave equations. The chapter ended with a description of guided waves in plates. The simple case of SH waves in plate has been considered. The concept of dispersion and basic information on guided SH wave have been reported. The use of polar and cylindrical coordinates to model the beveled plate showed the suitability for the investigation purpose.

Chapter 3

Formulation of SH waves in beveled free end plate

Chapter 3

Formulation of SH waves in beveled free end plate

3.1. Introduction

In the present chapter the problem of Horizontally Shear wave propagation in a beveled free end plate is considered. The plate is assumed to be linearly elastic, homogeneous and isotropic. Based on the application of the method of separation of variables (also known as the wave function expansion technique), a series solution is derived. The analyzed plate is divided into two regions by introducing a semi-circular fictitious common boundary. In each region, the displacement field can be expressed as an infinite sum of appropriate wave functions satisfying partial boundary conditions, respectively. The total solution is assembled by enforcing the continuity conditions at the common interface. The solution technique proposed realizes a great reduction in the computational achievement [Mohammedi et al, 2019].

3.2. Geometry model of the problem

The wave guide problem to be investigated is shown in Figure 3.1. It is shown a portion of a structure which represents a plate of uniform thickness d having a bevel angle α. The plate is bounded on the three sides by traction-free surfaces denoted Γ_1, Γ_2 and Γ_3, and is assumed to be made of homogeneous, elastic, and isotropic material.

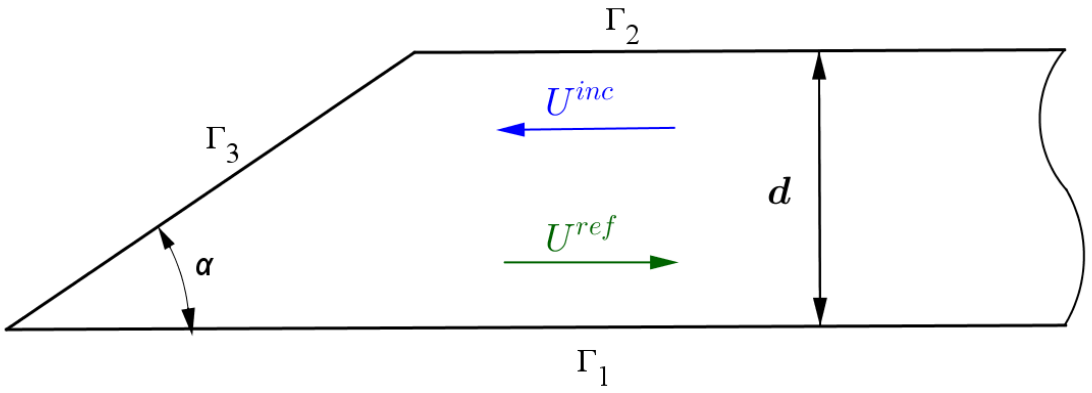

Figure 3.1: The plate structure geometry showing incident and reflected waves

Since this work deals with horizontal shear SH guided waves, the only material properties which are taken into account are the plate shear modulus μ and the density ρ. The coordinate systems, the extent of regions I and II, and their common artificial boundary Γ_4 are all depicted in Figure 3.2.

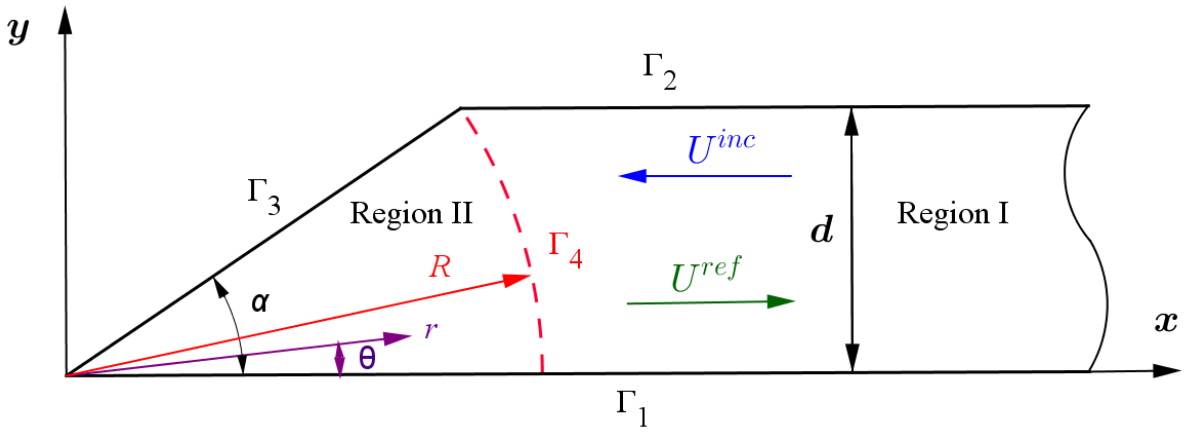

Figure 3.2: Partitioned wedge-plate regions and common fictitious boundary.

A Cartesian coordinate system, for region I, is constructed where its origin is located at the tip of the beveled end, the positive x-axis is aligned with the lower surface, and the y-axis increases upwards. The origin of the Cartesian coordinates also serves as the origin of the polar coordinates system for region II. The polar angle θ increases counterclockwise starting at the positive x-axis and ending at the beveled edge Γ_3.

The radius of the polar coordinates r as shown in Figure 3.3 has a maximum value :

$$R = \frac{d}{\sin\alpha} \tag{3.1}$$

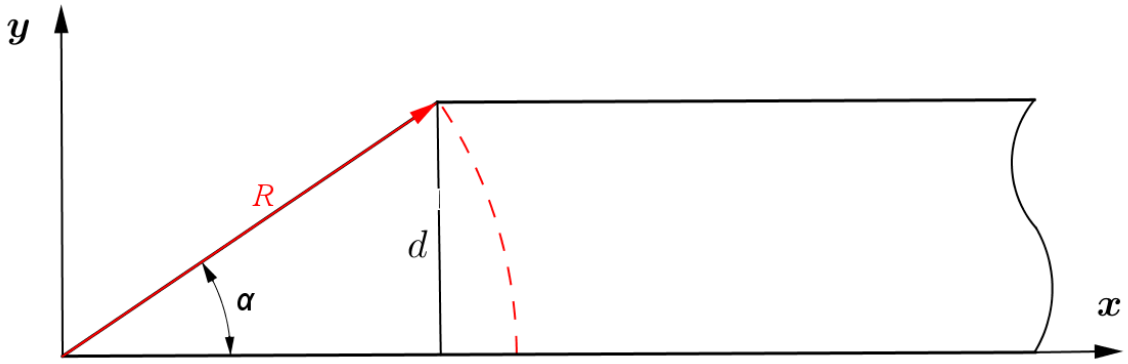

Figure 3.3: Maximum value of radius r.

3.3. Formulation of reflected waves from a beveled free end

The waves studied here are assumed to be time harmonic SH waves propagating in the x-direction of Figure 3.1. It is to be noted that for such type of waves, no dependence on z occurs. In the domain of the plate, the displacement field which is the only non-vanishing component is given by U_z. As illustrated in Figure 3.1, an incident SH wave travelling in the negative x-direction impinges on the beveled free end of the plate and reflects back in the positive x-direction. The corresponding displacement field U_z in the plate is made of incident U_z^{inc} and the reflected U_z^{ref} displacements fields,

$$U_z = U_z^{inc} + U_z^{ref} \tag{3.2}$$

3.3.1. Equations of motion

The geometry of the plate admits an equivalent formulation whereby the plate is divided into two regions as shown in Figure 3.2, and the incident SH

wave travelling in Region I impinges on the artificial boundary Γ_4, reflects and sets up a standing wave in the bounded Region II. The solutions for the out-of-plane, time-dependent particle displacement fields U_z^I and U_z^{II}, in regions I and II respectively, are governed by the following wave equations, which are derived from the Navier equations in Cartesian coordinates by (2.30)

$$\frac{\partial^2 U_z^I}{\partial x^2}+\frac{\partial^2 U_z^I}{\partial y^2}=\frac{1}{c_s^2}\frac{\partial^2 U_z^I}{\partial t^2} \tag{3.3}$$

and, in cylindrical coordinates by (2.55)

$$\frac{\partial^2 U_z^{II}}{\partial r^2}+\frac{1}{r}\frac{\partial U_z^{II}}{\partial r}+\frac{1}{r^2}\frac{\partial^2 U_z^{II}}{\partial \theta^2}=\frac{1}{c_s^2}\frac{\partial^2 U_z^{II}}{\partial t^2} \tag{3.4}$$

where

$$c_s=\sqrt{\frac{\mu}{\rho}} \tag{3.5}$$

is the shear velocity as defined by equation (2.27), while t denotes time.

3.3.2. Continuity conditions

The interface continuity of displacement and stress conditions on the fictitious boundary Γ_4 are given by

$$U_z^I=U_z^{II} \quad ; \quad r=R,\ x=R\cos\theta,\ y=R\sin\theta \tag{3.6}$$

$$\sigma_{nz}^I=\sigma_{rz}^{II} \quad ; \quad r=R,\ x=R\cos\theta,\ y=R\sin\theta \tag{3.7}$$

σ_{nz}^I is the shear stress at the boundary region I and is given by the Cauchy stress formula (2.13)

$$\sigma_{nz}^I=t_3^{I(n)}=\sigma_{3j}^I n_j=\sigma_{31}^I n_1+\sigma_{32}^I n_2 \tag{3.8}$$

Where n_1 and n_2 are the direction cosine of the outward unit normal vector $\underset{\sim}{n}$ along the boundary Γ_4

For convenience the expression (3.8) can be rewritten in (x, y, z) notation as

$$\sigma_{nz}^{I} = \sigma_{xz}^{I} \cos\theta + \sigma_{yz}^{I} \sin\theta \tag{3.9}$$

σ_{rz}^{II} is the shear stress in region II (Figure 3.4) given by the strain- stress relationship

$$\sigma_{rz}^{II} = \mu \frac{\partial u_z^{II}}{\partial r} \tag{3.10}$$

3.3.3. Boundary conditions

The traction-free boundary conditions on traction free sides of the plate are given by:

$$\sigma_{yz}^{I} = 0, \quad y = 0, d \tag{3.11}$$

$$\sigma_{\theta z}^{II} = 0, \quad \theta = 0, \alpha \tag{3.12}$$

Where σ_{yz}^{I} is the out-of-plane shear stress acting on the two boundaries, Γ_1 and Γ_2 of region I, while $\sigma_{\theta z}^{II}$ is the out-of-plane shear stress acting on the two boundaries, Γ_1 and Γ_3 of region II (Figure 3.4).

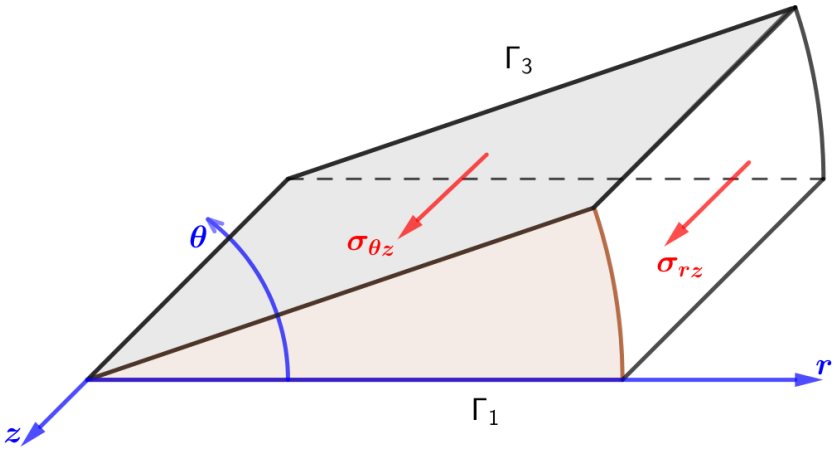

Figure 3.4: Stresses in polar coordinates in region II

3.3.4. Helmholtz equations

The SH waves are assumed to be time harmonic, and hence the out-of-plane z-displacement fields in regions I and II are given by,

$$U_z^I = u_z^I(x,y)e^{i\omega t} \tag{3.13}$$

$$U_z^{II} = u_z^{II}(r,\theta)e^{i\omega t} \tag{3.14}$$

where u_z is the particle displacement, ω is the applied frequency and $i^2 = -1$. Substituting equation (3.13) and equation (3.14) into equations (3.3) and (3.4), respectively, results to the steady state form of the governing equations in each region

$$\frac{\partial^2 u_z^I}{\partial x^2} + \frac{\partial^2 u_z^I}{\partial y^2} = -\frac{\omega^2}{c_s^2} u_z^I \tag{3.15}$$

$$\frac{\partial^2 u_z^{II}}{\partial r^2} + \frac{1}{r}\frac{\partial u_z^{II}}{\partial r} + \frac{1}{r^2}\frac{\partial^2 u_z^{II}}{\partial \theta^2} = -\frac{\omega^2}{c_s^2} u_z^{II} \tag{3.16}$$

Equation (3.15) and equation (3.16) are also known as the *Helmholtz equations* in rectangular and cylindrical coordinates, respectively. The geometry of the regions renders the solutions of these equations as separable.

3.3.5. Solution to Helmholtz equations

The solution to the Helmholtz equations represents the reflected waves which can be expressed as an infinite sum of wave functions.

$$u_z^{I\,ref}(x,y) = \sum_{m=0}^{\infty} A_m \cos\left(\frac{m\pi}{d} y\right) e^{ik_m x} \tag{3.17}$$

The total solution in region I is expressed in terms of a single incident mode of order q and all the reflected modes expressed as an infinite sum of wave functions represented by equation (3.17)

$$u_z^I(x,y) = C_q \cos\left(\frac{q\pi}{d} y\right) e^{-ik_q x} + \sum_{m=0}^{\infty} A_m \cos\left(\frac{m\pi}{d} y\right) e^{ik_m x} \tag{3.18}$$

where C_q is the amplitude of the q^{th} incident mode and A_m is the amplitude of the m^{th} reflected mode. Note, each term of the series solution in equation (3.18) satisfies the traction free boundary condition in equation (3.11) along Γ_1 and Γ_2 Because only displacements according to z are considered in the shear problem, the displacement field does not depend on z. The first two symmetric wave modes $q=0,2$ (solid curves) and antisymmetric wave modes $q=1,3$ (dashed curves) with respect to the mid surface $y=\frac{d}{2}$ of the displacement field are displayed in Figure 3.5.

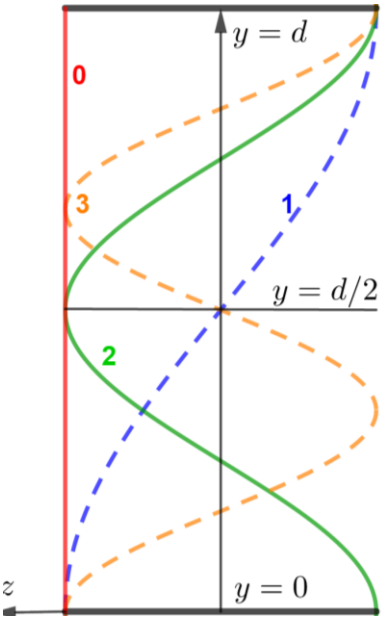

Figure 3.5: The y-variation of displacement for the first two symmetric and antisymmetric SH modes.

The wave numbers k_m and k_q are defined by equation (2.47) as,

$$k_m = \sqrt{\frac{\omega^2}{c_s^2} - \frac{m^2\pi^2}{d^2}} \tag{3.19}$$

$$k_q = \sqrt{\frac{\omega^2}{c_s^2} - \frac{q^2\pi^2}{d^2}} \tag{3.20}$$

Similarly, the separable solution of equation (3.16) is represented as an infinite Bessel-Fourier sum,

$$u_z^{II}(r,\theta) = \sum_{n=0}^{\infty} B_n \cos\left(\frac{n\pi}{\alpha}\theta\right) J_{\frac{n\pi}{\alpha}}(k_0 r) \tag{3.21}$$

Each term of the Fourier series in equation (3.21) satisfies the traction free boundary conditions (3.12) along Γ_1 and Γ_3. B_n denotes the n^{th} amplitude of the standing wave in region II, $J_{\frac{n\pi}{\alpha}}$ is the Bessel function of the first kind of order $\frac{n\pi}{\alpha}$, and k_0 is defined as

$$k_0 = \frac{\omega}{c_s} \tag{3.22}$$

The stress field in region I is given by,

$$\sigma_{xz}^I = \mu\left(\frac{\partial u_z^I}{\partial x}\right) = \mu\left[-ik_q C_q \cos\left(\frac{q\pi}{d}y\right)e^{-ik_q x} + \sum_{m=0}^{\infty} ik_m A_m \cos\left(\frac{m\pi}{d}y\right)e^{ik_m x}\right] \tag{3.23}$$

and

$$\sigma_{yz}^I = \mu\left(\frac{\partial u_z^I}{\partial y}\right) = \mu\left[-\frac{q\pi}{d} C_q \sin\left(\frac{q\pi}{d}y\right)e^{-ik_q x} + \sum_{m=0}^{\infty} -\frac{m\pi}{d} A_m \sin\left(\frac{m\pi}{d}y\right)e^{ik_m x}\right] \tag{3.24}$$

It must be remarked that, as shear waves involve only displacements along z-direction, the stress components are only σ_{xz} and σ_{yz}

The stress field along the boundary Γ_4 represented by equation (3.9) is given by

$$\begin{aligned}\sigma_{nz}^I = {} & \mu\left[-ik_q C_q \cos\left(\frac{q\pi}{d}y\right)e^{-ik_q x} + \sum_{m=0}^{\infty} ik_m A_m \cos\left(\frac{m\pi}{d}y\right)e^{ik_m x}\right]\cos\theta + \\ & \mu\left[-\frac{q\pi}{d} C_q \sin\left(\frac{q\pi}{d}y\right)e^{-ik_q x} + \sum_{m=0}^{\infty} -\frac{m\pi}{d} A_m \sin\left(\frac{m\pi}{d}y\right)e^{ik_m x}\right]\sin\theta\end{aligned} \tag{3.25}$$

Additionally, the stress field in region II is given by

$$\sigma_{rz}^{II} = \mu\left(\frac{\partial u_z^{II}}{\partial r}\right) = \mu\sum_{n=0}^{\infty} k_0\ B_n \cos\left(\frac{n\pi}{\alpha}\theta\right)\frac{\partial J_{\frac{n\pi}{\alpha}}}{\partial r}\left(k_0 r\right) \tag{3.26}$$

Substituting the series solutions (3.18), (3.21), (3.25) and (3.26) into the continuity equations (3.6), (3.7), and transposing the known incident terms to the right hand side, the displacement and stress continuity conditions are now expressed as,

$$\sum_{m=0}^{M} A_m \cos\left(\frac{m\pi}{d}y\right)e^{ik_m x} - \sum_{n=0}^{N} B_n \cos\left(\frac{n\pi}{\alpha}\theta\right) J_{\frac{n\pi}{\alpha}}\left(k_0 R\right) = -C_q \cos\left(\frac{q\pi}{d}y\right)e^{-ik_q x} \tag{3.27}$$

$$\begin{aligned} &\sum_{m=0}^{M} A_m\left[ik_m \cos\left(\frac{m\pi}{d}y\right)\cos\theta - \frac{m\pi}{d}\sin\left(\frac{m\pi}{d}y\right)\sin\theta\right]e^{ik_m x} \\ &-\sum_{n=0}^{N} B_n\ k_0 \cos\left(\frac{n\pi}{\alpha}\theta\right)\frac{\partial J_{\frac{n\pi}{\alpha}}}{\partial r}\left(k_0 R\right) = C_q\left[ik_q \cos\left(\frac{q\pi}{d}y\right)\cos\theta + \frac{q\pi}{d}\sin\left(\frac{q\pi}{d}y\right)\sin\theta\right]e^{-ik_q x} \end{aligned} \tag{3.28}$$

It should be noted that when dealing with numerical procedures it is necessary to limit the infinite sums of the series to a finite number of terms M and N. The number of terms, which will be taken into consideration, depends only on the accuracy requirement.

The two matching equations (3.27) and (3.28) are now projected onto $\cos\left(\frac{p\pi}{\alpha}\theta\right)$ as shown below,

$$\begin{aligned} &\int_0^{\alpha}\sum_{m=0}^{M} A_m \cos\left(\frac{p\pi}{\alpha}\theta\right)\cos\left(\frac{m\pi}{d}y\right)e^{ik_m x}d\theta - \int_0^{\alpha}\sum_{n=0}^{N} B_n \cos\left(\frac{p\pi}{\alpha}\theta\right)\cos\left(\frac{n\pi}{\alpha}\theta\right) J_{\frac{n\pi}{\alpha}}\left(k_0 R\right)d\theta \\ &= -C_q\int_0^{\alpha}\cos\left(\frac{p\pi}{\alpha}\theta\right)\cos\left(\frac{q\pi}{d}y\right)e^{-ik_q x}d\theta \end{aligned} \tag{3.29}$$

$$\begin{aligned}
&\int_0^{\alpha}\sum_{m=0}^{M} A_m \cos\left(\frac{p\pi}{\alpha}\theta\right)\left[ik_m \cos\left(\frac{m\pi}{d}y\right)\cos\theta - \frac{m\pi}{d}\sin\left(\frac{m\pi}{d}y\right)\sin\theta\right]e^{ik_m x}d\theta \\
&\qquad -\int_0^{\alpha}\sum_{n=0}^{N} B_n k_0 \cos\left(\frac{p\pi}{\alpha}\theta\right)\cos\left(\frac{n\pi}{\alpha}\theta\right)\frac{\partial J_{\frac{n\pi}{\alpha}}}{\partial r}(k_0 R)\,d\theta \\
&= C_q\int_0^{\alpha}\cos\left(\frac{p\pi}{\alpha}\theta\right)\left[ik_q \cos\left(\frac{q\pi}{d}y\right)\cos\theta + \frac{q\pi}{d}\sin\left(\frac{q\pi}{d}y\right)\sin\theta\right]e^{-ik_q x}d\theta
\end{aligned} \tag{3.30}$$

where

$$\begin{aligned} x &= R\cos\theta \\ y &= R\sin\theta \end{aligned} \tag{3.31}$$

3.3.6. Block matrix representation

After limiting the infinite series properly, this leads to a set of algebraic equations in which the unknown coefficients A_m and B_n may be solved, respectively, after setting C_q to be one. At this stage, the system of equations (3.29) and (3.30) can be expressed by a block matrix representation. For this purpose the terms containing the coefficients A_m, B_n and C_q in (3.29), for displacement, are denoted by:

$$\begin{aligned}
&\int_0^{\alpha}\sum_{m=0}^{M}\cos\left(\frac{p\pi}{\alpha}\theta\right)\cos\left(\frac{m\pi}{d}y\right)e^{ik_m x}d\theta = \mathrm{A}_{pm}^{D} \\
&-\int_0^{\alpha}\sum_{n=0}^{N}\cos\left(\frac{p\pi}{\alpha}\theta\right)\cos\left(\frac{n\pi}{\alpha}\theta\right)J_{\frac{n\pi}{\alpha}}(k_0 R)\,d\theta = \mathrm{B}_{pn}^{D} \\
&-\int_0^{\alpha}\cos\left(\frac{p\pi}{\alpha}\theta\right)\cos\left(\frac{q\pi}{d}y\right)e^{-ik_q x}d\theta = \mathrm{C}_{pq}^{D}
\end{aligned} \tag{3.32}$$

and in (3.30), for the stresses, are denoted by:

$$\int_0^{\alpha}\sum_{m=0}^{M}\cos\left(\frac{p\pi}{\alpha}\theta\right)\left[ik_m\cos\left(\frac{m\pi}{d}y\right)\cos\theta-\frac{m\pi}{d}\sin\left(\frac{m\pi}{d}y\right)\sin\theta\right]e^{ik_m x}d\theta=\mathrm{A}_{pm}^{S}$$

$$-\int_0^{\alpha}\sum_{n=0}^{N}k_0\cos\left(\frac{p\pi}{\alpha}\theta\right)\cos\left(\frac{n\pi}{\alpha}\theta\right)\frac{\partial J_{\frac{n\pi}{\alpha}}}{\partial r}(k_0R)\,d\theta=\mathrm{B}_{pn}^{S} \qquad (3.33)$$

$$\int_0^{\alpha}\cos\left(\frac{p\pi}{\alpha}\theta\right)\left[ik_q\cos\left(\frac{q\pi}{d}y\right)\cos\theta+\frac{q\pi}{d}\sin\left(\frac{q\pi}{d}y\right)\sin\theta\right]e^{-ik_q x}d\theta=\mathrm{C}_{pq}^{S}$$

In these expressions, the superscripts D and S denote the displacement and stress respectively. Now the system of equations (3.29) and (3.30) can be represented by

$$\begin{bmatrix}\mathrm{A}_{pm}^{D} & \mathrm{B}_{pn}^{D}\\ \mathrm{A}_{pm}^{S} & \mathrm{B}_{pn}^{S}\end{bmatrix}\begin{bmatrix}A_m\\ B_n\end{bmatrix}=\begin{bmatrix}\mathrm{C}_{pq}^{D}\\ \mathrm{C}_{pq}^{S}\end{bmatrix}C_q \qquad (3.34)$$

Notice that the indices m and n are dummy indices which imply the summation over the ranges M and N ($m=0,1,2...,M \quad ; \quad n=0,1,2...,N$)

To illustrate the global matrix representation of the system of equations, it would be helpful to consider the following particular cases

- **Case 1**

$m=0 \quad ; \quad n=0 \quad ; \quad q=0 \quad ; \quad p=0$

For this case, the system of equations (3.34) is given by:

$$\begin{bmatrix}\mathrm{A}_{00}^{D} & \mathrm{B}_{00}^{D}\\ \mathrm{A}_{00}^{S} & \mathrm{B}_{00}^{S}\end{bmatrix}\begin{bmatrix}A_0\\ B_0\end{bmatrix}=\begin{bmatrix}\mathrm{C}_{00}^{D}\\ \mathrm{C}_{00}^{S}\end{bmatrix}C_0 \qquad (3.35)$$

(3.35) represents two equations with two unknowns.

- **Case 2**

$m=0,1,2 \quad ; \quad n=0,1,2 \quad ; \quad q=0 \quad ; \quad p=0,1,2$

The system of equations (3.34) is then given by

$$\begin{bmatrix} A^D_{00} & A^D_{01} & A^D_{02} & B^D_{00} & B^D_{01} & B^D_{02} \\ A^D_{10} & A^D_{11} & A^D_{12} & B^D_{10} & B^D_{11} & B^D_{12} \\ A^D_{20} & A^D_{21} & A^D_{22} & B^D_{20} & B^D_{21} & B^D_{22} \\ A^S_{00} & A^S_{01} & A^S_{02} & B^S_{00} & B^S_{01} & B^S_{02} \\ A^S_{10} & A^S_{11} & A^S_{12} & B^S_{10} & B^S_{11} & B^S_{12} \\ A^S_{20} & A^S_{21} & A^S_{22} & B^S_{20} & B^S_{21} & B^S_{22} \end{bmatrix} \begin{bmatrix} A_0 \\ A_1 \\ A_2 \\ B_0 \\ B_1 \\ B_2 \end{bmatrix} = \begin{bmatrix} C^D_{00} \\ C^D_{10} \\ C^D_{20} \\ C^S_{00} \\ C^S_{10} \\ C^S_{20} \end{bmatrix} C_0 \tag{3.36}$$

(3.36) represents six equations with six unknowns.

- **Case 3**

$m = 0,1,2,...,M \quad ; \quad n = 0,1,2,...,N \quad ; \quad q = 0 \quad ; \quad p = 0,1,2,...,P$

For this general case the system of equations (3.34) is then given by

$$\begin{bmatrix} A^D_{00} & A^D_{01} & A^D_{02} & \rightarrow & A^D_{0M} & B^D_{00} & B^D_{01} & B^D_{02} & \rightarrow & B^D_{0N} \\ A^D_{10} & A^D_{11} & A^D_{12} & \rightarrow & A^D_{1M} & B^D_{10} & B^D_{11} & B^D_{12} & \rightarrow & B^D_{1N} \\ A^D_{20} & A^D_{21} & A^D_{22} & \rightarrow & A^D_{2M} & B^D_{20} & B^D_{21} & B^D_{22} & \rightarrow & B^D_{2N} \\ \downarrow & \downarrow & \downarrow & \downarrow & \downarrow & \downarrow & \downarrow & \downarrow & \downarrow & \downarrow \\ A^D_{P0} & A^D_{P1} & A^D_{P2} & \rightarrow & A^D_{PM} & B^D_{P0} & B^D_{P1} & B^D_{P2} & \rightarrow & B^D_{PN} \\ A^S_{00} & A^S_{01} & A^S_{02} & \rightarrow & A^S_{0M} & B^S_{00} & B^S_{01} & B^S_{02} & \rightarrow & B^S_{0N} \\ A^S_{10} & A^S_{11} & A^S_{12} & \rightarrow & A^S_{1M} & B^S_{10} & B^S_{11} & B^S_{12} & \rightarrow & B^S_{1N} \\ A^S_{20} & A^S_{21} & A^S_{22} & \rightarrow & A^S_{2M} & B^S_{20} & B^S_{21} & B^S_{22} & \rightarrow & B^S_{2N} \\ \downarrow & \downarrow & \downarrow & \downarrow & \downarrow & \downarrow & \downarrow & \downarrow & \downarrow & \downarrow \\ A^S_{P0} & A^S_{P1} & A^S_{P2} & \rightarrow & A^S_{PM} & B^S_{PM} & B^S_{P1} & B^S_{P2} & \rightarrow\downarrow & B^S_{PN} \end{bmatrix} \begin{bmatrix} A_0 \\ A_1 \\ A_2 \\ \downarrow \\ A_M \\ B_0 \\ B_1 \\ B_2 \\ \downarrow \\ B_N \end{bmatrix} = \begin{bmatrix} C^D_{00} \\ C^D_{10} \\ C^D_{20} \\ \downarrow \\ C^D_{P0} \\ C^S_{00} \\ C^S_{10} \\ C^S_{20} \\ \downarrow \\ C^S_{P0} \end{bmatrix} C_0 \tag{3.37}$$

The solution of equations (3.29) and (3.30) is obtained by choosing $N = M$ and setting $p = 0,...,M$. The resulting algebraic system of equations (3.37), of size $(M+1)+(N+1)$, is subsequently solved to determine the amplitudes A_m and B_n.

3.4. Energy balance

Based on the principle of conservation of energy which states that,

$$E_q^{inc} = \sum_{m=0}^{M} E_m^{ref} \tag{3.38}$$

Where E_q^{inc} is the energy flux carried by the specified incident mode while E_m^{ref} represents the energy flux of m^{th} reflected mode through the cross section of the plate.

E_q^{inc} and E_m^{ref} are defined below [Abduljabbar et al, 1983].

$$E_m^{ref} = \begin{cases} \dfrac{d}{4}\mu\omega k_m |A_m|^2, & m \neq 0 \\ \dfrac{d}{2}\mu\omega k_m |A_m|^2, & m = 0 \end{cases} \tag{3.39}$$

$$E_q^{inc} = \begin{cases} \dfrac{d}{4}\mu\omega k_q |C_q|^2, & q \neq 0 \\ \dfrac{d}{2}\mu\omega k_q |C_q|^2, & q = 0 \end{cases} \tag{3.40}$$

In equation (3.39), $|A_m|$ represents the absolute value of the amplitude of the mode transporting the energy flux.

The approach taken in this work involves a wave function expansion and uses of truncated Fourier series in expressing the solution in the regions of the plate. To evaluate the accuracy of the technique, the error involved in the analysis can be estimated by the derivation from equation (3.38). This leads to the expression:

$$\varepsilon = \frac{\left(E_q^{inc} - \sum_{m=0}^{M} E_m^{ref} \right)}{E_q^{inc}} \tag{3.41}$$

Where ε denotes the relative error in the computational procedure. The value of M is increased iteratively until the relative energy error ε, shown in equation (3.41), satisfies a desired tolerance.

It will be convenient to introduce the symbol R_{mq} to denote the ratio of the elastic energy flux contained in reflected mode m to the elastic energy flux supplied by incident mode q

$$R_{mq} = \frac{E_m^{ref}}{E_q^{inc}} \tag{3.42}$$

Substituting equation (3.42) into equation (3.41) results in the following expression for the relative error in the elastic energy flux,

$$\varepsilon = 1 - \sum_{m=0}^{M} R_{mq} \tag{3.43}$$

In this work, the series solutions (3.18) and (3.21) are considered to be convergent when the corresponding relative error ε does not exceed 1×10^{-5}.

3.5. Plate with vertical edge (beveled angle = 90°)

The limiting case for $\alpha = \frac{\pi}{2}$, as shown in Figure 3.6, corresponds physically to a waveguide of a semi-infinite plate with a vertical edge.

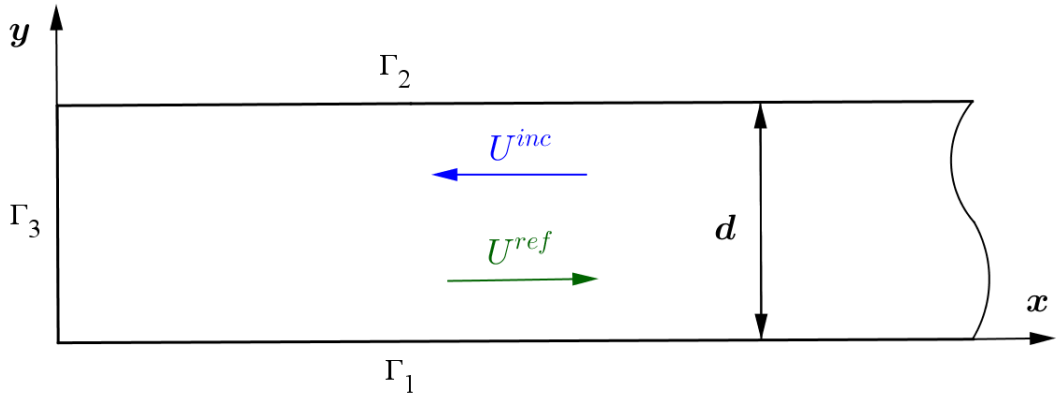

Figure 3.6: Plate structure with normal free end

In this special case, the stress-free boundary conditions on Γ_3 is expressed in rectangular coordinates as:

$$\sigma_{xz}^{I} = 0, \quad x = 0 \tag{3.44}$$

Substitution of the stress expression given in equation (3.23) into equation (3.44) above, results in the following relationship between incident and reflected modes,

$$\sum_{m=0}^{M} A_m \left[ik_m \cos\left(\frac{m\pi}{d} y\right)\right] = -C_q \left[-ik_q \cos\left(\frac{q\pi}{d} y\right)\right] \tag{3.45}$$

Using the orthogonality of modes, equation (3.45), has the following analytical solution for the amplitude of the reflected modes,

$$\begin{aligned} &A_q = C_q \\ &A_m = 0 \quad m = 0,1,2,\ldots,M \qquad m \neq q \end{aligned} \tag{3.46}$$

The above result is obtained by:

a) Multiplying both sides of equation (3.45) by $\cos\left(\frac{n\pi}{d} y\right)$

b) Integrating the resulting equation over y from 0 to d

c) Making use of the orthogonality of the trigonometric functions over Γ_3

d) Taking the corresponding incident q^{th} mode ($q = 0,1$)

Equation (3.46) manifests the well-known fact that an incident mode reflects from the vertical free end of waveguide are totally reflected back.

The same solution to the vertical free end can be found by dividing the domain into two regions as shown in Figure 3.7.

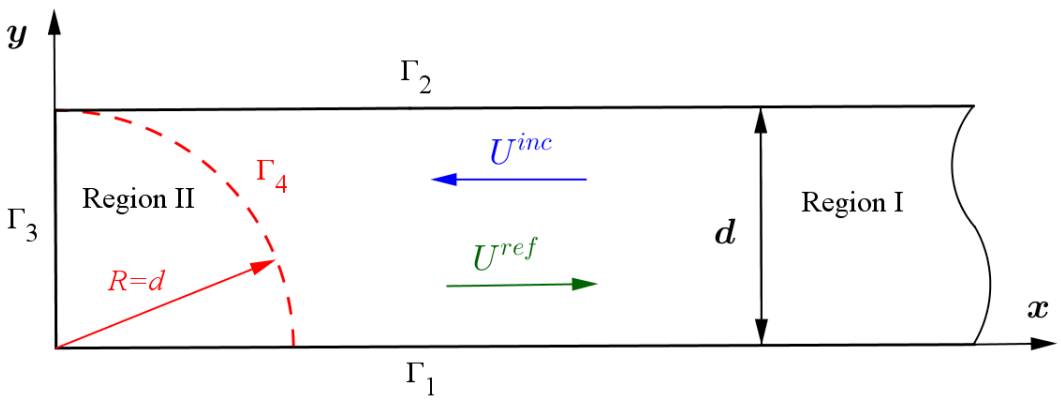

Figure 3.7: Partitioned wedge-plate regions and common fictitious boundary.

Substitution of equation (3.46) into the continuity condition at the artificial interface described in equations (3.6) and (3.7) yields

$$C_q \cos\left(\frac{q\pi}{d} y\right)\left(e^{-ik_q x} + e^{ik_q x}\right) = \sum_{n=0}^{N} B_n \cos(2n\theta)\, J_{2n}(k_0 R) \tag{3.47}$$

At the interface $x = R\cos\theta$ and for the zeroth incident mode $q = 0$, equation (3.47) reduces to:

$$C_0 2\cos(k_0 R\cos\theta) = B_0 J_0(k_0 R) + \sum_{n=1}^{N} B_n \cos(2n\theta)\, J_{2n}(k_0 R) \tag{3.48}$$

The well-known *Jacobi-Anger expansion* is:

$$\cos(z\cos\theta) = J_0(z) + 2\sum_{n=1}^{\infty}(-1)^n J_{2n}(z)\cos(2n\theta) \tag{3.49}$$

With z replaced by $k_0 R$, equation (3.49) becomes:

$$\cos(k_0 R\cos\theta) = J_0(k_0 R) + 2\sum_{n=1}^{\infty}(-1)^n J_{2n}(k_0 R)\cos(2n\theta) \tag{3.50}$$

Comparing equations (3.48) and (3.50), while setting $C_0 = 1$, the unknown coefficients can be found.

$$\begin{aligned} B_0 &= 2 \\ B_n &= 4(-1)^n \quad n = 1, 2, ..., N \end{aligned} \tag{3.51}$$

The results B_n in equation (3.51) are used to verify the accuracy of truncated series solution proposed above.

3.6. Summary

An analytical approach is presented for the propagation of SH waves in a beveled free end plate. A region matching technique is applied to derive a series solution. Appropriate wave functions are employed to describe the displacement field of the SH wave. The enforcement of the continuity of displacements and stresses at the fictitious common boundary leads to the determination of the unknown coefficients. Finally, the particular case of a plate with vertical edge (beveled angle = 90°) was used to determine a simple analytical results that will be used in a limiting case sense, to test the numerical results obtained in the next chapter.

Chapter 4

Numerical results and discussion

Chapter 4

Numerical results and discussion

4.1. Introduction

In this chapter the numerical results of Horizontally Shear wave propagation in a beveled free end plate are presented in terms of the ratio between the energy of the m^{th} reflected mode and the energy of the q^{th} incident mode. Two cases are considered; the zeroth (symmetric) and the first (antisymmetric) modes of incident waves. Beveled angles ranging from 20° to 90° with 0.1° increment and normalized frequencies ranging from 0 to 5.5 are considered. Selected beveled angles are reported here, namely 30°, 45° and 60° for the whole range of the normalized frequency. Also, three selected frequencies are considered, namely 1.5, 3.5 and 5.5, for the variation of the beveled angle from 0° to 90°.The energy ratios are plotted as function of the beveled angles and normalized frequencies.

4.2. Non-dimensional frequency and wave number

For this kind of studies, it is very convenient to define the non-dimensional frequency (normalized frequency) and the non-dimensional wave number. A non-dimensional form of Equations (3.19) and (3.20) is adopted and used in reporting numerical results found in this thesis. Rewriting Equations (3.19) as

$$k_m = \sqrt{\frac{\omega^2}{c_s^2} - \frac{m^2\pi^2}{d^2}} = \frac{\pi}{d}\sqrt{\left(\frac{\omega^2 d^2}{\pi^2 c_s^2}\right) - m^2} \tag{4.1}$$

or

$$\frac{k_m d}{\pi} = \sqrt{\left(\frac{\omega^2 d^2}{\pi^2 c_s^2}\right) - m^2} \tag{4.2}$$

where

$K_m = \frac{k_m d}{\pi}$ is The non-dimensional wave number and $\Omega = \frac{\omega d}{\pi c_s}$ is the non-dimensional frequency. With this notation, Equations (3.19) and (3.20) become:

$$K_m = \sqrt{\Omega^2 - m^2} \tag{4.4}$$

$$K_q = \sqrt{\Omega^2 - q^2} \tag{4.5}$$

According to this definition, $\Omega = \frac{\omega d}{\pi c_s} = \frac{kd}{\pi} = \frac{2d}{\lambda}$, (where $\lambda = \frac{2\pi}{k}$ is the wavelength),

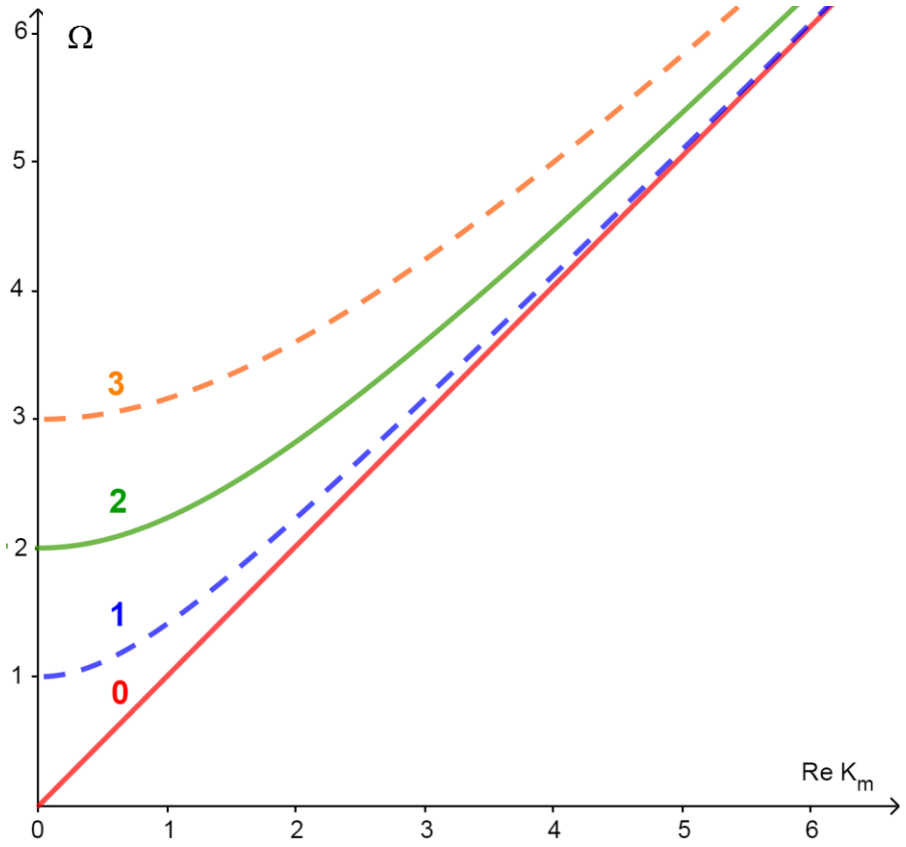

Figure 4.1: Frequency spectrum for SH waves in a plate. Solid line are the symmetric modes, dashed lines are the antisymmetric modes

Examination of Equations (4.4) and (4.5), show that for $m = 0$ ($q = 0$) gives that $K_{m,q} = \Omega$, or in dimensional form, $\omega = k\, c_s$. Thus it is seen that the zeroth-mode is non-dispersive, whereas all other modes propagate dispersively (Figure 4.1).

For $\Omega > m,q$, $K_{m,q}$ is real and the spectrum consists of a family of hyperbolas $(m,q=1,2,3,...)$. At $K_{m,q}=0$, $\Omega = m,q$ which represents the cutoff frequencies for the various modes. For $\Omega < m,q$, $K_{m,q}$ is imaginary which correspond to a non-propagating waves. Once again, in Figure 4.1, the solid lines correspond to the symmetric modes $(m,q=0,2,)$, the dashed lines are the antisymmetric modes $(m,q=1,3)$.

If the non-dimensional frequency Ω is small which corresponds to the case of a low frequency, it means that the dimension of the thickness of the plate is small compared to the wavelength and conversely.

4.3. Energy variation with normalized frequency at selected beveled angles

When a single known propagating incident mode impinges on the beveled end of a semi-infinite plate, it induces a collection of both propagating and non-propagating reflected modes. The elastic energy of the reflected propagating modes is reported in this section for both SH_0 and SH_1 known incident modes, for a wide range of corresponding beveled angles and frequencies. The energy is reported as the ratio between the energy of the m^{th} reflected mode and the energy of the q^{th} incident mode.

The proper number of terms in the series solution given in Equations (3.18) and (3.21), M (in region I) and N (in region II), are chosen by numerically testing for their convergence. Based on a sequence of numerical experiments, the maximum convergence is achieved at N=18 wave function modes in the region of the beveled end, and M=18 wave function modes in the plate region. In this work the largest non-dimensional frequency was set to 5.5 and the error tolerance ε, defined in Equation (3.44), does not exceed 1×10^{-5}.

4.3.1. Energy variation for the SH_0 incident mode

Figure 4.2 through Figure 4.4 show the R_{m0} distribution due to SH_0 incident mode. The variations of R_{m0} versus Ω, due to the SH_0 incident mode, which correspond to $\alpha = 30^{\circ}$, 45°, and 60°, respectively are displayed in these Figures.

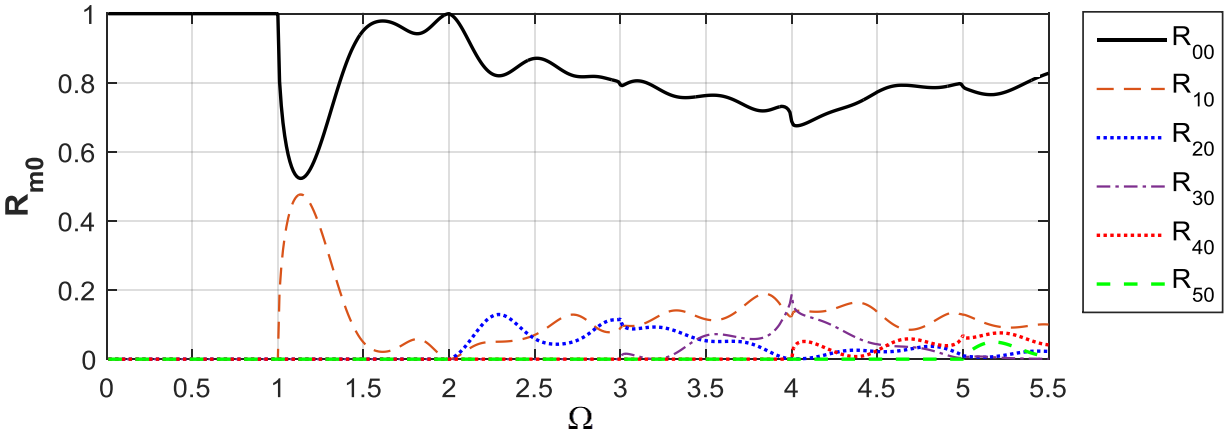

Figure 4.2: R_{m0} versus normalized frequency for selected beveled edge $\alpha = 30°$

4.3.1.1 Mode dominance of SH_0

When the beveled angle is 30° (Figure 4.2) or 45° (Figure 4.3) R_{00} is strictly larger than R_{m0} $(m \neq 0)$ over the entire frequency range. For $\alpha = 30^{\circ}$ (Figure 4.2), the minimum value of R_{00} is 0.523 which is attained when $\Omega = 1.13$.

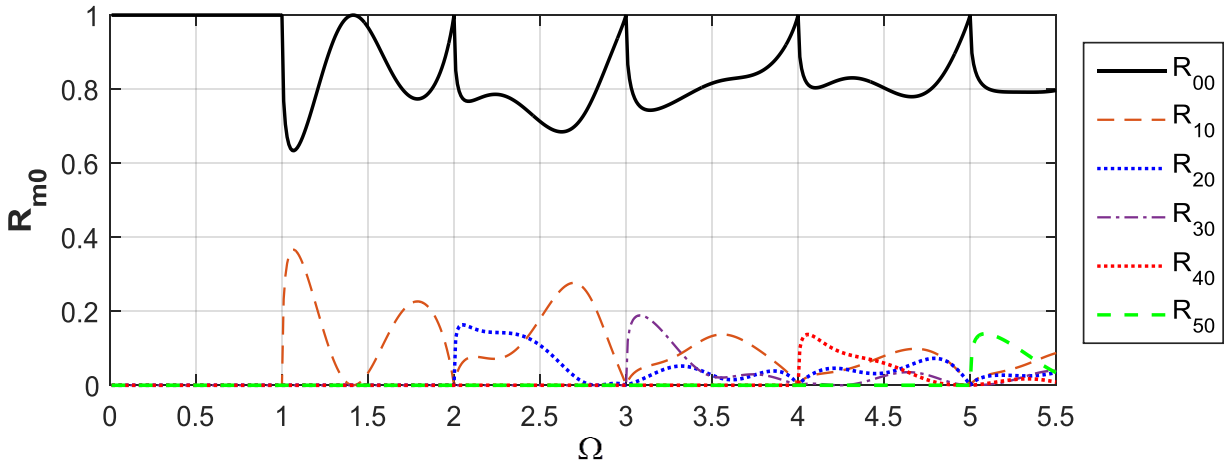

Figure 4.3: R_{m0} versus normalized frequency for selected beveled edge $\alpha = 45°$

While when $\alpha = 45°$ (Figure 4.3) the minimum value of R_{00} is 0.634 and is attained when $\Omega = 1.07$. For the $\alpha = 60°$ (Figure 4.4) R_{00} loses its dominance and vanishes at the following frequencies: 1.155, 2.309, 3.464, and 4.619. These values are illustrated in table 4.1.

Table 4.1. Calculated results of R_{mo} for particular frequencies and beveled edge $\alpha = 60°$

Ω	α	R_{00}	R_{10}	R_{20}	R_{30}	R_{40}	R_{50}	Error
1.155	60°	2.06E-13	1					1.00E-08
2.309	60°	1.03E-13	1.93E-07	1				1.00E-08
3.464	60°	2.29E-16	5.76E-09	1.24E-08	0.999971			1.00E-08
4.619	60°	2.80E-15	1.94E-08	2.28E-08	3.99E-08	1		1.00E-08

4.3.1.2 Total reflection of SH_0

Total reflection of SH_0 is reached when $R_{00} = 1$. This occurs at certain beveled angle and frequency values. At beveled angle $\alpha = 30°$ and 60° the total reflection occurs when $\Omega = 2$ (which is also a cut-off frequency). When $\alpha = 45°$ $R_{00} = 1$ at all cutoff frequencies (1,2,3,4,5) and when $\Omega = 1.414$.

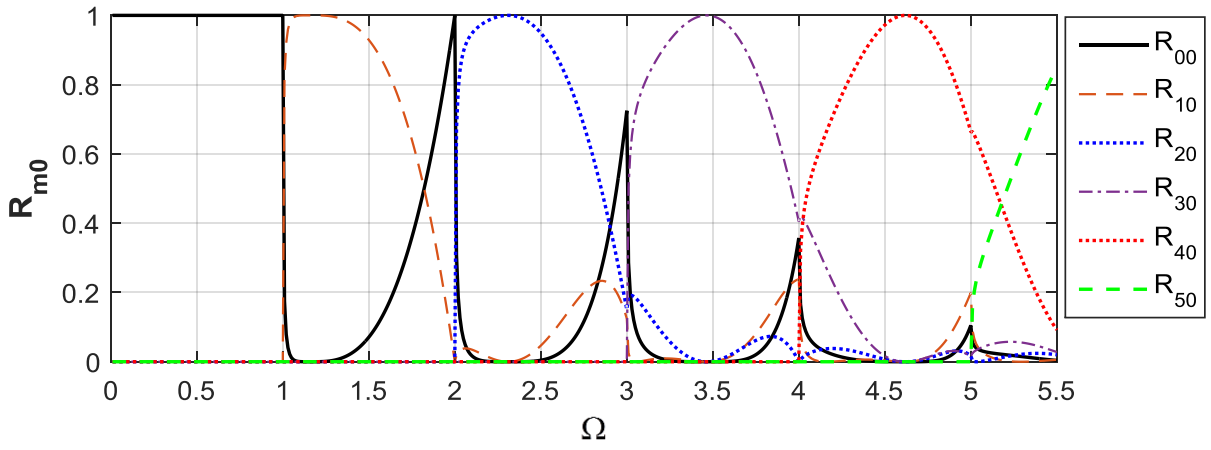

Figure 4.4: R_{m0} versus normalized frequency for selected beveled edge $\alpha = 60°$

4.3.1.3 Mode conversion of SH_0

As shown in table 4.1, when α=60° and for Ω=1.155, SH_1 is the only reflected mode, similarly when $\Omega = 2.309$, 3.464 and 4.619 the SH_2, SH_3 and SH_4 are the corresponding total reflected modes, respectively. (Figure 4.4).

4.3.2. Energy variation for the SH_1 incident mode

Figure 4.5 through Figure 4.7 show the R_{m1} distribution due to SH_1 incident mode. The variations of R_{m1} versus Ω, due to the SH_1 incident mode, which correspond to $\alpha = 30^{\circ}$, 45°, and 60°, respectively are displayed in these Figures.

4.3.2.1 Mode dominance of SH_1

Unlike the dominance of the SH_0 mode over the entire frequency range, the SH_1 mode shows partial dominance as shown in Figures 4.5 and 4.6.

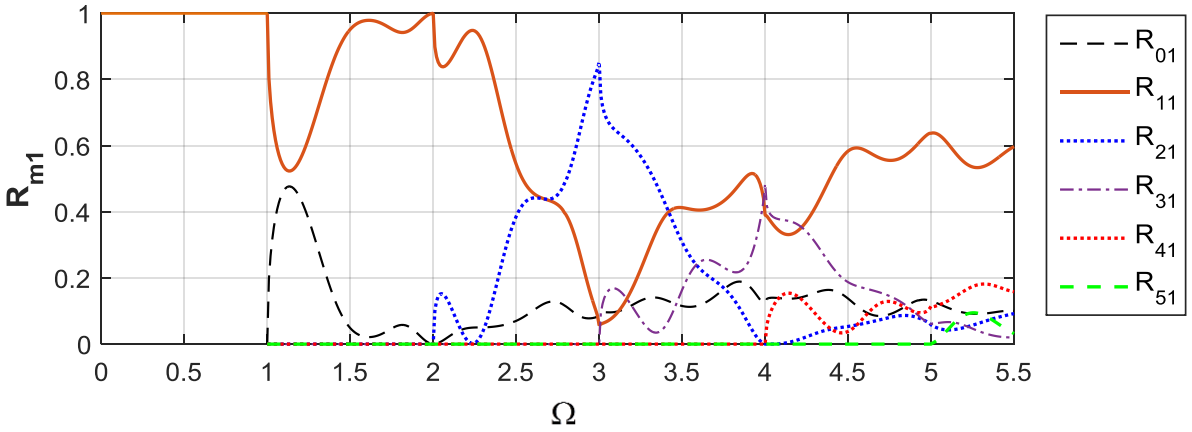

Figure 4.5: R_{m1} versus normalized frequency for selected beveled edge $\alpha = 30°$

4.2.2.2 Total reflection of SH_1

At a beveled angle $\alpha = 30°$, the total reflection is attained when $\Omega = 1$ and $\Omega = 2$. For the case of $\alpha = 45°$, total reflection of the incident SH_1 mode is obtained when $\Omega = 1$, $\Omega = 1.412$, and $\Omega = 2$. At the beveled angle $\alpha = 60^{\circ}$, the total reflection is attained when $\Omega = 1$, $\Omega = 2$, and $\Omega = 2.309$.

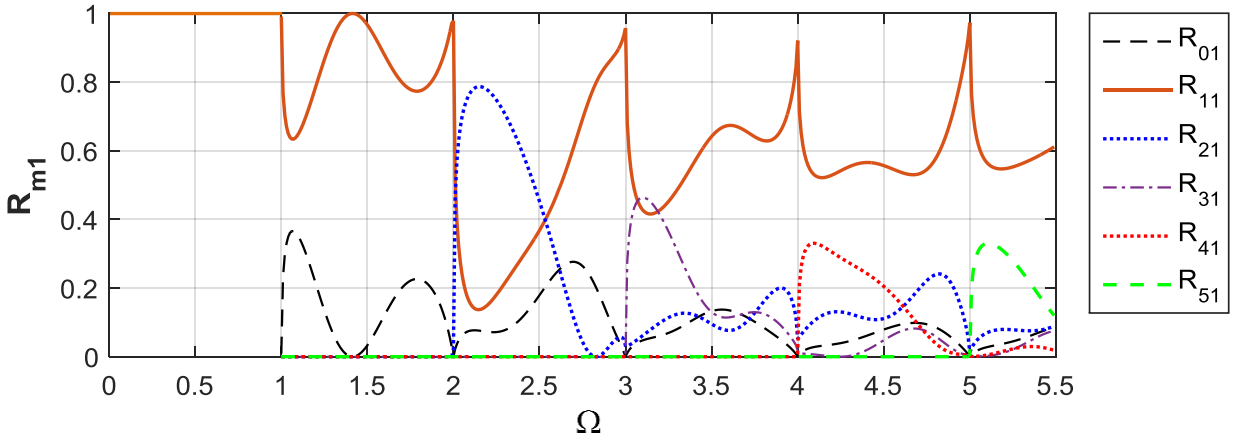

Figure 4.6: R_{m1} versus normalized frequency for selected beveled edge $\alpha = 45°$

4.3.2.3 Mode conversion of SH_1

Table 4.2 demonstrates when $\alpha = 60^{\circ}$ and for $\Omega = 1.155$, 3.055, 4.163, and 5.292, SH_1 disappears ($R_{11} = 0$) giving way to other modes to carry the reflected energy.

Table 4.2. Calculated results of R_{m1} for particular frequencies and beveled edge $\alpha = 60°$

Ω	α	R_{01}	R_{11}	R_{21}	R_{31}	R_{41}	R_{51}	Error
1.155	60°	1	2.06E-13					1.00E-08
2.309	60°	1.93E-07	1	1.93E-07				1.00E-08
3.055	60°	8.00E-09	8.07E-16	0.799976	0.200024			1.00E-08
4.163	60°	6.33E-08	1.49E-13	1.13E-07	0.71398	0.28602		1.00E-08
5.292	60°	6.61E-08	2.94E-13	1.00E-07	3.28E-07	0.667146	0.332853	1.00E-08

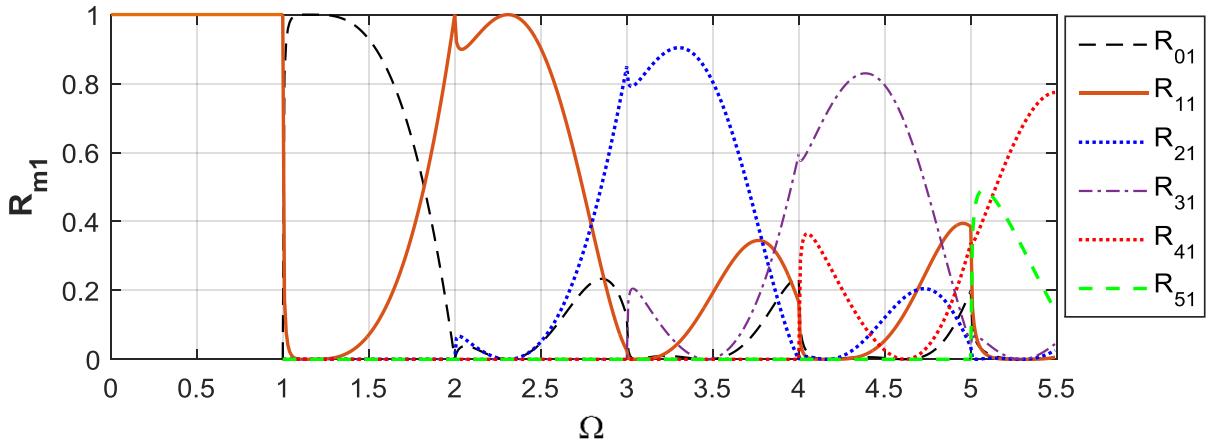

Figure 4.7: R_{m1} versus normalized frequency for selected beveled edge $\alpha = 60°$

The abrupt variations at the cutoff frequencies in Figures 4.3, 4.4, 4.6 and 4.7 are due to the inception of new propagating modes, which cause a sudden change in the distribution of energy in the spectra of the reflected and transmitted waves. Remarkably, the variation in the energy ratios is more abrupt when the beveled angle is increased (see Figures 4.3 and 4.6).

4.4.Energy variation with beveled angles and selected frequencies

In subsection 4.2, the variation of the normalized frequency Ω versus three beveled angles, namely $\alpha = 30°, \alpha = 45°$ and $\alpha = 60°$ was reported. However, in this subsection, the variation of the beveled angle $20^{\circ} \le \alpha \le 90°$ for selected frequencies $\Omega = 1.5$, 3.5, and 5.5, is investigated to determine the interaction of SH waves with a range of beveled angles.

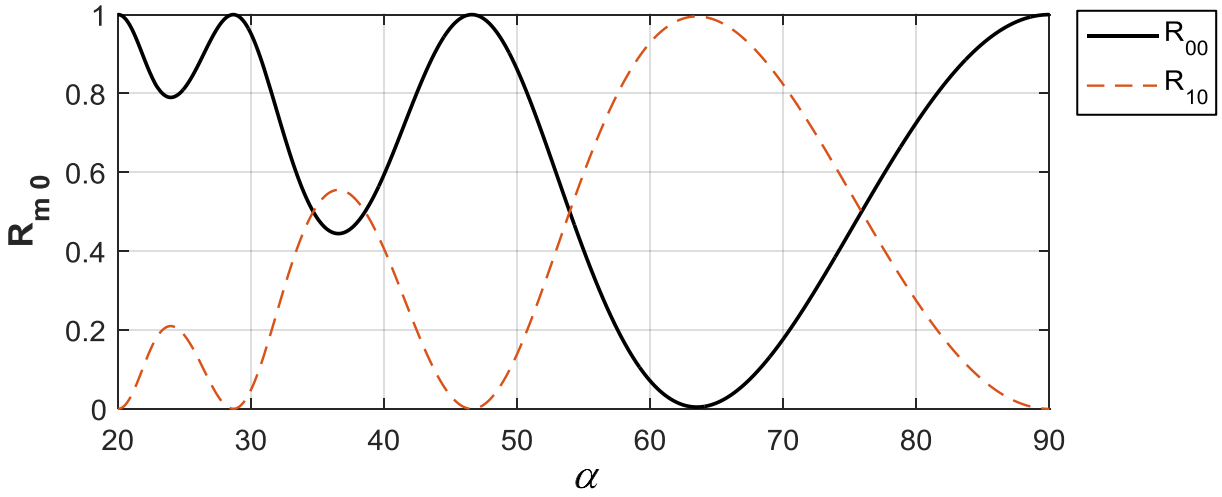

Figure 4.8: R_{m0} versus beveled edge angle for normalized frequency $\Omega = 1.5$

In Figures 4.8, 4.9 and 4.10, R_{m0} versus beveled edge angle at three selected normalized frequencies, namely 1.5, 3.5, and 5.5, is reported. These frequencies are selected to be halfway between the cutoff frequencies.

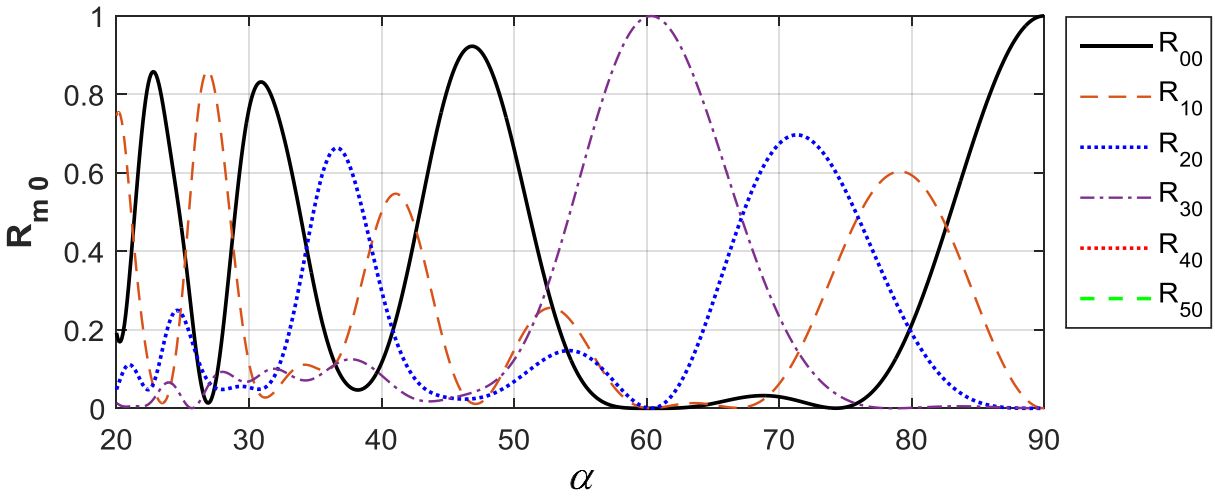

Figure 4.9: R_{m0} versus beveled edge angle for normalized frequency $\Omega = 3.5$

In Figure 4.8, SH_0 gradually decreases until it diminishes, $R_{00} = 0$, after which it increases and reaches total reflection, $R_{00} = 1$, when $\alpha = 20.019°$, $28.67°$ and $46.60°$ (Table 4.3).

Table 4.3. Calculated results of R_{m0} for particular angles and normalized frequency $\Omega = 1.5$

Ω	α	R_{00}	R_{10}	R_{20}	R_{30}	R_{40}	R_{50}	Error
1.5	20.019	1.00E+00	1.23E-13					1.00E-08
1.5	28.6691	1.00E+00	1.24E-14					1.00E-08
1.5	46.597	1.00E+00	1.21E-11					1.00E-08
1.5	63.51	4.53E-03	9.95E-01					1.00E-08

Figures 4.9 and 4.10 show the region where SH_0 is very small compared to the other propagating modes. This region is centered around $\alpha = 63°$.

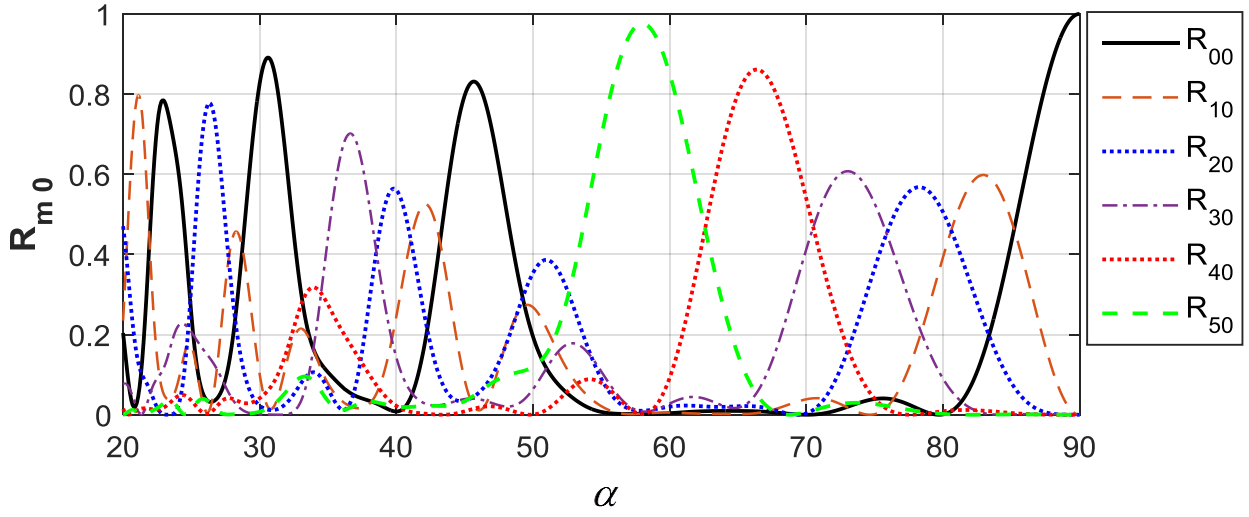

Figure 4.10: R_{m0} *versus beveled edge angle for normalized frequency* $\Omega = 5.5$

Similarly, in Figures 4.11, 4.12 and 4.13, R_{m1} versus beveled edge angle at the three selected normalized frequencies is displayed.

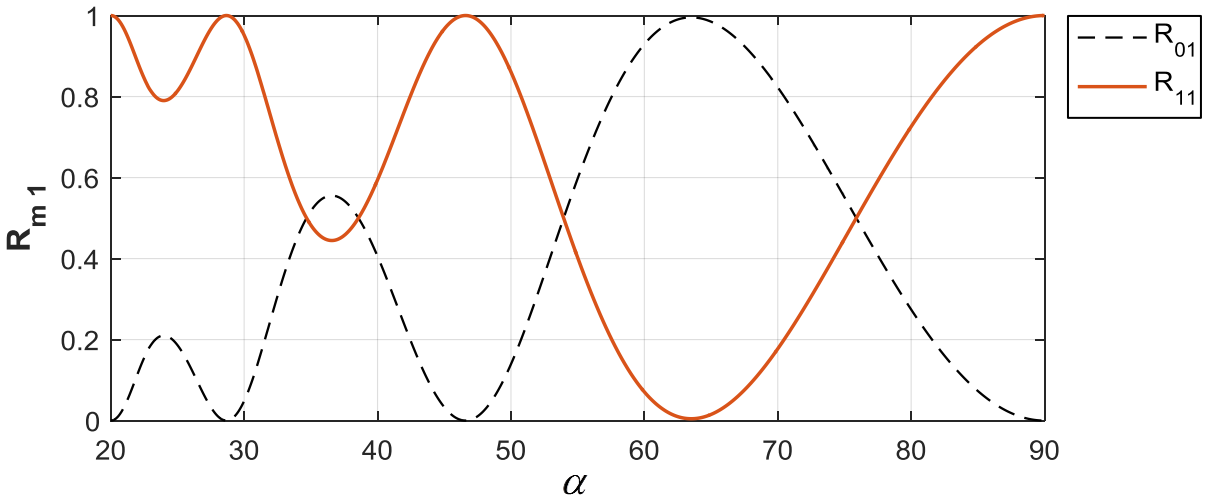

Figure 4.11: R_{m1} *versus beveled edge angle for normalized frequency* $\Omega = 1.5$

SH_1 gradually decreases until it diminishes, $R_{00} = 0$, after which it increases and reaches total reflection, $R_{11} = 1$, when $\Omega = 1.5$, $\alpha = 28.67°$, and 46.60° (Table 4.4).

Table 4.4. Calculated results of R_{m1} for particular angles and normalized frequency $\Omega = 1.5$

Ω	α	R_{01}	R_{11}	R_{21}	R_{31}	R_{41}	R_{51}	Error
1,5	28,67	1,29E-09	1					1,00E-08
1,5	46,6	3,51E-08	1					1,00E-08
1,5	63,51	0,995468909	0,004531					1,00E-08

The region of vanishing R_{11} is not as extreme as in the case of R_{00}.

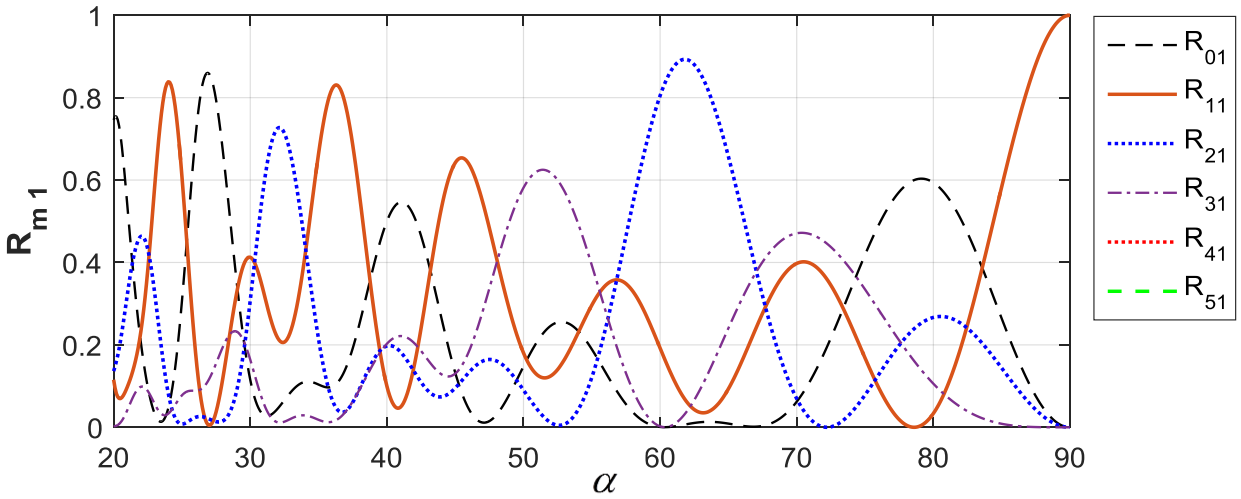

Figure 4.12: R_{m1} versus beveled edge angle for normalized frequency $\Omega = 3.5$

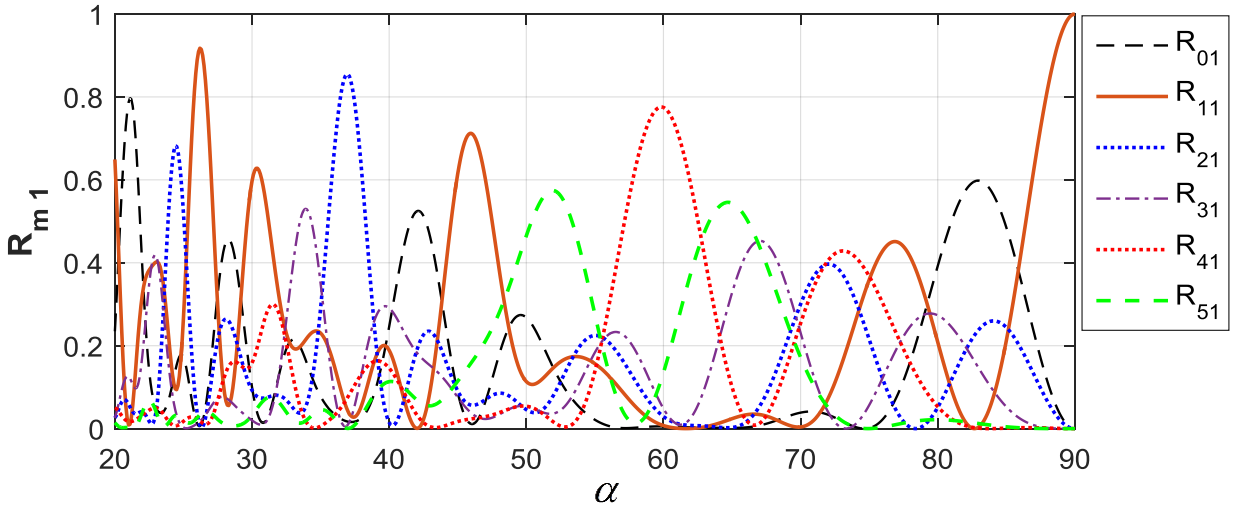

Figure 4.13: R_{m1} versus beveled edge angle for normalized frequency $\Omega = 5.5$

4.5. Comparison with other approaches

Facing recent approaches, this study deals with wave function expansion for the beveled end instead of a spatial discretization. As illustrated in (Table 4.5), this technique offers the advantages of allowing stable analysis of a vast selection of beveled angles, satisfaction of the boundary conditions, accuracy of the results and fast analysis time.

Table 4.5. Comparison with other approaches

	[Chancellier et al, 2002]	**[Chancellier et al, 2005]**	**[Mofakhami and Boller, 2008]**	**[Nakamura et al, 2012]**	**[Ahmad and Gabbert, 2012]**	**[Mohammedi et al, 2019]**
Wave type	Studied guided Lamb waves propagation	Studied guided Lamb waves propagation	Studied guided Lamb waves propagation	Studied SH waves	Studied guided Lamb waves propagation	Studied the propagation of SH waves in a waveguide
Approximation method	Used collocation methods and confirmed their results using finite elements method with 45 wave function modes.	Used a collocation method on the beveled free end to determine the Lamb wave amplitudes. N=800 collection points and M=45 wave function modes.	Used time domain Finite element method	Used time domain Finite element method	Used time domain semi-analytical finite element method	Used frequency domain analytical wave functions method, to determine the SH wave amplitudes with N=18 wave function modes.
Continuity condition at the boundary	Enforced Continuity conditions at the interface nodes of the finite elements.	Approximated a no tractions boundary condition at the beveled end.	Used artificial internal boundary to model the semi-infinite section.		Enforced Continuity conditions at the interface nodes of the finite elements.	Enforced continuity of displacements and tractions at an artificial internal boundary,
Materials	Used specific materials – stainless steel plates	Used specific materials – stainless steel plates	Used specific materials – Aluminum.	Used specific materials – Aluminum plates.	Used specific materials – Aluminum plates.	Used non-dimensional quantities that apply to wide range of materials.
Accuracy	Solutions converge for angle values between 70° and 90°. For smaller angles, the precision is less.	Achieved an accuracy of 1%.	Did not report on the accuracy of their results	Did not report on the finite element results accuracy	Did not report on the semi-analytical finite element results accuracy.	Achieved an accuracy of 0.001%

	[Chancellier et al, 2002]	[Chancellier et al, 2005]	[Mofakhami and Boller, 2008]	[Nakamura et al, 2012]	[Ahmad and Gabbert, 2012]	[Mohammedi et al, 2019]
Bevel angles	reported only inclination angles between 70° and 90° with increments of 5°	Considered beveled angles between 85° and 90°	Considered a wide range of angles from 25° and up to 90° with an increment of 5°.	Used beveled angles 60°, 85°, 90° specimen in their experimental setting and 1° inclination for numerical simulation	Report shows results for a 45° inclination angle	used bevel angles as low as 20° and up to 90° with an increment of 0.1°
Frequency Range	Considered low frequencies. The frequency reported was 3.15 MHz-mm which is equivalent to the non-dimensional frequency of about 0.4. This is considered to be in the low-frequency range.	Considered low frequencies for a specific material (stainless steel, c_T =3150 m/s). The frequency reported was between 1 to 4 MHz-mm. The equivalent no-dimensional frequency range is between 0.1 - 0.4	Considered low frequencies. The frequency reported was 400 MHz and thickness of 3 mm which is equivalent to no-dimensional frequency of about 0.2. This is considered to be in the low-frequency range	Used low frequency 0.546 MHz in a 2 mm thick plate. The equivalent no-dimensional frequency is about 0.1.	Considered low frequencies. The frequency reported was 2 and 5 MHz-mm. The equivalent to non-dimensional frequency range 0.2 - 0.5. This is considered to be in the low-frequency range.	This study reports non-dimensional frequency between 0 - 5.0, which places this work in the low to high-frequency range
Discretization	Meshing is needed for each beveled angle	Used collocation method	Used Finite elements to discretize the domains	Used spatial discretization method	Meshing is needed for each beveled angle. This also leads to mesh-dependency of results.	This approach uses global wave functions and does not require spatial discretization.

4.6. Summary

Numerical results are presented for the propagation of SH waves in a beveled free end plate. In this study, single incident SH_0 and SH_1 modes were used, and reflected SH modes are examined. Two cases are considered; in the first, the zeroth mode (SH_0 symmetric mode) is incident on the edge at selected frequencies and in the other, the first mode (SH_1 anti-symmetric mode) is incident on the edge at the same range of frequencies. The results are presented in term of the ratio between the energy of the reflected mode and the energy of the incident mode for a wide range of beveled angles and frequencies. The validity and accuracy of the results are checked by satisfaction of the energy conservation principle.

Finally, a comparative study between different approaches mentioned in the literature shows the novelty of this work and indicates that the approach used is easy to deal with in a very wide range of angles and frequencies with great accuracy.

Chapter 5

Conclusions

Chapter 5

Conclusions

5.1. Summary of findings

In this thesis, a wave function expansion method is used to analyze the diffraction of SH waves by the beveled free end of a semi-infinite plate (waveguide). The plate with edge defect is modeled as a semi-infinite elastic plate with traction free surfaces and beveled free end. The solution of the problem uses the separability property of the Helmholtz equations, for both rectangular and cylindrical coordinates, and the continuity condition across an artificial boundary separating the two regions. This strategic selection of the regions leads to an efficient separable solution for the unknown coefficients.

In this study, only two single incident modes SH_0 and SH_1 (monochromatic) were used, and a range of frequencies was considered. Continuity conditions at the common boundary between the two regions combined with the orthogonal functions expansion led to a set of algebraic equations to derive the amplitude of the reflected waves.

The numerical solution of these algebraic equations is determined for a wide range of frequencies and bevel angles with a relative energy error that does not exceed 1×10^{-5}. For the limiting case, the computed results for a plate with vertical edge (beveled angle = 90°) are in good agreement with those from the exact series solution of a single vertical edge plate. These evidences have reinforced the validity of the whole framework of present formulations. This study has also shown the existence of critical bevel angles where an incident mode is either “totally” reflected or “totally” absorbed at a specific incident frequency.

In contrast to recent approaches to beveled waveguides, [Chancellier et al, 2002], [Chancellier et al, 2005], [Mofakhami and Boller, 2008], [Nakamura et al,

2012], [Ahmad and Gabbert, 2012], this work did not spatially discretize the beveled end of the waveguide. Moreover, a richer family of orthogonal wave function expansion for the beveled end is used, and consequently, the particular class of bases functions with compact supports, such as those used in SAFE or collocation approaches, has been avoided. The wave function expansion comes with the advantages of allowing the stable analysis of a wider range of beveled angles, the exact satisfaction of plate surfaces boundary conditions, high accuracy for near and far fields responses, and fast analysis turnaround time.

Also, the technique used in this work demonstrated the ability to handle low to high-frequency excitation (the largest non-dimensional frequency was set to 5.5 and an extremely tight error tolerance less than 0.001 percent). Additionally, the existence of total mode conversion and total mode reflection for some non-dimensional frequencies was demonstrated. Likewise there are some critical beveled angles in which the incident mode (symmetric or anti-symmetric) is totally reflected in an inversely manner. Particularly, an incident SH_0 mode reflected into an SH_1 mode and conversely. Results at angles as low as 20^o and nondimensional frequencies as high as 5.0 have been reported, where such results are not available in the literature.

Consequently, these results illustrate the interaction of guided waves with edge defects and demonstrate a simple way to calculate reflecting coefficients. Such results can lead to the development of novel applications of guided waves to defect sizing instead of simple detection. The analytical methods presented in this thesis are very promising tools for further NDT applications, since they are much faster than classical finite element models, so they can serve as a model for numerical methods, in particular for those at much higher frequencies. Also, the adopted approach resolves some numerical instabilities that appear in other approaches available in the literature.

5.2. Recommendation for future work

Future enhancement of this work may include investigation of SH wave excitation in plates with irregular geometry resembling natural fracture lines. The study also needs to be extended to the case of plates with constrained boundary conditions.

It will be important to apply the region-matching technique to the modeling of SH wave diffraction by cracks present in a multilayer plate made of anisotropic materials. These extensions of the model allow considering many applications in the nondestructive control, particularly in the composite materials area.

Experimental validations, extended to the 3D case could be further investigated.

References

References

[Abduljabbar et al, 1983] Z. Abduljabbar, S. Datta and A. Shah, Diffraction of horizontally polarized shear waves by normal edge cracks in a plate, Journal of applied physics, 54 (1983) 461-472.

[Achenbach, 1973] J.D. Achenbach, Wave Propagation in Elastic Solids. North-Holland, Amsterdam (1973)

[Adams, 2007] D. Adams, Health monitoring of structural materials and components methods with applications, John Wiley & Sons, 2007.

[Ahmad and Gabbert, 2012] Z. Ahmad and U. Gabbert, Simulation of Lamb wave reflections at plate edges using the semi-analytical finite element method, Ultrasonics, 52 (2012) 815-820.

[Annamaria, 2016] P. Annamaria, Scattering of guided shear waves in plates with discontinuities- NDT & E International 84(67):75 -2016

[Boukabache et al, 2014] H. Boukabache; C.Escriba; J.-Y.Fourniols, Toward Smart Aerospace Structures: Design of a Piezoelectric Sensor and Its Analog Interface for Flaw Detection. Sensors 2014, 14, 20543-20561.

[Brekhovskikh, 1980] L.M. Brekhovskikh, Waves in layered media. Academic Press, 1980.

[Castaings et al, 2002] M. Castaings, E. Le Clezio and B. Hosten, Modal decomposition method for modeling the interaction of Lamb waves with cracks, The Journal of the Acoustical Society of America, 112 (2002) 2567-2582.

[Castaings, 2014] M. Castaings, SH ultrasonic guided waves for the evaluation of interfacial adhesion. Ultrasonics 2014,

[Cauchy, 1822] A.L. Cauchy, Sur les équations qui experiment les conditions d'équilibre ou les lois du movement intérieur d'un corps solide, élastique ou non élastique. Ex. de Math. 3, 160–187 (1822)-Oeuvres (2) 8, 253–277

[Chancellier et al, 2002] N. Wilkie-Chancellier, H. Duflo, A. Tinel and J. Duclos, Theoretical study of lamb wave conversion at the edge of different angles bevelled plates, in: Forum Acusticum, Seville, (2002) 17-21.

[Chancellier et al, 2004] N. Wilkie-Chancellier, H. Duflo, A. Tinel and J. Duclos, Energy balance in the conversion of a Lamb wave at a bevelled edge, Acta Acustica united with Acustica, 90 (2004) 77-84.

[Chancellier et al, 2005] N. Wilkie-Chancellier, H. Duflo, A. Tinel and J. Duclos, Numerical description of the edge mode at the beveled extremity of a plate, The Journal of the Acoustical Society of America, 117 (2005) 194-199.

[Chen et al, 2015] J.-J. Chen, G.-H. Song and X. Han, Asymmetric first order shear horizontal guided waves propagation in a tapered plate, Physics Letters A, 379 (2015) 2125-2129.

[Croxford et al, 2007] A. Croxford; P. Wilcox; B. Drinkwater; G. Konstantinidis, Strategies for guided-wave Structural HealthMonitoring. In Proceedings of the Royal Society of London A: Mathematical, Physical and Engineering Sciences;AIP Publishing: Melville, NY, USA, 2007; pp. 2961–2981.

[Deckers et al, 2014] E. Deckers, O. Atak, L. Coox, R. D'Amico, H. Devriendt, S. Jonckheere, K. Koo, B. Pluymers, D. Vandepitte, and W. Desmet, The wave based method: An overview of 15 years of research, Wave Motion, 51 (2014) 550-565.

[Demma et al, 2003] A. Demma; P. Cawley; M. Lowe, Scattering of the fundamental shear horizontal mode from steps and notches in plates. J Acoust Soc Am 2003; 113(4):1880–91.

[Demma, 2003] A. Demma, The interaction of guided waves with discontinuities in structures, thesis imperial.ac.uk, 2003

[Ditri, 1996] J.J. Ditri, Some results on the scattering of guided elastic SH waves from material and geometric waveguide discontinuities, The Journal of the Acoustical Society of America, 100 (1996) 3078-3087.

[Gao and Lopez, 2010] H. Gao, S. Ali and B. Lopez, Efficient detection of delamination in multilayered structures using ultrasonic guided wave EMATs, NDT & E International, 43 (2010) 316-322.

[Giurgiutiu, 2007] V. Giurgiutiu, Structural health monitoring: with piezoelectric wafer active sensors, Academic Press, MA, USA, (2007).

[Graff, 1991] K. F. Graff, Wave Motion in Elastic Solids. Dover Publications, 1991.

[Gunawan and Hirose, 2004] A. Gunawan; S. Hirose, Mode-exciting method for Lamb wave-scattering analysis. J Acoust Soc Am 2004; 115(3):996–1005.

[Hirao and Ogi, 1999] M. Hirao and H. Ogi, An SH-wave EMAT technique for gas pipeline inspection, NDT & E International, 32 (1999) 127-132.

[Kamal and Giurgiutiu, 2014] A. Kamal; V. Giurgiutiu, Shear horizontal wave excitation and reception with shear horizontal piezoelectric wafer active sensor (SH-PWAS). Smart Mater. Struct. 2014, 23, 085019.

[Kolsky, 1963] H. Kolsky, Stress Waves in Solids, 2nd ed. Dover, New York (1963)

[Koshiba et al, 1987] M. Koshiba; K. Hasegawa; M. Suzuki, Finite-element solution of horizontally polarized shear wave scattering in an elastic plate. IEEE Trans Ultrason Ferroelectr Freq Control 1987; 34(4):461–6.

[Lamb, 1917] H. Lamb, On waves in an elastic plate. In Pro. R. Sos. London, Ser. A, pages 114-128,1917.

[Lamé, 1852] G. Lamé, Leçons sur la Theorie Mathématique de l'Elasticité des Corps Solides. Bachelier, Paris (1852)

[Lawrie and Kaplunov, 2012] J.B. Lawrie, and J. Kaplunov, Edge waves and resonance on elastic structures: an overview, Mathematics and Mechanics of Solids, 17 (2012) 4-16.

[Love, 1906] A.E.N. Love, A Treatise on the Mathematical Theory of Elasticity. Cambridge University Press (1906)

[Lowe and Diligent, 2002] MJS. Lowe; O. Diligent, Low-frequency reflection characteristics of the S0 Lamb wave from a rectangular notch in a plate. J Acoust Soc Am 2002; 111(1):64–74.

[Miklowitz, 1980] J. Miklowitz, The Theory of ElasticWaves andWaveguides, 2nd ed. North-Holland, Amsterdam (1980)

[Mofakhami and Boller, 2008] M. Mofakhami and C. Boller, Lamb wave interactions with non-symmetric features at structural boundaries, Zeitschrift für Angewandte Mathematik und Mechnik (ZAMM), (2008).

[Mohammedi et al, 2019] B. Mohammedi; N. Sobh, D. Abueidda, A. Belgacem-Bouzida, Analysis.of edge defects in an elastic plate using SH waves. Journal of Mechanical Science and Technology 2019; 33(1):87–94.

[Morvan et al, 2003] B. Morvan, N. Wilkie-Chancellier, H. Duflo, A. Tinel and J. Duclos, Lamb wave reflection at the free edge of a plate, The Journal of the Acoustical Society of America, 113 (2003) 1417-1425.

[Nakamura et al, 2012] N. Nakamura, H. Ogi, M. Hirao and K. Nakahata, Mode conversion behavior of SH guided wave in a tapered plate, NDT & E International, 45 (2012) 156-161.

[Ostachowicz et al, 2011] W. Ostachowicz, P. Kudela, M. Krawczuk and A. Zak, Guided waves in structures for SHM: the time-domain spectral element method, John Wiley & Sons, West Sussex, UK, (2011).

[Petcher et al, 2013] P. Petcher, S. Burrows & S.Dixon, Shear horizontal (SH) ultrasound wave propagation around smooth corners. Ultrasonics. 2013.

[Poisson, 1829] S.D. Poisson, Mémoire sur les équations générales de l'equilibre et du mouvement des corps élastiques et des fluides. J. École Poly. 13(20), 1–174 (1829)

[Pujol, 2003] J. Pujol, Elastic wave propagation and generation in seismology, Cambridge university press, UK, (2003).

[Rajagopal and Lowe, 2007] P. Rajagopal; MJS. Lowe, Short range scattering of the fundamental shear horizontal guided wave mode normally incident at a through-thickness crack in an isotropic plate. J Acoust Soc Am 2007; 122(3):1527–38.

[Rayleigh and Lindsay, 1945] J. W. S. B. Rayleigh, & R. B. Lindsay, The Theory of Sound, Dover. 1945.

[Redwood, 1960] M. Redwood, Mechanical Wave-Guides, The Propagation of Acoustic and Ultrasonic Waves in Fluids and Solids with Boundaries, Pergamon, New York 1960.

[Rose, 1999] J. L. Rose, Ultrasonic Waves in Solid Media, Cambridge University Press 1999.

[Rose, 2000] J.L. Rose, Guided wave nuances for ultrasonic nondestructive evaluation, IEEE Transactions on ultrasonics, ferroelectrics, and frequency control, 47 (2000) 575-583.

[Rose, 2014] J.L. Rose, Ultrasonic guided waves in solid media, Cambridge university press, NY, USA, (2014).

[Royer and Dieulesaint, 2000] D. Royer, & E. Dieulesaint, Elastic Waves in Solids I: Free and Guided Propagation, Springer. 2000.

[Santhanam and Demirli, 2013] S. Santhanam and R. Demirli, Reflection of Lamb waves obliquely incident on the free edge of a plate, Ultrasonics, 53 (2013) 271-282.

[Staszewski et al, 2004] W. Staszewski; C. Boller; G.R. Tomlinson, Health Monitoring of Aerospac Structures: Smart Sensor Technologies and Signal Processing; JohnWiley & Sons: Hoboken, NJ,USA, 2004.

[Victorov, 1970] I. A. Victorov, Rayleigh and Lam waves. Plenum Press, New York. 1970.

[Whitham, 1974] G.B. Whitham, Linear and Nonlinear Waves. Wiley, New York (1974)

Springer

KSME

Journal of Mechanical Science and Technology 33 (1) (2019) 87~94
www.springerlink.com/content/1738-494x(Print)/1976-3824(Online)
DOI 10.1007/s12206-018-1209-2

Analysis of edge defects in an elastic plate using SH-waves †

Brahim Mohammedi[1,2], Nahil A Sobh[2,*], Diab Abueidda[3] and Belgacem-Bouzida Aissa[4]

[1]*Laboratoire de Recherche en Productique, University Mostefa Benboulaid Batna2, Algeria*
[2]*Beckman Institute for Advanced Science and Technology, University of Illinois at Urbana-Champaign, USA*
[3]*Department of Mechanical Science and Engineering, University of Illinois at Urbana-Champaign, USA*
[4]*Department of Physics, University of Batna1, Algeria*

(Manuscript Received February 15, 2018; Revised June 27, 2018; Accepted July 31, 2018)

Abstract

The interaction of guided SH-waves with the beveled free end of a semi-infinite plate is analytically and numerically investigated. The material of the plate is assumed to be elastic, homogenous, and isotropic. The plate is modeled as a combination of a semi-infinite region and bounded wedged region separated by a common boundary. The analytical solution of the vertical free end case for the two regions is derived and used in verifying the numerical implementation. In this study, the SH_0 and the SH_1 first two incident modes are individually applied to analyze the corresponding reflected modes from the free end. Specifically, the elastic energy carried by the reflected modes is reported for a wide range of beveled angles and incident frequencies.

Keywords: Bevel end; Edge defects; Elastic plate; SH waves; Wave function

1. Introduction

Although experimental observations of dynamic edge phenomenon in elastic waveguides took place over 70 years ago, the reflection of guided waves from the free end of an elastic layer remains an active area of research. Lawrie et al. [1] provided a detailed review of the field that covered the period from 1958 to 2008. Within this context, a follow-up review was done by Deckers et al. [2] in which they discussed and summarized research on wave-based methods.

Researchers have made tremendous advancements utilizing mode and frequency selections to solve many problems; for example, in the testing of pipes, rails, plates, ship hulls, and aircraft integrity [3-5]. In recent years, the inspection of irregularities and defects such as cracks have been carried out using horizontally polarized shear (SH) waves generated and detected by electromagnetic-acoustic transducers [6-8].

The study of scattering problems varies from classical approaches such as mode matching and variational techniques to numerical techniques such as finite element and boundary element approaches, or a combination of numerical formulations with a wave function expansion technique. Among these, Abduljabbar et al. [9] studied the diffraction of SH waves in a plate with arbitrary defects by employing a finite element formulation and wave function expansion technique. Furthermore, Chen et al. [10] studied the SH guided waves propagated in a tapered plate using eigenmode matching theory and finite element methods. Ditri [11] dealt with the scattering of guided elastic SH waves from material and geometric waveguide discontinuities. Nurmalia et al. [12] studied the mode conversion behavior of an SH guided wave in a tapered plate. They investigated the different mode conversion phenomenon for abrupt and gradual thickness changes.

Many investigations have been made to study the beveled end of plates using Lamb waves. A semi-analytical finite element method has been used to simulate Lamb wave reflections at plate edges [13]. The Lamb wave conversion due to the beveled free end of plates has been studied theoretically as well as numerically, using the finite element method [14, 15].

Chancellier et al. used a collocation method on the beveled free end to determine the Lamb wave amplitudes and edge resonance [16]. Several experimental works have been published on the reflection of Lamb waves by the free and beveled edge of a plate [17-20]. In these papers, the mode conversions were examined in detail over a large frequency range, and the energy conversion coefficients were obtained both numerically (finite element method) and experimentally.

In this paper, a wave function expansion is used to investigate the interactions of SH waves with the beveled free end of an elastic plate. The plate is divided into two non-overlapping regions with a common interface. Each region admits a separable solution of the corresponding wave equation. The total solution is assembled by enforcing continuity conditions at the

*Corresponding author. Tel.: +1 217 244 9481, Fax.: +1 217 333 2922
E-mail address: sobh@illinois.edu
† Recommended by Associate Editor Junhong Park

interface. The solution preserves the total incident energy to within a small tolerance. The convergence of the solution is met when the difference between the total incident energy and reflected energy is less than 0.001 % which is a very tight criterion compared to existing convergence criteria reported in many works available in the Refs. [9, 11, 18, 19]. The solution provided here is compared with the known solution for a plate with a vertical end [3, 5]. Very good agreement between the proposed numerical approach and analytical solution is observed. This indicates the effectiveness of the proposed approach. A wide range of beveled angles and incident frequencies are studied and reported here.

The main contribution of this work is in the identification of critical bevel-angles/frequencies pairs, where incident waves are totally reflected or totally converted into a different mode. These findings were made possible by the highly accurate and fast solutions that swept through an extensive range of bevel angles and incident frequencies.

2. Formulation of reflected waves from a beveled free end

The waveguide studied in this paper is shown in Fig. 1(a). It represents a plate of uniform thickness d having a bevel angle α. The plate is bounded on the three sides by traction-free surfaces denoted Γ_1, Γ_2 and Γ_3, and it is assumed to be elastic, homogeneous, and isotropic with shear modulus μ and the density ρ. The coordinate systems, the extent of regions I and II, and their common artificial boundary Γ_4 are all depicted in Fig. 1(b). A Cartesian coordinate system, for region I, is constructed where its origin is located at the tip of the beveled end, the positive *x*-axis is aligned with the lower surface, and the *y*-axis increases upwards. The origin of the Cartesian coordinates also serves as the origin of the polar coordinates system for region II. The polar angle θ increases counterclockwise starting at the positive *x*-axis and ending at the beveled edge Γ_3. The radius of the polar coordinates *r* has a maximum value of $R = d / \sin\alpha$.

As illustrated in Fig. 1(a), an incident SH wave traveling in the negative *x*-direction impinges on the beveled free end of the plate and reflects back in the positive *x*-direction. The corresponding displacement field U in the plate is made of the incident U^{inc} and the reflected U^{ref} displacements fields,

$$U = U^{inc} + U^{ref}. \tag{1}$$

The geometry of the plate admits an equivalent formulation whereby the plate is divided into two regions as shown in Fig. 1(b). The incident SH wave traveling in region I impinges on the artificial boundary Γ_4, reflects and sets up a standing wave in the bounded region II.

The solutions for the out-of-plane, time-dependent particle displacement fields U_z^I and U_z^{II}, in regions I and II respectively, are governed by the following wave equations,

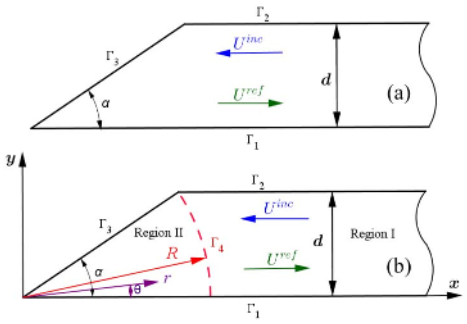

Fig. 1. (a) Geometry of the plate structure showing incident and reflected waves; (b) partitioned wedge-plate regions and common fictitious boundary.

$$\frac{\partial^2 U_z^I}{\partial x^2} + \frac{\partial^2 U_z^I}{\partial y^2} = \frac{1}{c^2}\frac{\partial^2 U_z^I}{\partial t^2} \tag{2}$$

$$\frac{\partial^2 U_z^{II}}{\partial r^2} + \frac{1}{r}\frac{\partial U_z^{II}}{\partial r} + \frac{1}{r^2}\frac{\partial^2 U_z^{II}}{\partial \theta^2} = \frac{1}{c^2}\frac{\partial^2 U_z^{II}}{\partial t^2} \tag{3}$$

where $c = (\mu/\rho)^{1/2}$ is the shear velocity, while *t* denotes time. The interface continuity of displacement and stress conditions at Γ_4 are given by

$$U_z^I = U_z^{II} \tag{4}$$

$$\sigma_{nz}^I = \sigma_{rz}^{II}. \tag{5}$$

σ_{nz}^I is the shear stress in region I and is given by

$$\sigma_{nz}^I = \sigma_{xz}^I \cos\theta + \sigma_{yz}^I \sin\theta \tag{6}$$

while σ_{rz}^{II} is the shear stress in region II. Finally, the traction-free boundary conditions on traction free sides of the plate are given by:

$$\sigma_{yz}^I = 0 \quad ; \quad y = 0, d \tag{7}$$

$$\sigma_{\theta z}^{II} = 0 \quad ; \quad \theta = 0, \alpha \tag{8}$$

where σ_{yz}^I is the out-of-plane shear stress acting on the two boundaries, Γ_1 and Γ_2 of region I, while $\sigma_{\theta z}^{II}$ is the out-of-plane shear stress acting on the two boundaries, Γ_1 and Γ_3 of region II.

The SH waves are assumed to be time harmonic, and hence the out-of-plane z-displacement fields in regions I and II are given by,

$$U_z^I = u_z^I(x,y)e^{i\omega t} \tag{9}$$

$$U_z^{II} = u_z^{II}(r,\theta)e^{i\omega t} \tag{10}$$

where ω is the applied frequency and $i^2 = -1$. u_z^I and u_z^{II} represent the steady state displacements fields in the regions I and II, respectively. Substituting Eqs. (9) and (10) into Eqs. (2) and (3), respectively, results in the steady-state form of the governing equations in each region

$$\frac{\partial^2 u_z^I}{\partial x^2}+\frac{\partial^2 u_z^I}{\partial y^2}=\frac{-\omega^2}{c^2}u_z^I \tag{11}$$

$$\frac{\partial^2 u_z^{II}}{\partial r^2}+\frac{1}{r}\frac{\partial u_z^{II}}{\partial r}+\frac{1}{r^2}\frac{\partial^2 u_z^{II}}{\partial \theta^2}=\frac{-\omega^2}{c^2}u_z^{II}. \tag{12}$$

Eqs. (11) and (12) are also known as the Helmholtz equations in rectangular and cylindrical coordinates, respectively. The geometry of the regions renders the solutions of Eqs. (11) and (12) as separable. In other words, the solutions to the Helmholtz equations can be expressed as an infinite sum of wave functions.

The separable series solution for Eq. (11) is given by

$$u_z^I(x,y)=C_q h_q(x,y)+\sum_{m=0}^{\infty}A_m \ell_m(x,y) \tag{13}$$

with:

$$h_q(x,y)=\cos\left(\frac{q\pi}{d}y\right)e^{-ik_q x}\ ;\ \ \ell_m(x,y)=\cos\left(\frac{m\pi}{d}y\right)e^{ik_m x}.$$

Note, each term of the series solution in Eq. (13) satisfies the traction-free boundary condition in Eq. (7) along Γ_1 and Γ_2. C_q is the amplitude of the q^{th} incident mode, A_m is the amplitude of the m^{th} reflected mode, and the wave numbers k_m and k_q are defined as,

$$k_m=\sqrt{\frac{\omega^2}{c^2}-\frac{m^2\pi^2}{d^2}} \tag{14}$$

$$k_q=\sqrt{\frac{\omega^2}{c^2}-\frac{q^2\pi^2}{d^2}}. \tag{15}$$

Similarly, the separable solution of Eq. (12) is represented as an infinite Bessel-Fourier sum,

$$u_z^{II}(r,\theta)=\sum_{n=0}^{\infty}B_n\cos\left(\frac{n\pi}{\alpha}\theta\right)J_{n\pi/\alpha}(k_0 r). \tag{16}$$

Each term of the Fourier series in Eq. (16) satisfies the traction free boundary conditions Eq. (8) along Γ_1 and Γ_3. B_n denotes the n^{th} amplitude of the standing wave in region II, $J_{n\pi/\alpha}$ is the Bessel function of the first kind of order $n\pi/\alpha$ and k_0 is defined as $k_0=\omega/c$.

The stress field in region I is given by,

$$\begin{aligned}\sigma_{xz}^I&=\mu\frac{\partial u_z^I}{\partial x}=-\mu i k_q h_q(x,y)+\mu\sum_{m=0}^{M}ik_m A_m \ell_m(x,y)\\ \sigma_{yz}^I&=\mu\frac{\partial u_z^I}{\partial y}=-\mu\frac{q\pi}{d}C_q\tilde{h}_q(x,y)+\mu\sum_{m=0}^{M}\frac{-m\pi}{d}A_m\tilde{\ell}_m(x,y)\end{aligned} \tag{17}$$

with

$$\tilde{h}_q(x,y)=\sin\left(\frac{q\pi}{d}y\right)e^{-ik_q x}\ \ ;\ \ \tilde{\ell}_m(x,y)=\sin\left(\frac{m\pi}{d}y\right)e^{ik_m x}.$$

Additionally, the stress field in region II is given by

$$\sigma_{rz}^{II}=\mu\frac{\partial u_z^{II}}{\partial r}=\mu\sum_{n=0}^{N}k_0\ B_n\cos\left(\frac{n\pi}{\alpha}\theta\right)\frac{\partial J_{n\pi/\alpha}}{\partial r}(k_0 r). \tag{18}$$

Substituting the series solutions Eqs. (13), (16), (17), (18) in the continuity Eqs. (4) and (5), and after limiting the infinite sums to a finite number of terms, M and N, and transposing the known incident terms to the right-hand side, the displacement and stress continuity conditions are now expressed as,

$$\sum_{m=0}^{M}\ell_m(x,y)A_m-\sum_{n=0}^{N}\cos\left(\frac{n\pi}{\alpha}\theta\right)J_{n\pi/\alpha}(k_0R)B_n=-h_q(x,y)C_q \tag{19}$$

$$\sum_{m=0}^{M}f_m(y,\theta)e^{ik_m x}A_m-\sum_{n=0}^{N}k_0\cos\left(\frac{n\pi}{\alpha}\theta\right)\frac{\partial J_{n\pi/\alpha}}{\partial r}(k_0R)B_n=g_q(y,\theta)e^{-ik_q x}C_q \tag{20}$$

where

$$f_m(y,\theta)=ik_m\cos\left(\frac{m\pi}{d}y\right)\cos\theta-\frac{m\pi}{d}\sin\left(\frac{m\pi}{d}y\right)\sin\theta$$

$$g_q(y,\theta)=\left[ik_q\cos\left(\frac{q\pi}{d}y\right)\cos\theta+\frac{q\pi}{d}\sin\left(\frac{q\pi}{d}y\right)\sin\theta\right].$$

Eqs. (19) and (20) are now projected onto $\cos(p\pi\theta/\alpha)$ as shown below,

$$\int_0^{\alpha}\sum_{m=0}^{M}A_m\cos\left(\frac{p\pi}{\alpha}\theta\right)\cos\left(\frac{m\pi}{d}y\right)e^{ik_m x}d\theta-\int_0^{\alpha}\sum_{n=0}^{N}B_n\cos\left(\frac{p\pi}{\alpha}\theta\right)\cos\left(\frac{n\pi}{\alpha}\theta\right)J_{n\pi/\alpha}(k_0R)d\theta=-C_q\int_0^{\alpha}\cos\left(\frac{p\pi}{\alpha}\theta\right)\cos\left(\frac{q\pi}{d}y\right)e^{-ik_q x}d\theta \tag{21}$$

$$\int_0^{\alpha}\sum_{m=0}^{M}A_m\cos\left(\frac{p\pi}{\alpha}\theta\right)f_m(y,\theta)e^{ik_m x}d\theta-\int_0^{\alpha}\sum_{n=0}^{N}B_n k_0\cos\left(\frac{p\pi}{\alpha}\theta\right)\cos\left(\frac{n\pi}{\alpha}\theta\right)\frac{\partial J_{n\pi/\alpha}}{\partial r}(k_0R)d\theta=C_q\int_0^{\alpha}\cos\left(\frac{p\pi}{\alpha}\theta\right)g_q(y,\theta)e^{-ik_q x}d\theta \tag{22}$$

where

$$\begin{aligned}x&=R\cos\theta\\ y&=R\sin\theta.\end{aligned} \tag{23}$$

The solution of Eqs. (21) and (22) is obtained by choosing $N=M$ and setting $p=0,\ldots,M$. The resulting algebraic system of equations, of size $2M\times 2M$, is subsequently solved to

determine the amplitudes A_m and B_n. The value of M is increased iteratively until the relative energy error ε, shown in Eq. (24), satisfies the desired tolerance.

$$\varepsilon = \frac{\left(E_q^{inc} - \sum_{m=0}^{M} E_m^{ref}\right)}{E_q^{inc}} \tag{24}$$

where E_q^{inc} is the energy flux carried by the specified incident mode while E_m^{ref} represents the energy flux of m^{th} reflected mode. E_q^{inc} and E_m^{ref} are defined below [9].

$$E_m^{ref} = \begin{cases} \frac{d}{4}\mu\omega k_m |A_m|^2, & m \neq 0 \\ \frac{d}{2}\mu\omega k_m |A_m|^2, & m = 0 \end{cases} \tag{25}$$

$$E_q^{inc} = \begin{cases} \frac{d}{4}\mu\omega k_q |C_q|^2, & q \neq 0 \\ \frac{d}{2}\mu\omega k_q |C_q|^2, & q = 0 \end{cases} \tag{26}$$

where $|\ |$ denotes the absolute value. R_{mq} is used to denote the ratio of the elastic energy flux contained in reflected mode m to the elastic energy flux supplied by incident mode q

$$R_{mq} = \frac{E_m^{ref}}{E_q^{inc}}. \tag{27}$$

Substituting Eq. (27) in Eq. (24) results in the following expression for the relative error in the elastic energy flux,

$$\varepsilon = 1 - \sum_{m=0}^{M} R_{mq}. \tag{28}$$

In this paper, the series solutions Eqs. (13) and (16) are considered to be convergent when the corresponding relative error ε does not exceed 1×10^{-5}.

3. A plate with a vertical edge (beveled angle = 90°)

The case of $\alpha = \pi/2$, as shown in Fig. 2, corresponds physically to a waveguide of a semi-infinite plate with a vertical edge. In this special case, the stress-free boundary conditions at Γ_3 are expressed in rectangular coordinates as

$$\sigma_{xz}^{I} = 0. \tag{29}$$

Substitution of the stress expression given in Eq. (17) into Eq. (29) results in the following relationship between incident and reflected modes,

$$\sum_{m=0}^{M} A_m \left[ik_m \cos\left(\frac{m\pi}{d}\mathrm{y}\right)\right] = -C_q \left[-ik_q \cos\left(\frac{q\pi}{d}\mathrm{y}\right)\right]. \tag{30}$$

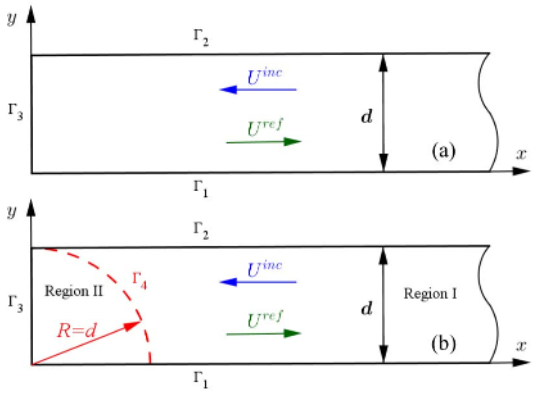

Fig. 2. (a) Plate structure with vertical free end; (b) partitioned wedge-plate regions and common fictitious boundary.

Using the orthogonality of modes, Eq. (30) has the following analytical solution for the amplitude of the reflected modes,

$$\begin{aligned} &A_q = C_q \\ &A_m = 0 \quad ; \quad m = 0,1,2,...,M \quad m \neq q. \end{aligned} \tag{31}$$

The above result is obtained by (a) multiplying both sides of Eq. (30) by $\cos(n\pi y/d)$, (b) integrating the resulting Equation over y from 0 to d, (c) making use of the orthogonality of the trigonometric functions over Γ_3, (d) taking the corresponding incident q^{th} mode ($q = 0,1$). Eq. (31) manifests the well-known fact that an incident mode reflects from the vertical free end of the waveguide are totally reflected back.

The same solution to the vertical free end can be found by dividing the domain into two regions as shown in Fig. 2(b). Substitution of Eq. (31) into the continuity condition at the artificial interface described in Eqs. (4) and (5) yields

$$\begin{aligned} &C_q \cos\left(\frac{q\pi}{d}y\right)\left(e^{-ik_q x} + e^{ik_q x}\right) = \\ &\sum_{n=0}^{N} B_n \cos(2n\theta) J_{2n}(k_0 R). \end{aligned} \tag{32}$$

At the interface $x = R\cos\theta$ and for the zeroth incident mode $q = 0$, Eq. (32) reduces to

$$\begin{aligned} &C_0 2\cos(k_0 R\cos\theta) = \\ &B_0 J_0(k_0 R) + \sum_{n=1}^{N} B_n \cos(2n\theta) J_{2n}(k_0 R). \end{aligned} \tag{33}$$

The well-known Jacobi-Anger expansion is

$$\begin{aligned} &\cos(k_0 R\cos\theta) = \\ &J_0(k_0 R) + 2\sum_{n=1}^{\infty}(-1)^n J_{2n}(k_0 R)\cos(2n\theta). \end{aligned} \tag{34}$$

Comparing Eqs. (33) and (34), while setting $C_0 = 1$, the

unknown coefficients can be found

$$B_0 = 2$$
$$B_n = 4(-1)^n \quad n = 1,2,...,N. \tag{35}$$

B_n in Eq. (35) are used in verifying the accuracy of the truncated series solution proposed above.

4. Results and discussions

A non-dimensional form of Eqs. (14) and (15) is adopted and used in reporting numerical results found in this study. The non-dimensional wave number $K_m = k_m d/\pi$ and the non-dimensional frequency $\Omega = \omega d/\pi c$ are substituted into Eqs. (14) and (15) to arrive at the following non-dimensional frequency relationships,

$$K_m = \sqrt{\Omega^2 - m^2} \tag{36}$$
$$K_q = \sqrt{\Omega^2 - q^2}. \tag{37}$$

When an incident guided wave impinges on the beveled end of a semi-infinite plate, it induces a collection of both propagating and non-propagating reflected modes. The elastic energy of the reflected propagating modes is reported in this section for both SH_0 and SH_1 incident modes for a wide range of corresponding beveled angles and frequencies. The energy is reported as the ratio between the energy of the reflected m^{th} mode and the energy of the q^{th} incident mode. This ratio is denoted by R_{mq}. Specifically, R_{m0} denotes the ratio of elastic energy content in the m^{th} reflected mode relative to SH_0 incident mode (q = 0). Similarly, R_{m1} corresponds to the ratio of elastic energy content in m^{th} reflected mode relative to the SH_1 incident mode (q = *1*). The number of terms in the series solution given in Eqs. (13) and (16), M (in region I) and N (in region II), are chosen to guarantee that the energy error ε, defined in Eq. (28), does not exceed 1×10^{-5}.

4.1 Energy variation with normalized frequency at selected beveled angles

Figs. 3-6 show the R_{m0} and R_{m1} distribution due to SH_0 and SH_1 incident modes. The variation of R_{m0} versus Ω, due to the SH_0 incident mode, is displayed in Figs. 3(a)-(c) which correspond to $\alpha = 30°$, $45°$ and $60°$, respectively.

• **Mode Dominance of SH_0**: When the beveled angle is $30°$ (Fig. 3(a)) or $45°$ (Fig. 3(b)), R_{00} is strictly larger than R_{m0} ($m \neq 0$) over the entire frequency range. For $\alpha = 30°$ (Fig. 3(a)), the minimum value of R_{00} is 0.523 which is attained when $\Omega = 1.13$. While when $\alpha = 45°$ (Fig. 3(b)) the minimum value of R_{00} is 0.634 and is attained when $\Omega = 1.07$. For $\alpha = 60°$ (Fig. 3(c)), R_{00} loses its dominance and vanishes at the following frequencies: 1.155, 2.309, 3.464 and 4.619.

• **Total Reflection of SH_0**: In Fig. 3, $R_{00} = 1$ at certain beveled angle and frequency values, which corresponds to total reflection of the incident mode SH_0. At the beveled angles $\alpha = 30°$ and $60°$, the total reflection occurs when $\Omega = 2$ (which is also a cut-off frequency). When $\alpha = 45°$, $R_{00} = 1$ at all cutoff frequencies (1, 2, 3, 4, 5) and when $\Omega = 1.414$.

• **Mode conversion of SH_0:** When $\alpha = 60°$ and for, $\Omega = 1.155$ SH_1 is the only reflected mode, similarly when $\Omega = 2.309$, 3.464 and 4.619 the SH_2, SH_3 and SH_4 are the corresponding total reflected modes, respectively.

• **Mode Dominance SH_1**: Unlike the dominance of the SH_0 mode over the entire frequency range, the SH_1 mode shows partial dominance as shown in Figs. 4(a) and (b).

• **Total Reflection SH_1:** At the beveled angle $\alpha = 30°$, the total reflection is attained when $\Omega = 1$ and $\Omega = 2$. For the case of $\alpha = 45°$, total reflection of the incident SH_1 mode is obtained when $\Omega = 1$, $\Omega = 1.412$ and $\Omega = 2$. At the beveled angle $\alpha = 60°$, the total reflection is attained when $\Omega = 1$, $\Omega = 2$ and $\Omega = 2.309$.

• **Mode conversion of SH_1:** When $\alpha = 60°$ and for $\Omega = 1.155$, 3.055, 4.163 and 5.292, SH_1 disappears ($R_{11} = 0$) giving way to other modes to carry the reflected energy.

The abrupt variations at the cutoff frequencies in Figs. 3 and 4 are due to the inception of new propagating modes, which cause a sudden change in the distribution of energy in the spectra of the reflected and transmitted waves. Remarkably, the variation in the energy ratios is more abrupt when the beveled angle is increased (see Figs. 3 and 4).

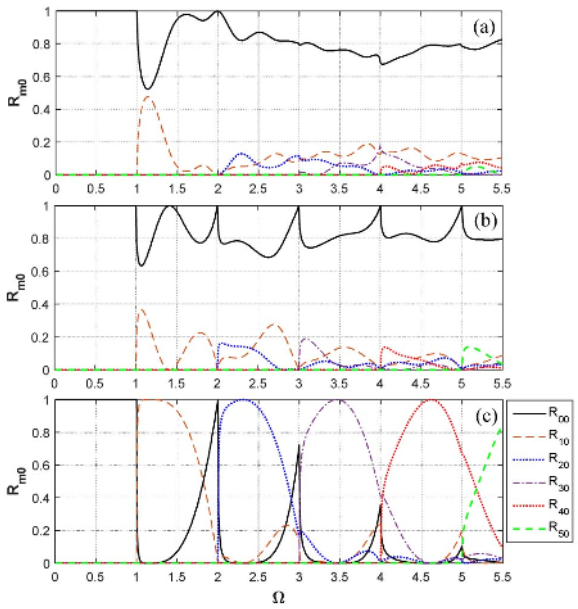

Fig. 3. R_{m0} versus normalized frequency for the selected beveled edges: (a) $\alpha = 30°$; (b) $\alpha = 45°$; (c) $\alpha = 60°$.

4.2 Energy variation with beveled angle and selected frequencies

In Subsec. 4.1, the variation of the normalized frequency Ω versus three beveled angles, namely $\alpha = 30°$, $\alpha = 45°$ and $\alpha = 60°$ was reported. However, in this subsection, the

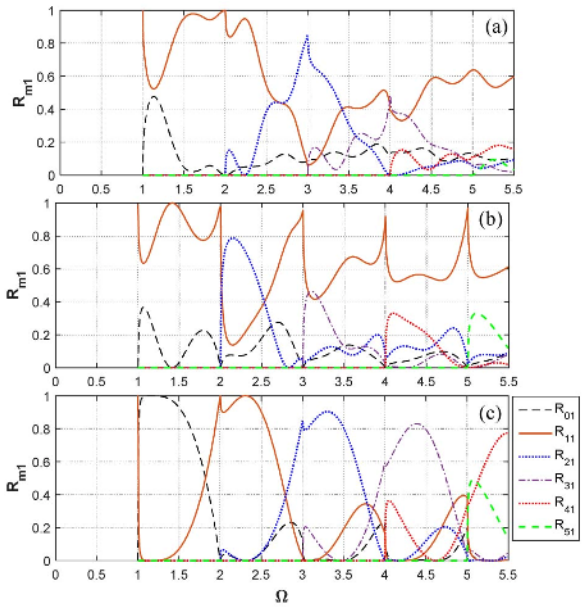

Fig. 4. R_{m1} versus normalized frequency for the selected beveled edges: (a) $\alpha = 30°$; (b) $\alpha = 45°$; (c) $\alpha = 60°$.

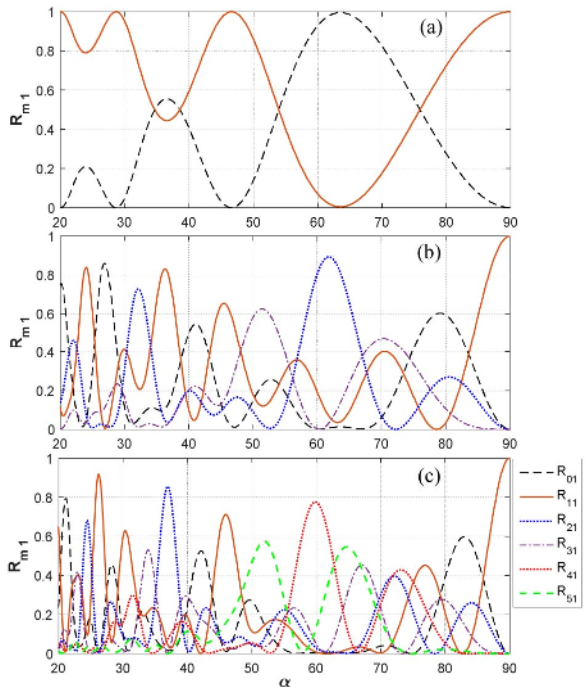

Fig. 5. R_{m0} versus beveled edge angle for selected normalized frequencies: (a) $\Omega = 1.5$; (b) $\Omega = 3.5$; (c) $\Omega = 5.5$.

variation of the beveled angle $20° \le \alpha \le 90°$ for selected frequencies $\Omega = 1.5$, 3.5 and 5.5, is investigated to determine the interaction of SH waves with a range of beveled angles.

In Fig. 5, R_{m0} versus beveled edge angle at three selected normalized frequencies, namely 1.5, 3.5 and 5.5, is reported. These frequencies are selected to be halfway between the cut-off frequencies. In Fig. 5(a), SH_0 gradually decreases until it

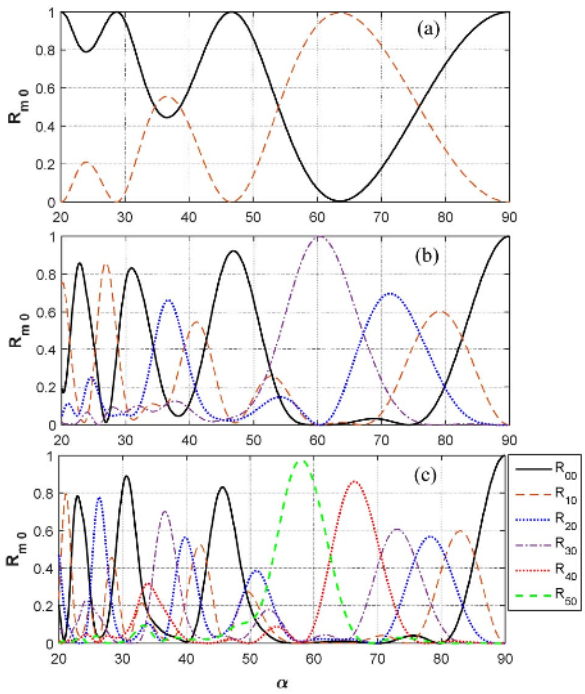

Fig. 6. R_{m1} versus beveled edge angle for selected normalized frequencies: (a) $\Omega = 1.5$; (b) $\Omega = 3.5$; (c) $\Omega = 5.5$.

diminishes, $R_{00} = 0$, after which it increases and reaches total reflection, $R_{00} = 1$, when $\Omega = 1.5$ and $\alpha = 20.019°$, 28.67°, 46.60°. Figs. 5(b) and (c) show the region where SH_0 is very small compared to the other propagating modes. This region is centered around $\alpha = 63°$.

Similarly, in Fig. 6 R_{m1} versus beveled edge angle at the three selected normalized frequencies is displayed. SH_1 gradually decreases until it diminishes, $R_{11} = 0$, after which it increases and reaches total reflection, $R_{11} = 1$, when $\Omega = 1.5$, $\alpha = 28.67°$ and 46.60°. The region of vanishing R_{11} is not as extreme as in the case of R_{00} .

5. Conclusion

The diffraction of SH waves by the beveled free end of a semi-infinite plate is examined, and its numerical solution is determined for a wide range of frequencies and bevel angles. The solution uses the separability property of the Helmholtz equations, for both rectangular and cylindrical coordinates, and the continuity condition across an artificial boundary. This strategic selection of the regions leads to an efficient separable solution for the unknown coefficients. In this study, single incident modes were used, and a range of frequencies was considered. Continuity conditions at the common boundary between the two regions led to a set of algebraic equations. The solution of these algebraic equations has a relative energy error that does not exceed 1×10^{-5} . This study has shown the existence of critical bevel angles where an incident mode is either "totally" reflected or "totally" absorbed at a specific incident frequency.

Acknowledgments

The first author would like to acknowledge the support of the Algerian ministry of higher education and scientific research to conduct this research during his stay at the University of Illinois at Urbana-Champaign, USA.

Nomenclature

c	: Shear velocity
d	: Thickness
$J_{n\pi/\alpha}$	: Bessel function
k_m, k_q	: Wave numbers
U	: Displacement field
α	: Bevel angle
ε	: Relative energy error
θ	: Polar angle
μ	: Shear modulus
ρ	: Density
σ	: Stress
ω	: Frequency

References

[1] J. B. Lawrie and J. Kaplunov, Edge waves and resonance on elastic structures: an overview, *Mathematics and Mechanics of Solids,* 17 (2012) 4-16.

[2] E. Deckers, O. Atak, L. Coox, R. D'Amico, H. Devriendt, S. Jonckheere, K. Koo, B. Pluymers, D. Vandepitte and W. Desmet, The wave based method: An overview of 15 years of research, *Wave Motion*, 51 (2014) 550-565.

[3] V. Giurgiutiu, *Structural health monitoring: with piezoelectric wafer active sensors*, Academic Press, MA, USA (2007).

[4] W. Ostachowicz, P. Kudela, M. Krawczuk and A. Zak, *Guided waves in structures for SHM: The time-domain spectral element method*, John Wiley & Sons, West Sussex, UK (2011).

[5] J. L. Rose, *Ultrasonic guided waves in solid media*, Cambridge University Press, NY, USA (2014).

[6] J. L. Rose, Guided wave nuances for ultrasonic nondestructive evaluation, *IEEE Transactions on Ultrasonics, Ferroelectrics, and Frequency Control*, 47 (2000) 575-583.

[7] H. Gao, S. Ali and B. Lopez, Efficient detection of delamination in multilayered structures using ultrasonic guided wave *EMATs, NDT & E International*, 43 (2010) 316-322.

[8] M. Hirao and H. Ogi, An SH-wave EMAT technique for gas pipeline inspection, *NDT & E International*, 32 (1999) 127-132.

[9] Z. Abduljabbar, S. Datta and A. Shah, Diffraction of horizontally polarized shear waves by normal edge cracks in a plate, *Journal of Applied Physics*, 54 (1983) 461-472.

[10] J.-J. Chen, G.-H. Song and X. Han, Asymmetric first order shear horizontal guided waves propagation in a tapered plate, *Physics Letters A*, 379 (2015) 2125-2129.

[11] J. J. Ditri, Some results on the scattering of guided elastic SH waves from material and geometric waveguide discontinuities, *The Journal of the Acoustical Society of America*, 100 (1996) 3078-3087.

[12] N. Nakamura, H. Ogi, M. Hirao and K. Nakahata, Mode conversion behavior of SH guided wave in a tapered plate, *NDT & E International*, 45 (2012) 156-161.

[13] Z. Ahmad and U. Gabbert, Simulation of Lamb wave reflections at plate edges using the semi-analytical finite element method, *Ultrasonics*, 52 (2012) 815-820.

[14] N. Wilkie-Chancellier, H. Duflo, A. Tinel and J. Duclos, Theoretical study of lamb wave conversion at the edge of different angles bevelled plates, *Forum Acusticum*, Seville (2002) 17-21.

[15] M. Mofakhami and C. Boller, Lamb wave interactions with non-symmetric features at structural boundaries, *Zeitschrift für Angewandte Mathematik und Mechnik (ZAMM)* (2008).

[16] N. Wilkie-Chancellier, H. Duflo, A. Tinel and J. Duclos, Numerical description of the edge mode at the beveled extremity of a plate, *The Journal of the Acoustical Society of America,* 117 (2005) 194-199.

[17] M. Castaings, E. Le Clezio and B. Hosten, Modal decomposition method for modeling the interaction of Lamb waves with cracks, *The Journal of the Acoustical Society of America*, 112 (2002) 2567-2582.

[18] B. Morvan, N. Wilkie-Chancellier, H. Duflo, A. Tinel and J. Duclos, Lamb wave reflection at the free edge of a plate, *Journal of the Acoustical Society of America*, 113 (2003) 1417-1425.

[19] N. Wilkie-Chancellier, H. Duflo, A. Tinel and J. Duclos, Energy balance in the conversion of a Lamb wave at a bevelled edge, *Acta Acustica United with Acustica*, 90 (2004) 77-84.

[20] S. Santhanam and R. Demirli, Reflection of Lamb waves obliquely incident on the free edge of a plate, *Ultrasonics*, 53 (2013) 271-282.

Brahim Mohammedi received his M.S. in mechanical engineering from the University of Colorado at Boulder USA. He is currently a lecturer at the Faculty of Technology, University of Batna 2. His research interests include solid mechanics, waves in elastic solids and elasticity problems.

Diab Abueidda received his M.Sc. in mechanical engineering from Masdar Institute of Science and Technology and his B.Sc. from American University of Sharjah. Both are in the United Arab Emirates. Currently, he is a Ph.D. student at the University of Illinois at Urbana-Champaign. His research interest includes computational and experimental solid mechanics, topology optimization, and nano-/micro-fabrication.

Nahil A. Sobh received his Ph.D. in Applied Mathematics and Ph.D. in Civil engineering from the University of Colorado at Boulder USA. He is currently lead scientist of Beckman Institute for Advanced Science and Technology, Carl R. Woese Institute for Genomic Biology, Department of Civil and Environmental Engineering, and an Adjunct Associate Professor at Department of Mechanical Science and Technology. He currently leads the Data Science Implementation project of the NIH center of Excellence on the Big Data to Knowledge. His research interests include big data, data science, artificial intelligence, deep learning, and computational and experimental mechanics.

Belgacem-Bouzida Aissa received his Doctorat en Sciences in Material engineering from the University of Nancy I France. He is currently a Professor at the Department of Physics and Vice-President of the University of Batna 1, Algeria. He has published more than 40 papers in different journals and conferences. His research interests are materials and phase diagrams of multicomponents. alloys. He is a supervisor of many scientific research projects.

ملخص

تم فحص التفاعل بين موجات القص الافقية SH الموجهة مع نهاية حرة منحوتة لصفيحة نصف لانهائية بالطريقتين التحليلية والرقمية. وقد تم إعتماد فرض مادة الصفيحة مرنة ومتباينة المناحي. كما تمت نمذجة الصفيحة ذات التشوه على الحافة كتركيبة لمنطقتين : منطقة شبه لانهائية مع اجهادات منعدمة على السطوح ومنطقة قطاعية محددة ، المنطقتين تحدهما حدود مشتركة. تمت برهنة الحل التحليلي لحالة النهاية الحرة العمودية والذي تم استخدامه للتحقق من نجاعة البرنامج المنجز . في هذه الدراسة تم استخدام نمطين مختلفين واردين SH_0 و SH_1 كل على حده بهدف تحليل الأنماط المنعكسة والمرتبطة بالنهاية الحرة . تم إيجاد حل رقمي في حالة مجموعة واسعة من الترددات والزوايا المشطوفة. كما تم تمثيل خصوصا طاقة المرونة المنقولة بواسطة الانماط المنعكسة و ذلك باختيار زوايا مشطوفة و وترددات واردة. تم التأكد من صحة ودقة النتائج باعتماد مبدأ مصونية الطاقة و تقبل نسبة خطأ على الدقة لا تتجاوز 0 .001 %. المنهج التحليلي المقترح في هذه الأطروحة يساهم في فهم التفاعل بين الموجات SH الموجهة و عيوب المواد ويبين ان هذه الطريقة يمكن ان تشكل قاعدة إرشادية للمراقبة الغيرمدمرة للصفائح.

كلمات مفتاحية: نهاية منحوتة, تشوه الحافة, صفيحة مرنة, موجاتSH ,دالة الموجة

Abstract

The interaction of guided Shear Horizontal (SH) waves with the beveled free end of a semi-infinite plate is analytically and numerically investigated. The material of the plate is assumed to be elastic, homogenous, and isotropic. The plate with edge defect is modeled as a combination of a semi-infinite region with traction free surfaces and a bounded wedged region, separated by a common boundary. The analytical solution of the vertical free end case for the two regions is derived and used in verifying the numerical implementation. In this study, two single incident modes SH_0 and SH_1 were used individually in order to analyze the corresponding reflected modes from the free end. The numerical solution is determined for a wide range of frequencies and bevel angles. Specifically, the elastic energy carried by the reflected modes is reported for selected beveled angles and incident frequencies. The validity and accuracy of the results are checked by satisfaction of the energy conservation principle with a tight error tolerance less than 0.001 percent. The analytical approach proposed in this thesis contribute to the understanding of the interaction of guided SH waves with defects and shows that this method can be an efficient guidelines for non-destructive testing of plates.

Keywords: Bevel end; Edge defect; Elastic plate; SH waves; Wave function

Résumé

L'interaction des ondes de cisaillement horizontales (SH) guidées avec l'extrémité libre biseautée d'une plaque semi-infini est analytiquement et numériquement examinée. Le matériau de la plaque est supposé élastique, homogène et isotrope. La plaque présentant un défaut de bord est modélisée comme une combinaison d'une région semi-infinie avec des contraintes nulles en surfaces et d'une région sectorielle bornée, délimitées par une frontière commune. La solution analytique du cas d'extrémité libre verticale pour les deux régions est démontrée et utilisée pour vérifier l'implémentation numérique. Dans cette étude, deux modes incidents distincts SH_0 et SH_1 ont été utilisés individuellement afin d'analyser les modes réfléchis correspondants de l'extrémité libre. La solution numérique est déterminée pour une large gamme de fréquences et d'angles de biseau. Spécifiquement, l'énergie élastique transportée par les modes réfléchis est représentée pour une sélection d'angles biseautés et fréquences incidentes. La validité et la précision des résultats sont vérifiées par la satisfaction du principe de conservation de l'énergie avec une tolérance d'erreur étroite inférieure à 0,001%. L'approche analytique proposée dans cette thèse contribue à la compréhension de l'interaction des ondes SH guidées avec les défauts et montre que cette méthode peut constituer une ligne de conduite efficace pour le contrôle non destructif des plaques.

Mots clés: Extrémité biseautée; Défaut de bord; Plaque élastique; Ondes SH; Fonction d'onde.